Investigation of Resistance Spot Weld Failure in Tailored Hot Stamped Assemblies

by

Cameron O'Keeffe

A thesis

presented to the University Of Waterloo

in fulfillment of the

thesis requirement for the degree of

Master of Applied Science

in

Mechanical and Mechatronics Engineering

Waterloo, Ontario, Canada, 2018

I hereby declare that I am the sole author of this thesis. This is a true copy of the thesis, including any required final revisions, as accepted by my examiners

I understand that my thesis may be made electronically available to the public

Abstract

This thesis presents the results from the mechanical characterization of resistance spot welds within hot stamped USIBOR® 1500-AS steel sheet (1.2 and 1.6 mm thickness) with tailored properties. Three parent metal conditions, ranging from a fully martensitic (495 HV) to a mixed ferritic-bainitic microstructure (211 HV), were obtained using in-die heating (IDH) to control the cooling (quench) rate during the hot stamping process. Flat sheets and hat channel geometries were produced through die quenching in which the die was maintained at 25, 400, and 700°C with strengths of 1,548, 817, and 671 MPa, respectively.

The as-quenched sheets were resistance spot welded and mechanically tested in lap shear, cross tension, V-bend, and JIS tensile coupon geometries to characterize the mechanical response of single welds under various loading orientations. Hardness testing was conducted on the welds to investigate the hardness (strength) distribution in the welded region, heat affected zone (HAZ) and parent metal. The drop in hardness within the HAZ increased as the parent metal strength increased, such that the hardness of the HAZ was similar for all three spot welded parent metals (211-318 HV). In the mechanical testing, strain localized in the HAZ (or nugget) with the result that the strength of the welds was relatively constant for all die quench conditions. For the range of material conditions considered, the lowest weld strength 4.0-4.5 kN was measured in the cross-tension tests compared to 12.1-15.0 kN for the lap shear tests (data for 1.2 mm sheet).

A new mechanical test, termed the "Caiman", was developed to study groups of welds under both static and dynamic Mode I structural loading. Channel sections comprising of fully quenched material as well as hot stamped components with tailored, lower strength flanges were joined via spot welding. The experiments subjected the welded regions to Mode I tensile loading to investigate how

failure propagated along the spot weld line. It was found that the energy absorption within the welded connections was higher for the lower strength (tailored) parent metal conditions, largely due to activation of plastic deformation within the parent metal as opposed to the fully martensitic condition for which deformation was confined to the weld nugget or HAZ. High speed thermal imaging was shown to be an effective method to detect failure of individual welds and track failure propagation within the welded assembly due to local adiabatic heating associated with weld fracture or pullout. Temperature increases of 7 °C were typical of quasi-static loading whereas increases of 80 °C were observed under dynamic loading. It was determined that initiation of the first weld failure was delayed slightly under dynamic loading (relative to quasi-static); however, failure propagation after initiation was more rapid for dynamic loading for a given load point displacement.

Numerical simulations of the lap shear and cross tension single weld experiments were used to calibrate weld failure models within the commercial finite element software LS DYNA, with relatively good correlation to the experimental data. The calibration exercise revealed the importance of simulation of the post failure response, in particular the use of the "fade energy" numerical parameter, to more accurately capture the energy released during the weld fracture event.

The weld failure models calibrated from the single weld tests were applied to simulate the static and dynamic Caiman experiments without additional "tuning". For the quasi-static Caiman simulations, the predicted load-displacement response and failure propagation were relatively accurate, with higher errors for the fully martensitic case since the HAZ was not modelled. The dynamic simulations aligned relatively well with the experimental results.

Acknowledgements

I would like to thank my supervisors, Dr. Michael Worswick and Dr. Clifford Butcher for the opportunity to work on this project and for their support and guidance throughout my quest. I would also acknowledge Dr. José Imbert for his support of my project and guiding me through grad life. Thanks to Ryan George, Dr. Michael Nemcko, and Dr. Alexander Bardelcik for their support in hot stamping and design.

The support for this project from Honda R&D Americas, Promatek Research Center, ArcelorMittal, Automotive Partnership Canada, The Natural Sciences and Engineering Research Council, the Ontario Research Fund, and the Canada Research Chair Secretariat is gratefully acknowledged.

In the lab the assistance and guidance of Eckhard Budziarek, Jeff Wemp, Chris Peace, Tom Gawel, Andy Barber, and Neil Griffett allowed me to complete the experiments successfully and safely. Whether it's operation of a die set or material testing system the technician team here knows how to get work done. None of this work would have been half as enjoyable without the other grad students, thanks to Cale Peister for the talks about racing and other shenanigans, Kyu Bin Han for crushing assignments and lunches, and Kaab Omer for the project support. Shout outs to Jacqueline Noder, Sam Kim, Matt Tumers, Luke ten Kortenaar, Armin Abedini, Pedram Samadian, Alireza Mohamadizadeh, Chris Kohar, Cameron Tolton, Sante DiCecco, Nikky Pathak, Kenneth Cheong, Taamjeed Rahman, and Amir Zhumagulov.

Thanks to my parents and siblings for their support and encouragement. Also, thank you to Allison Florence Hague for putting up with the never-ending thesis and hair.

Table of Contents

List of Figures

1.0 Introduction

1.1 Motivation

The automotive industry is utilizing novel manufacturing processes to produce light weight structural components that reduce vehicle weight and increase fuel economy. One such manufacturing process is hot stamping that involves heating a boron steel sheet in a furnace followed by forming in a chilled tool. By partitioning the forming die into temperature controlled sections to control the quench rate, the microstructure within different regions of a single part can be varied to produce a tailored microstructure with mechanical properties that vary from high strength (low ductility) to moderate strength (high ductility).

To apply these tailored hot stamped components to automotive structures they need to be able to be attached to other parts. Resistance Spot Welding (RSW) is a joining technique used heavily by the automotive industry to join sheet metal components. Spot welds are created by running electrical current through clamped pieces of sheet metal at a point. The heat melts the sheets together, creating a bonded nugget of material. For mild grade steels, the spot welding process creates a fully hardened nugget that is surrounded by the lower strength base metal. However, when the base metal is largely martensite as in hot stamped components there is a region surrounding the weld that gets tempered because the material is heated to just below the critical temperature creating a softened sub critical Heat Affected Zone (HAZ) that is softer and more ductile than the surrounding material. Due to this localized strength reduction, it has been shown that cracks will initiate in the HAZ and can lead to premature failure of hot stamped structural components. The onset of fracture largely governs the crash performance of a structure and since fracture can initiate in the HAZ, it is important to investigate this phenomenon.

To reduce development costs, manufacturers are creating complex computer simulations to ensure new designs in automotive structures meet safety standards before investing in tooling and physical testing. To improve the accuracy of these simulations, new material models are continually being developed to better predict the deformation and fracture of the materials used. Modelling of spot weld failure is of interest when considering the deformation behaviour of tailored hot stamped structures due to the complex mechanical behaviour of spot welds. Modelling of a single weld alone is challenging but methods have been proposed in literature to tackle the problem. What is uncertain is how to transition from single welds to welded structures and how to properly capture the behaviour of spot weld groups. The aim of the current research is to experimentally and numerically investigate failure within spot welded tailor hot stamped coupons and structures.

1.2 Hot stamping

Hot stamping was initially developed to produce steel sheet components with a fully martensitic microstructure because complex parts with ultra-high strength could be formed at elevated temperatures that couldn't be formed at room temperature due to the low ductility of martensite. To obtain a martensitic microstructure a high cooling rate is needed so chilled dies are commonly used. [1]. Later on, it was discovered that by altering the temperature of the forming die, different microstructures could be produced in the final part [2]. As shown by Figure 1, altering the cooling rate of the blank changes the resulting microstructure of the formed part [3]. With lower cooling rates bainite and ferrite are formed by crossing each respective region of the CCT diagram during the quench.

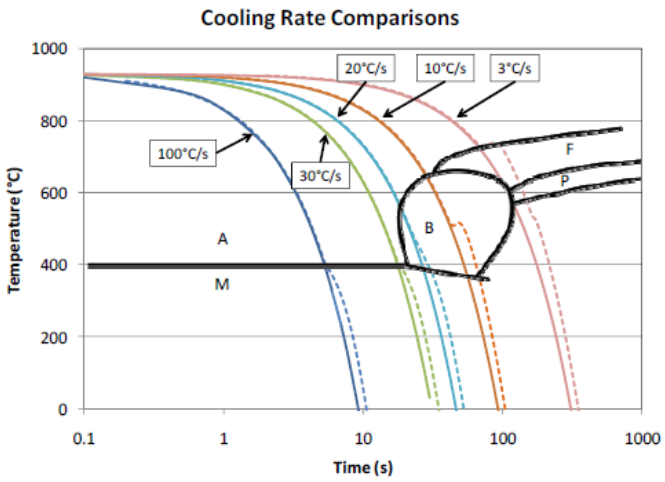

Figure 1: Continuous Cooling Transformation diagram for USIBOR® 1500-AS [4]

Several procedures are available to tailor the microstructure throughout a hot stamped part such as tailor welded blanks, blank tempering, and in die heating. Tailor welded blanks involves joining materials of varying strength by laser welding followed by austenizing and hot stamping. In the blank tempering process, only certain regions of the blank are heated above the austenizing temperature so that only these regions experience phase transformation during the hot stamping process. The In Die Heating (IDH) process involves tailoring a component by controlling the temperature at different regions within the quenching die. To produce more ductile regions, a lower cooling rate is used to produce more bainite and ferrite. This is achieved by heating portions of the die and maintaining the tooling at some desired temperature. In areas where intrusion resistance is key, high cooling rates are used to produce high strength martensite. This is accomplished by cooling portions of the tooling with water channels to maintain the die at room temperature [5].

A multitude of studies have been conducted on IDH to study its advantages and limitations relative to conventional hot stamping. It has been shown that IDH can be used to reduce the springback of the formed part and increase formability [6]. The main advantage of IDH is the ability to produce a variable hardness distribution throughout the formed part. George *et al.* [4, 7]

demonstrated that several distinct microstructures could be produced in a single part by producing a lab-scale B-pillar which had an ultra-high strength zone with low ductility and a region of moderate strength and higher ductility as shown in Figure 2.

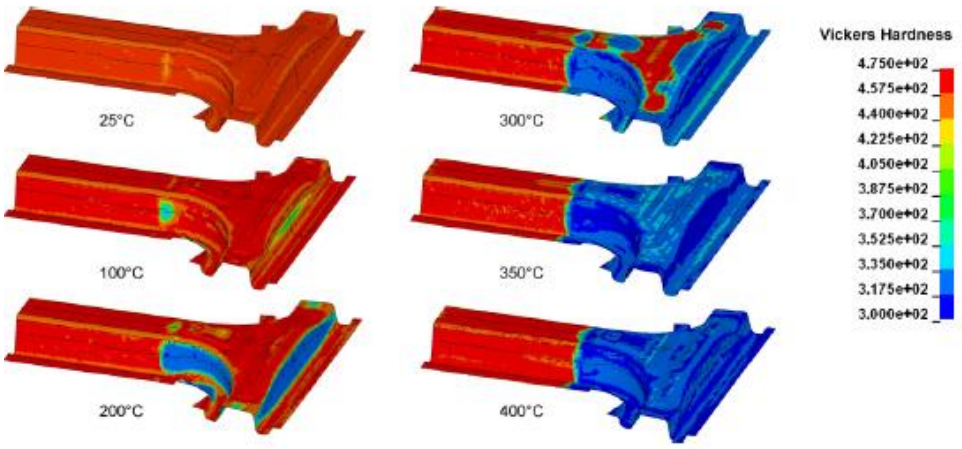

Figure 2: Vickers hardness contour plots for various heated die temperatures [4]

To numerically model the deformation of tailored components, one must accurately predict the distribution of material properties throughout the part. To accomplish this, forming simulations are used to predict the decomposition of austenite into bainite, ferrite, or martensite. The material model developed by Akerstrom [8] implemented in LS-DYNA finite element software is one such model which may be used to predict the final phase composition and Vickers hardness in each element as a result of the forming process.

While phase composition is difficult to validate in formed parts, defining the material as a composite offers a more physical approach to predict flow stress and fracture behaviour. Srithananan *et al.* [9] used micrographs to generate representative volume elements of dual phase steels. Utilizing this approach, the flow stress behaviour of martensitic and bainitic heat treated boron steels was numerically predicted for several different loading conditions with good agreement to the experimental results. While this method can accurately predict the response of the material it is

computationally expensive to implement into a full vehicle crash model. To that end, Golling [10] presented a double inclusion homogenization model to define the material behaviour of tailor hot stamped steel as a function of constituent content. Numerically this method was able to accurately predict the response of microstructures containing varying amounts of bainite, ferrite, and martensite while remaining computationally efficient.

Bardelcik *et al.* [11] used a phenomenological approach to characterize the tailored microstructures by assuming a Voce hardening model for the constitutive response and assuming the coefficients to be functions of the microhardness. The predicted flow stress behaviour of several tailored microstructures at different strain rates overlaid on experimental data is shown in Figure 3. In crash events, the flow stress response alone is not sufficient to accurately describe the deformation of a component. The fracture behaviour must also be characterized such that the initiation of cracks may be predicted in complex loading conditions found in hot stamped components. Numerically, if the onset of fracture is inaccurately predicted, the simulated results will provide non-physical results that do not correlate to experimental results. One commonly used phenomenological damage (fracture) model is the Generalized Incremental Stress State dependent damage Model (GISSMO) [12] that uses Eq. (1) to define damage by a scalar variable, *D*, that is a function of equivalent plastic strain (ε_p), the plastic strain at failure (ε_f) that is defined by a fracture loci, and a user defined damage exponent, *n*. ten Kortenaar [13] developed the set of fracture loci for tailor hot stamped components shown in Figure 4.

$$\Delta D = \left(\frac{n * D^{\left(1-\frac{1}{n}\right)}}{\varepsilon_f}\right)\varepsilon_p \tag{1}$$

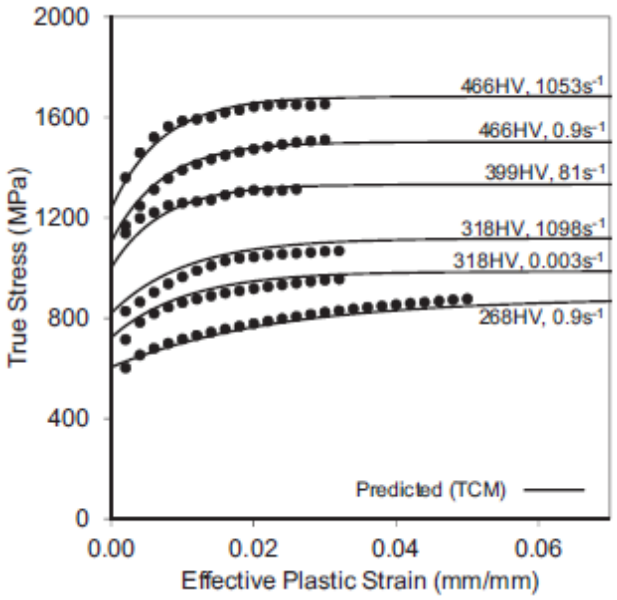

Figure 3: The measured (symbols) and predicted (curves) flow stress curves for a variety of as-quenched Vickers hardness and strain rate values [11]

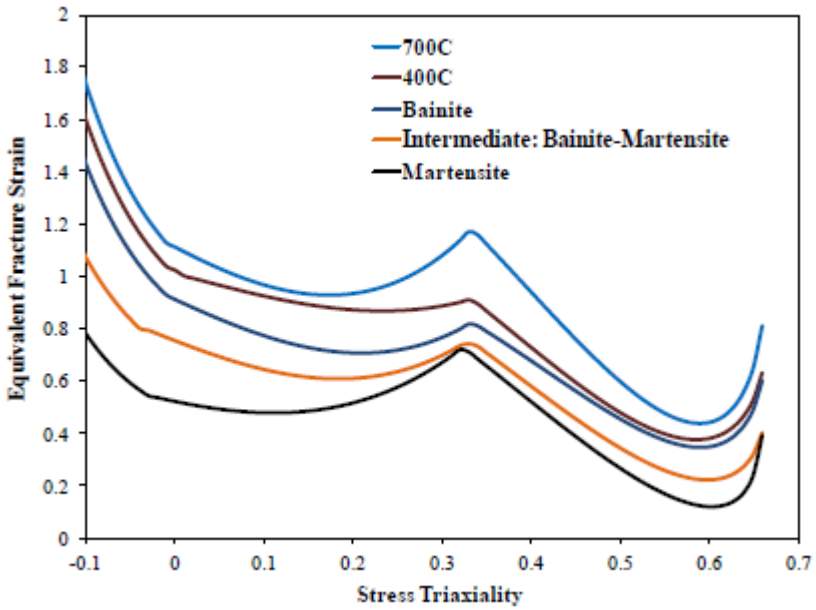

Figure 4: Fracture loci for several material quench conditions [13]

Omer *et al.* [14] used these fracture loci and the flow stress curves shown in Figure 4 and 5 to define a hardness dependent material model. When implemented into a finite element simulation, the

material model was able to accurately predict the energy absorption of tailored axial crush components as seen in Figure 9. Eller [15] used a similar hardness-based modelling approach that utilized a Modified Mohr-Coulomb fracture criterion and power law hardening to define the properties throughout the hat channels and was able to accurately predict the deformation and fracture behaviour in four-point bending.

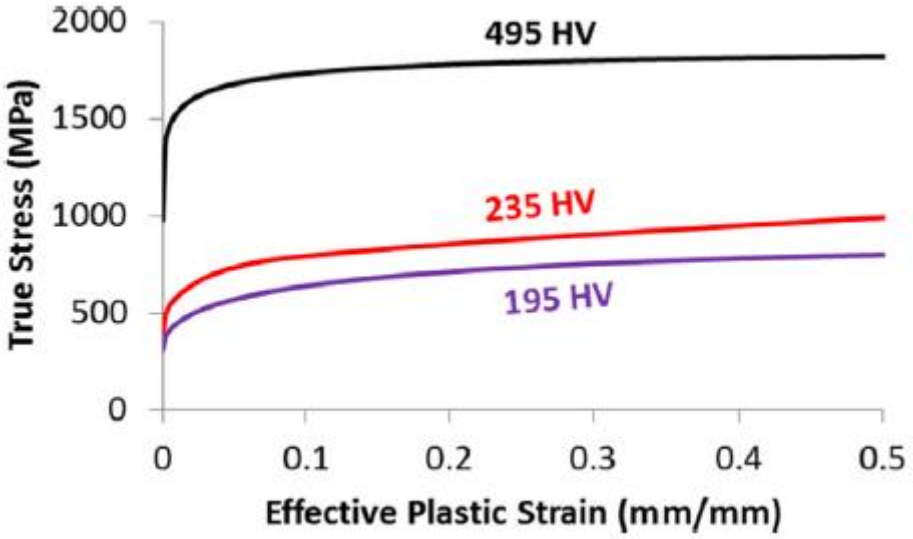

Figure 5: Flow stress curves for several quench conditions [14]

By utilizing IDH, components may be tailored to provide high energy absorption and stable deformation when crushed. Eller *et al.* [15] created a hat channel section with two distinct zones along the length of the part and was able to produce a bainitic microstructure in one region and a martensitic condition in the other region. When these specimens were subjected to quasi-static 4-point bending it was shown that fracture would initiate in the martensitic region. Prajogo [16] showed that by tailoring the flanges of side impact beams, the extent in which the part fractured could be suppressed in 3-point bending. Omer *et al.* [14, 17] produced the axial crush members shown in Figure 6 to highlight how IDH can be used to stabilize the crush response of ultra-high strength components in crash scenarios.

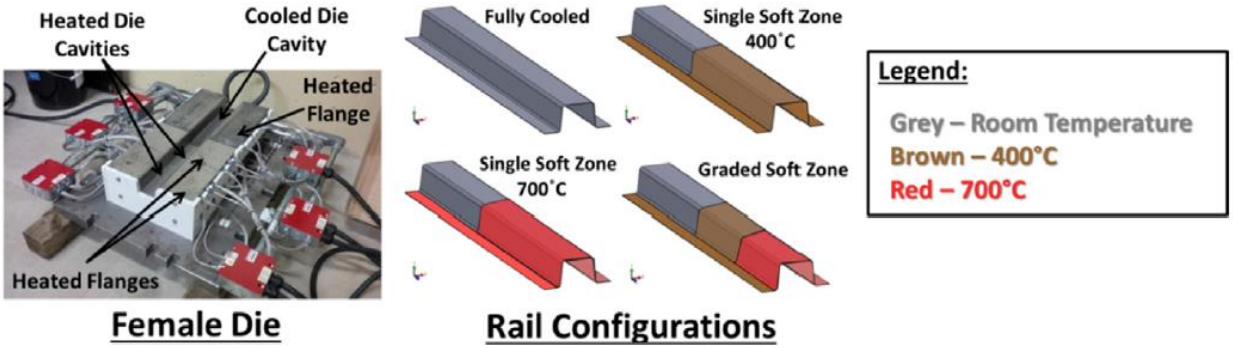

Figure 6: Tailored axial crush female die and rail configurations [14]

Once formed, the parts were crushed by a crash sled at 10.6 m/s weighing 855 kg to investigate how tailoring affected the dynamic crush response. In Figure 7, the force and energy measurements are shown for the tailoring configurations shown in Figure 6. With this test it was shown that the crush efficiency of the rail increased when a ductile region was introduced. While the fully cooled part exhibited the highest amount of energy absorption, extensive fracture was observed during the crush event as seen in Figure 8. In the tailored rails, the crush behaviour was more stable due the large majority of the deformation occurring in the soft areas. Specifically in the graded soft zone rail, progressive folding was observed which began in the softest region and concluded in the martensitic region.

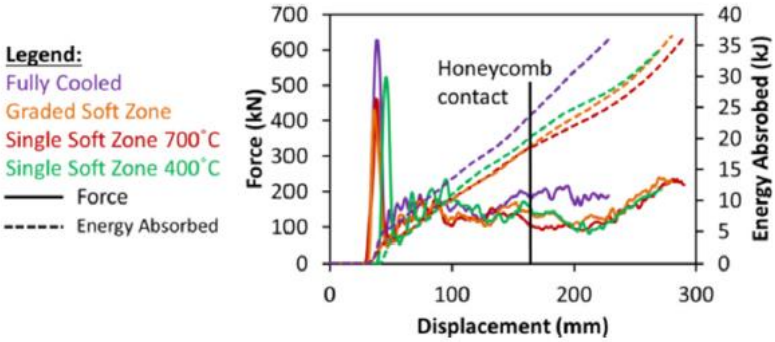

Figure 7: Average dynamic force displacement and energy absorption curves for tailored crush rails [14]

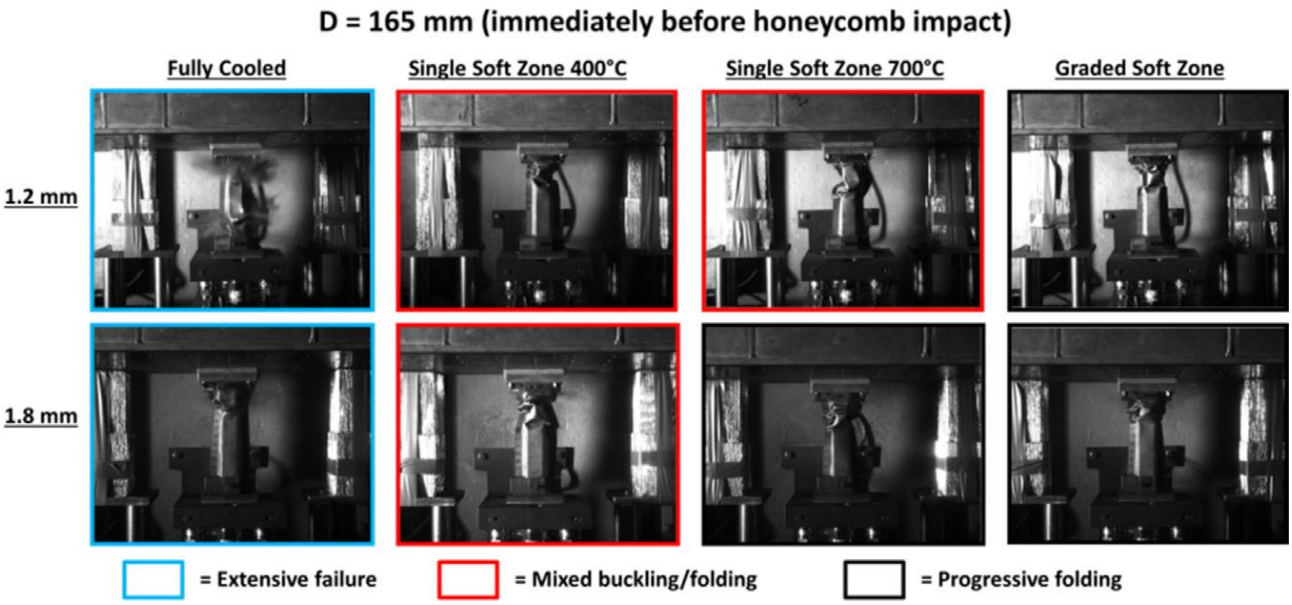

Figure 8: Images showing the axial crush of all tailored rails immediately prior to honeycomb impact [14]

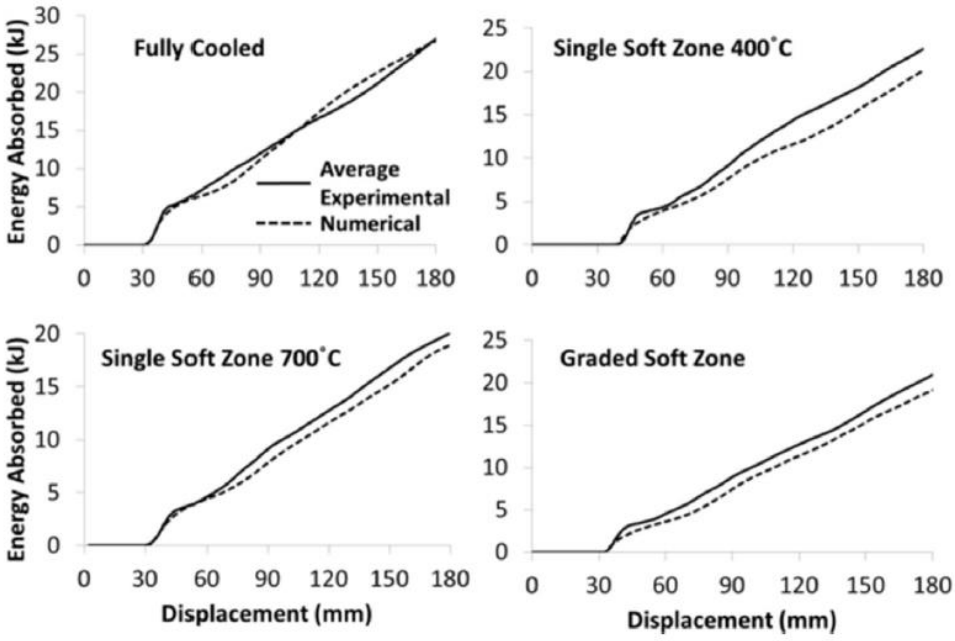

Figure 9: Measured versus predicted energy absorption curves for axial crush specimens [14]

Clearly, IDH can be used to produce parts which utilize the strength of martensite while suppressing undesirable fracture behaviour. For this manufacturing method to be viable in the

automotive industry, the mechanical behaviour of these components must be accurately captured in numerical models to reduce tooling costs and the number of design iterations.

The preceding failure prediction strategies are designed to predict parent metal failure. However, it is important to be able to predict the failure of joints, in particular spot welded joints that comprise the most common joining method for automotive structures. The deformation and rupture of the joints in a structure largely governs the overall deformation and energy absorption therefore RSW must be properly modeled in vehicle crashworthiness simulations

1.3 Resistance spot welding of hot stamped boron steels

For steel-to-steel joining, Resistance Spot Welding (RSW) is a commonly used joining technique with upwards of 2,000 spot welds in one automotive structure [18]. The RSW process joins two sheets together by applying electrical current and clamping force at a point. The heat generated due to the resistance of the applied current causes the contacting metal components to melt together and form a nugget of joined material. In the region surrounding the nugget, the metal never reaches a molten state and a tempered region called the heat affected zone (HAZ) is produced. In martensitic steels, the nugget and base material are approximately the same hardness but the HAZ is significantly softer [19]. It has been shown that fracture will initiate in this softened area [20] therefore, proper characterization and simulation of the mechanical behaviour of the HAZ is crucial.

1.3.1 Resistance spot welding

RSW is a massless joining technique (no filler metal is added) that involves the application of electric current and clamping pressure in order to generate a nugget of joined material. In two sheet connections there is a short current path and therefore, to produce the required heat, low voltage and high current are required. The RSW process as shown in Figure 10 begins by squeezing the work piece components between the electrodes, then the desired clamping load is applied to the work piece by the electrode, current is then passed through the work piece and the nugget is held to allow for solidification of the molten metal before the material is released.

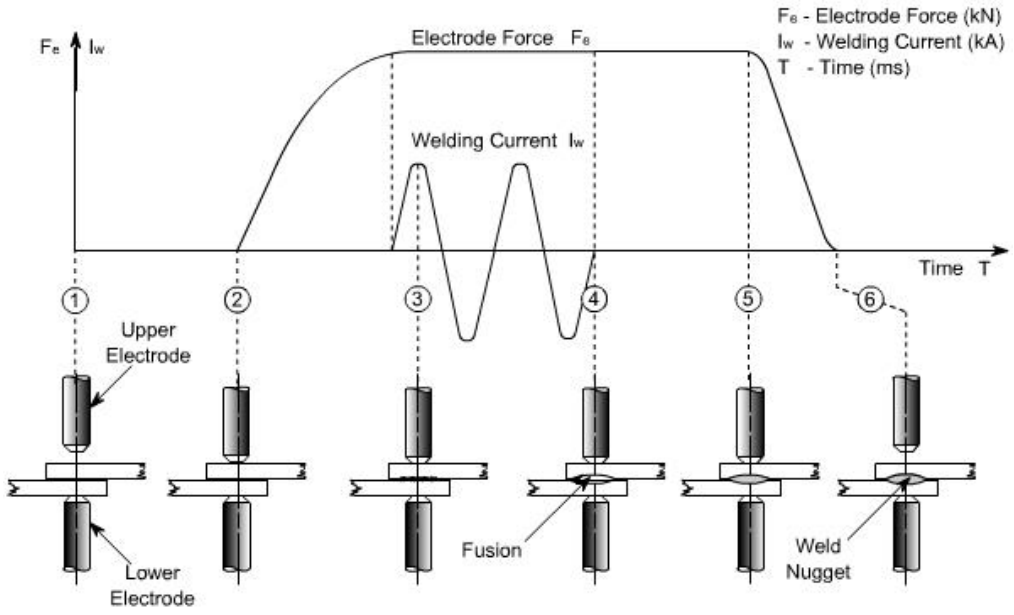

Figure 10: Spot weld process [21]

While the clamped region turns completely molten, the adjacent material becomes heated but does not reach the melting temperature resulting in a local tempering process. As shown by the cross-sectional view in Figure 11, this occurs because of the how the heat is distributed throughout the two sheets.

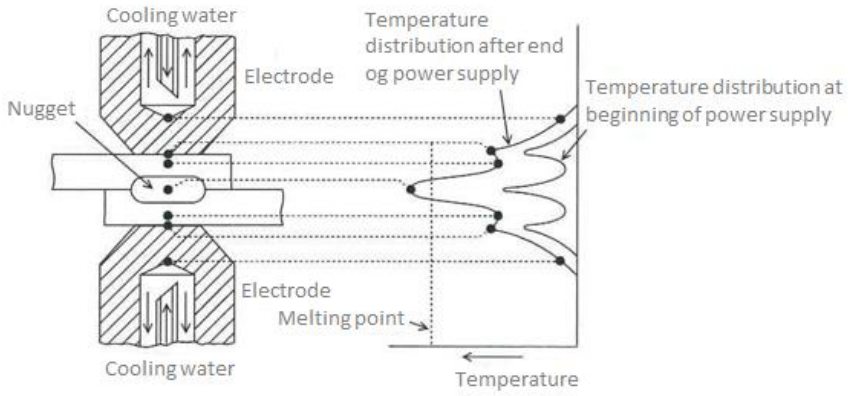

Figure 11: Cross sectional spot weld view and heat distribution [22]

Peak heat generation occurs at the interface between the clamped sheets due to the high resistance of the discontinuity. The dispersion of heat causes the sheets to melt and fuse resulting in a welded nugget and tempered surrounding region.

1.3.2 Mechanical performance of RSW

1.3.2.1 Mechanical performance experimentation of RSW

Many types of destructive mechanical tests have been developed to characterize spot weld performance. Qualitative spot weld tests are performed on assembly lines to visually assess the quality of the spot weld based on the failure surface. An example of this is the peel test shown in Figure 12 that is used to determine the quality of the weld based on weld failure. If spot weld pull out as shown by Figure 13 part A is observed then the welding process is deemed satisfactory. If interfacial fracture occurs then the process parameters need further refinement.

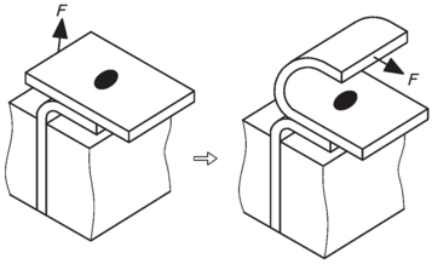

Figure 12: Manual peel test [23]

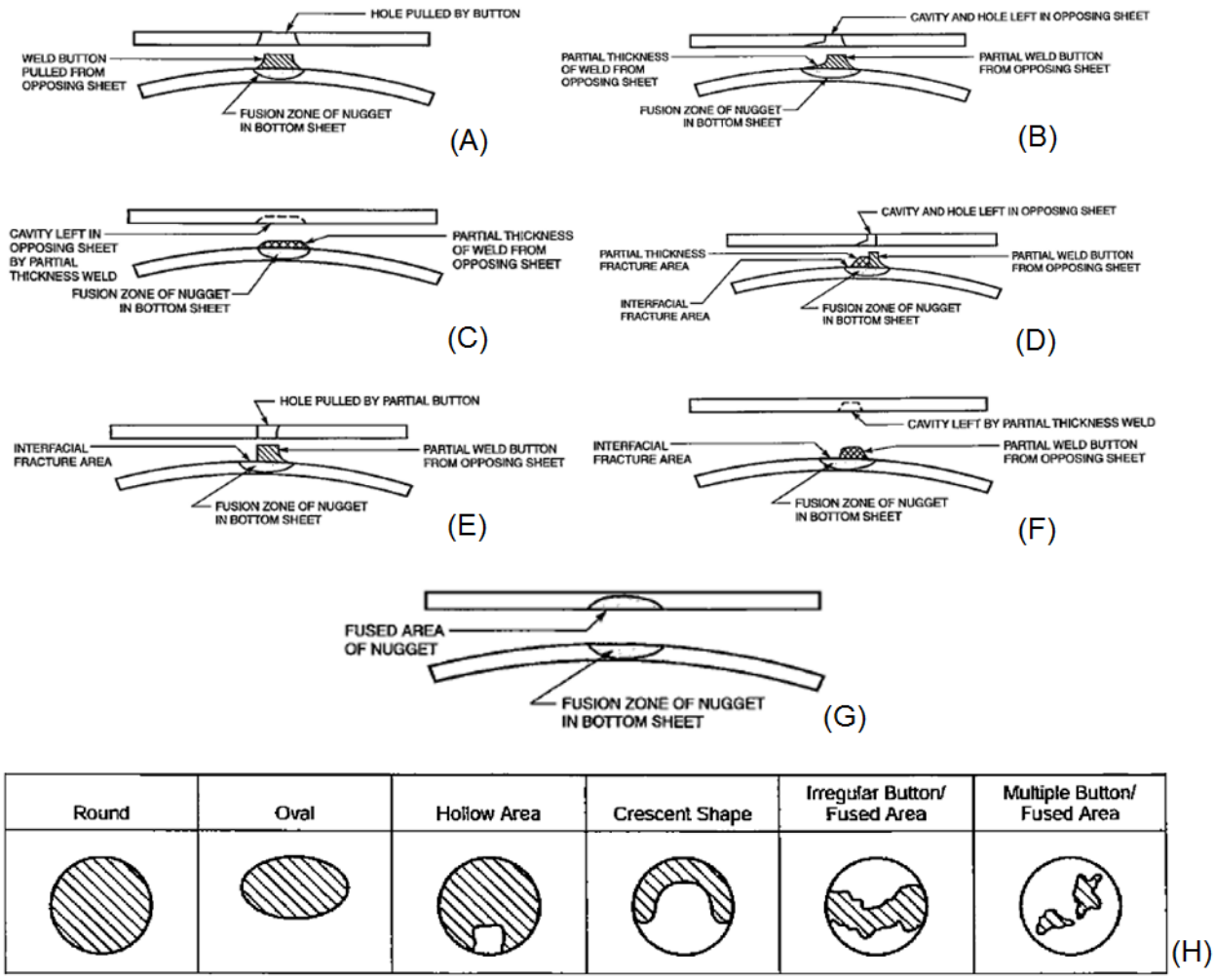

Figure 13: Spot weld failure in (A) Button Pullout (B) Partial Thickness Fracture with Button Pull (C) Partial Thickness Fracture (D) Interfacial Fracture with Button Pullout and Partial Thickness Fracture (E) Interfacial Fracture with Button Pullout (F) Interfacial Fracture with Partial Thickness Fracture (G) Interfacial Fracture (H) Weld fracture in plain view [24]

The fracture mode of the spot weld reveals a large amount about the quality and robustness of the spot weld process parameters. Failure of spot welds may affect the stiffness, noise, vibration and crash performance of a structural component [25]. Due to the rapid electro-thermo-mechanical event occurring during RSW, the resulting joint can take a variety of forms. Typically, when there is not enough heat delivered into the work piece, interfacial or partial thickness failure occurs. Both of these modes are unfavorable in load bearing structures due to the low energy absorption and rapid

failure of this fracture mode. In industrial applications, a pullout failure mode is preferred because it offers the maximum amount of energy absorption.

As shown by Figure 14 there are three basic ways to initiate and grow a crack. To properly capture the fracture of resistance spot welds, each one of these modes must be characterized. In contrast to qualitative tests such as the peel test, the two main quantitative tests to determine the strength and ductility of spot welds in shear (Mode II) and tension (Mode I) are the lap shear and cross-tension tests. In the lap shear test, the spot-welded coupon is subjected to uniaxial loading until the weld fails as shown in Figure 15.

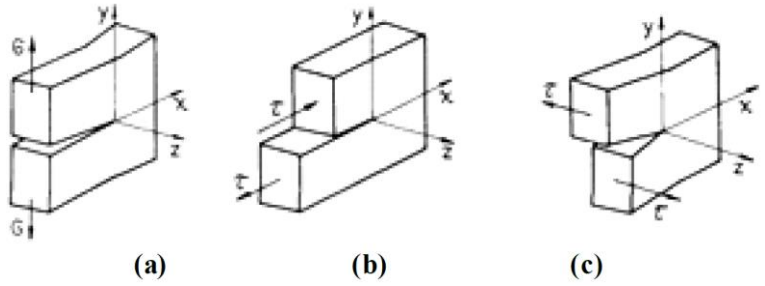

Figure 14: (a) Mode I - aperture (b) Mode II - sliding (c) Mode III – tear [26]

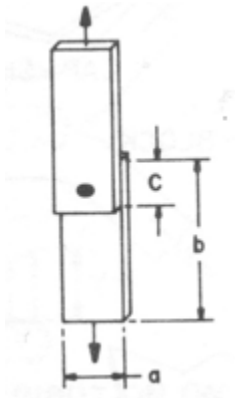

Figure 15: Lap shear test [27]

The lap shear test is utilized heavily by industry because lap shear specimens can be created and tested with relative ease. Typically, the force displacement data similar to that seen in Figure 16 is recorded over and the peak load is extracted to determine a "maximum shear force".

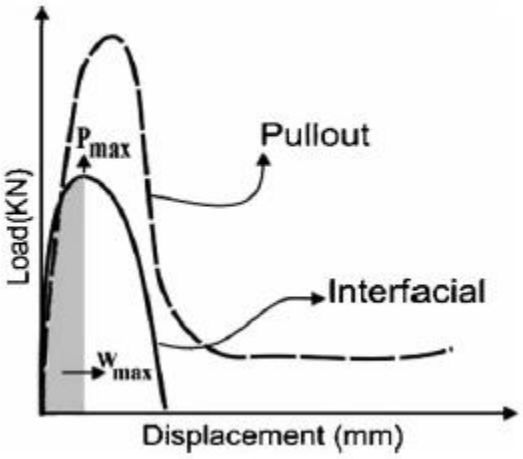

Figure 16: Load displacement diagram for lap shear in both failure modes [28]

Although the lap shear test provides an easy method to characterize the joints response in shear loading, the loading condition is complex due to a stress intensity at the notch of the weld and bending occurring in the base metal as shown by Figure 17.

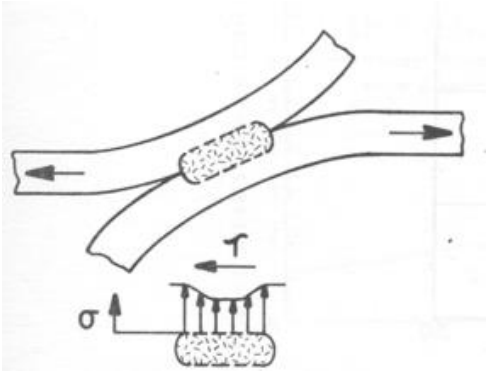

Figure 17: Stress distribution on nugget under lap shear [27]

During the lap shear test, the specimen experiences shear loading in the nugget and normal loading in the HAZ. Due to the nugget being subjected to the bulk of the shear stress, these tests typically show a high peak load and can reveal the dominant failure mode of the weld in shear. As shown by Figure 18, when the lap shear specimen fails by "pull-out", the specimen is subjected to a large amount of rotation and a complex stress state has developed when fracture occurs. Whereas for interfacial failure, the coupons experience less distortion and a smaller peak load as shown by Figure 16.

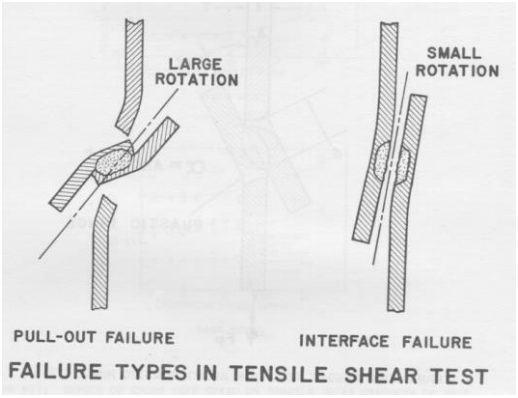

Figure 18: Lap shear failure modes [29]

For the cross-tension test shown in Figure 19, the specimen is subjected to transverse uniaxial loading.

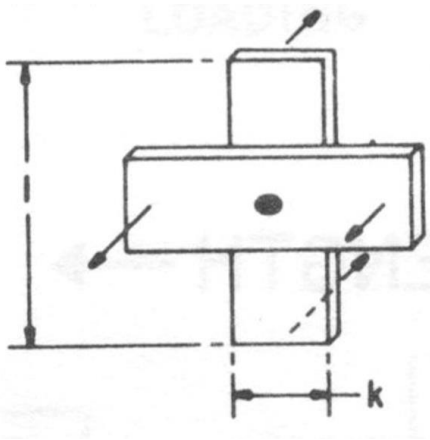

Figure 19: Cross tension test [27]

Similar to lap shear, the cross tension test is commonly used to calibrate spot weld settings due to the ease of specimen fabrication. The loading experienced in the spot weld is again complex due to the stress intensity at notch and the bending shown in Figure 20.

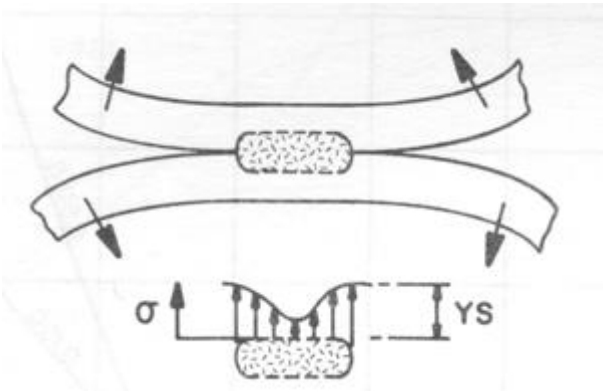

Figure 20: Stress distribution on nugget under cross tension [27]

During the test, the specimen experiences normal loading in the nugget and shear loading in the HAZ. In practice, the peak load is extracted from a measured force displacement curve and used to calculate a "maximum normal force". This test is also useful for determining the dominant failure mode of the spot weld in normal loading. Together, lap shear and cross-tension are the basic tests to characterize the mechanical behaviour of spot welds.

1.3.2.2 Mechanical performance simulations of RSW

Due to the complexities and experimental uncertainties in the RSW process as well as the variation of the mechanical properties within the HAZ, approximations are required to generate numerical models. Each modelling technique utilizes different meshing techniques and damage models to capture the behaviour of RSW joints. Wung *et al.* [30] defined the joint as a beam element that was governed by a force-based failure criterion. When the critical force was reached in the beam element it would be deleted to simulate failure of the spot weld. While this method may reasonably represent the behaviour of mild steels, the oversimplification of joint geometry can cause inaccurate predictions. Malcolm [31] refined this approach by using solid elements in place of beam elements to more accurately model deformation and failure of the joint. In this work, a mesh configuration using 8 brick elements governed by a force-based failure criterion was used to numerically represent the spot weld. These models were able to better represent the deformation of the joint prior to weld failure but were unable to capture the unloading behaviour of the joint post-failure.

Uncertainties and errors in the numerical models of single spot welds are compounded when analyzing welded components as in vehicle crash. The manner in which the materials and joints within a structure dissipate strain energy largely effect the impact performance. If the joints within a structure are designed to pull-out upon failure, force-based models are not sufficient to capture the energy absorbed by spot welded joints. Alternatively, by using a damage-based criterion in the base material and weld, nugget pullout out may be modelled by the progressive deletion of elements surrounding the nugget. Wang *et al.* [32] used a hardness distribution to define the variation in the yield strength. To mesh the region rigid beam elements comprised the nugget and shell elements represented the base material and HAZ. A constant value was used for the maximum strain in the failure criterion and thus was unable to accurately predict failure in different loading conditions as seen in Figure 21.

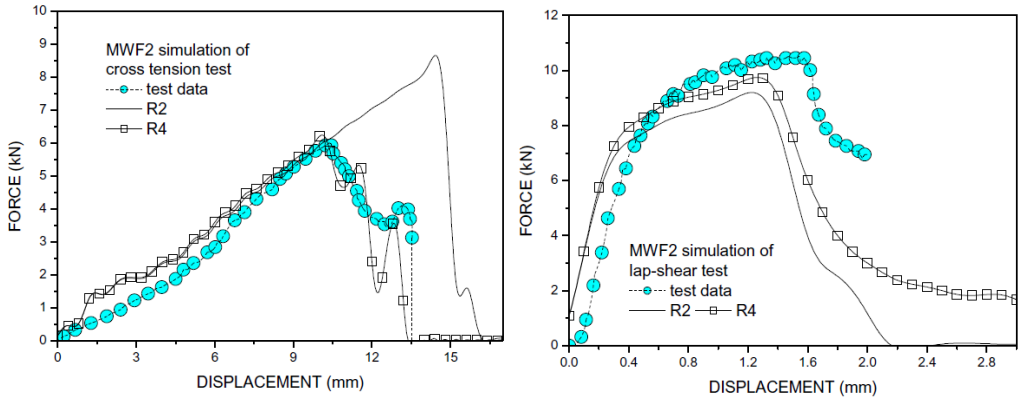

Figure 21: Comparison of simulated results to experimental data in cross tension and lap shear configurations by Wang [32] using a stress intensity (R2) and a yield strength scaling (R4) failure models

Nielsen [33] improved upon the method of Wang *et al.* [32] and used solid elements in combination with a modified Gurson [34] damage model to capture the mechanical behaviour. With this technique, both interfacial and pullout failure could be captured but it was computationally expensive due to the use of solid elements. Zeng [35] proposed a more efficient model that used rigid solid elements in place of the nugget and applied a Gurson-based damage approach to model the base material. Using this technique, good predictions were obtained for both cross-tension and lap shear tests as seen in Figure 22. However, since solid elements were used, it was not feasible to translate this to automotive crash structures that are based upon shell elements.

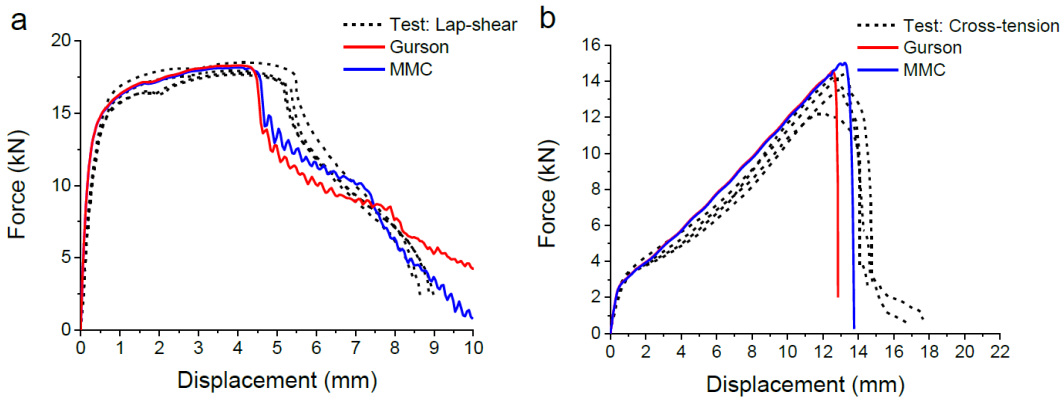

Figure 22: Comparison of force-displacement curves for two models with tests result: (a) lap-shear model/test curves: (b) cross-tension model/test curves by Zeng [35]

Nguyen [36] used the ductile ESI-Wilkins-Kamoulakos failure model [37] to predict the failure of the joint using both solid and shell elements to represent the base material. In this work, SYSWELD software was used to distribute the material properties throughout the weld in the finite element simulation. As shown in Figure 23, it was shown that accuracy improved by using shell elements to represent the base material and HAZ.

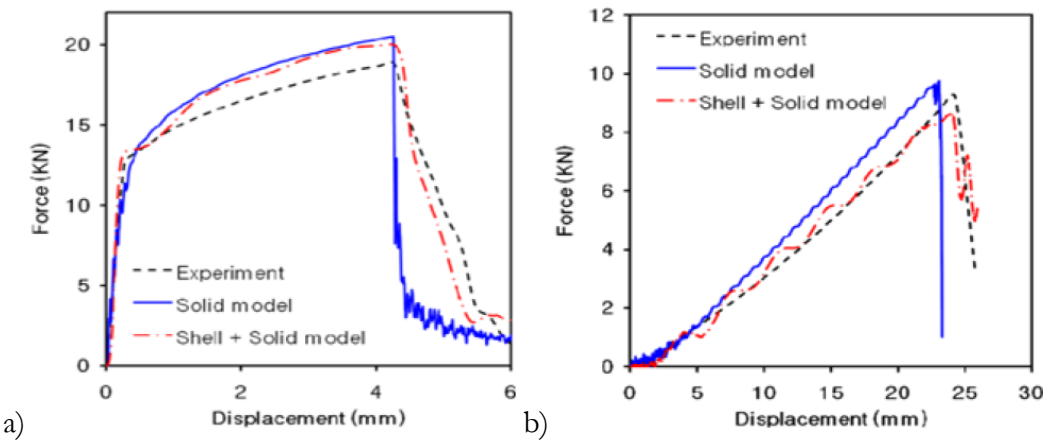

Figure 23: Comparison of the force-displacement curves for experiment and analyses a) Lap-shear test b) Cross-tension test by Nguyen [36]

1.3.3 Resistance Spot Welding of Martensitic Steels

As described in section 1.3.1, RSW is a fusion welding process in which heat is generated by a localized current and pressure is applied to ensure contact of the joining sheets. The physical principle for the heat generation is described by Joule's law. The current and clamping load must be such that a weld nugget is formed but not so high that molten metal is ejected from the weld zone. The complexity of RSW joints mainly stems from the inhomogeneity of the microstructure.

The joint can be broken down into three distinct zones, the fusion zone, HAZ, and base material. In Figure 11, the fusion zone is the region that the temperature surpasses the melting point of the material. In the HAZ, the metal is heated but not molten and is subdivided into three regions, the upper critical, intercritical, and subcritical HAZ. The upper critical HAZ is the region that experiences peak temperatures above the austenization temperature but doesn't become molten. The intercritical HAZ reaches temperatures between A_{C1} and A_{c3} and transforms into austenite and ferrite during the RSW process [38]. The subcritical region experiences temperatures below A_{c3} and experiences tempering of metastable bainite and martensite.

In dual phase steels, Baltazar [39] showed martensite grains heated to a temperature close to or below the lower critical transformation temperature would soften due to the diffusion of carbon. This type of softening is also seen in the subcritical HAZ when martensitic steels are spot welded. It was shown by Baltazar [40] that while the grains of the base material are retained in this region, they have been tempered. As shown in Figure 24, it was observed that the tempered martensite in the subcritical HAZ would experience significant reduction in hardness with respect to the grains seen in the base material.

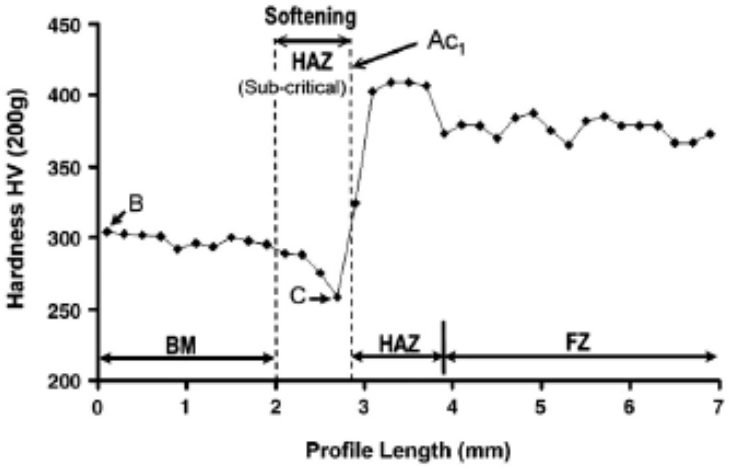

Figure 24: Vickers micro-hardness indentation profile across resistance spot welded DP980 steel [40]

The degree of HAZ softening is mainly dependent on the base material and spot weld parameters used. While martensite content and alloying elements are used in hot stamping to increase the strength of the material, they largely affect the degree of softening seen in the subcritical HAZ [41, 42]. It has also been shown by Dancette[43] that as the amount of heat input into the material increases, so does the softening. Therefore, thicker sheets and higher welding currents increase the degree of softening.

Using several tailored hot stamped grades, Eller *et al.* [44] welded several coupons together and investigated the mechanical behaviour of resistance spot welds. As seen in Figure 25, there is a clear relation between hardness of the parent metal and severity of softening within the HAZ. Eller subjected the weld to different loading conditions so that the force and strain data could be used to optimize the flow stress and fracture behaviour in numerical models. In Figure 26, for a fully hardened boron steel where the change in material properties is the most aggressive, the ductile media fractures at strains much lower than that of the base material. To numerically model the welded region a linear interpolation scheme was used to scale the yield strength and failure strain in the parent material radially around the spot weld centers. Three mechanical tests were performed to obtain local Digital

Image Correlation (DIC) strain measurements to correlate with the force-displacement response of the weld so that inverse finite element simulations could be used to calibrate the material properties of the critical HAZ. This method was then evaluated on the tensile specimen in Figure 27 with good agreement to experimental data.

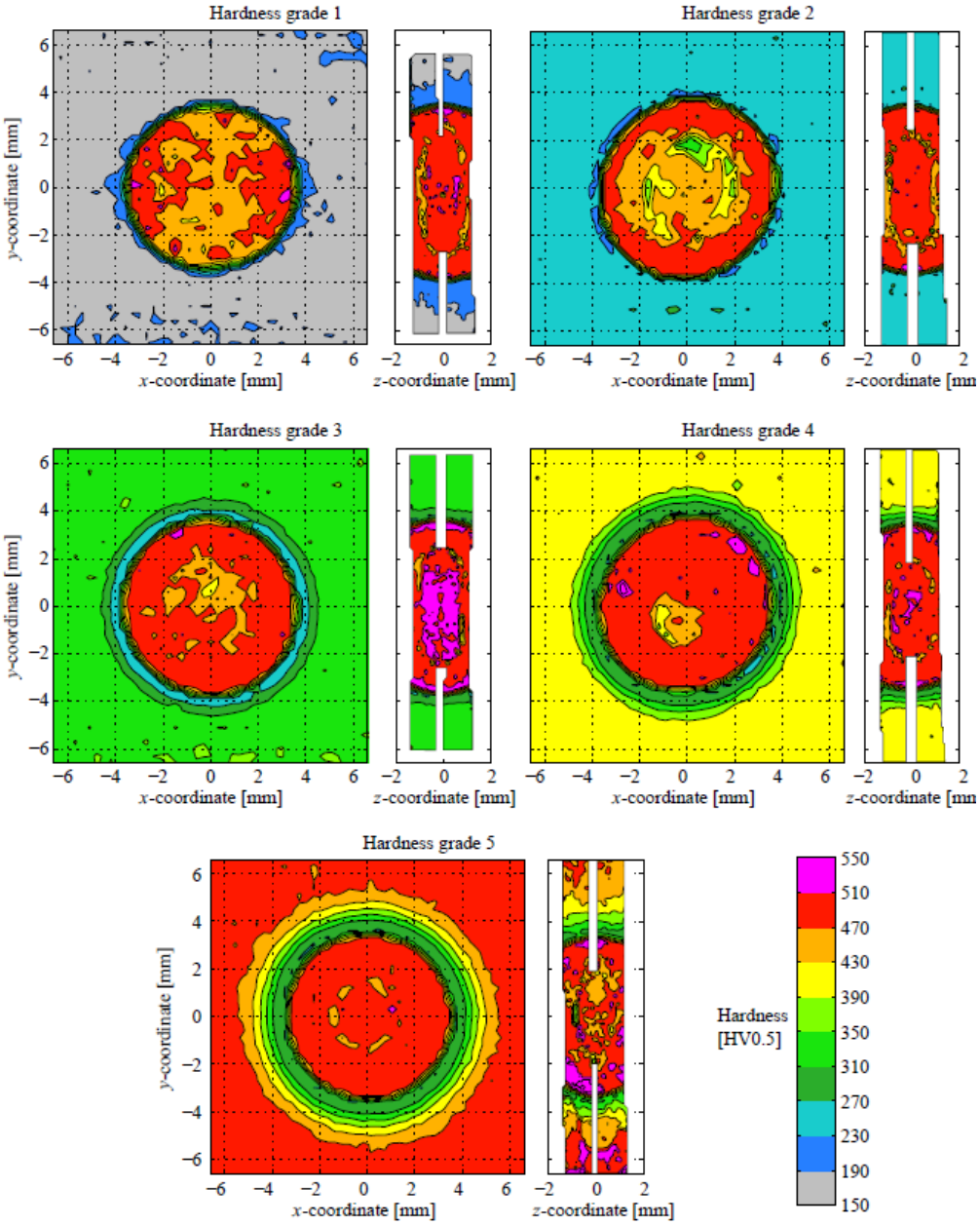

Figure 25: In-plane and cross-sectional hardness measurements of RSWs in five different base material hardness grades [45]

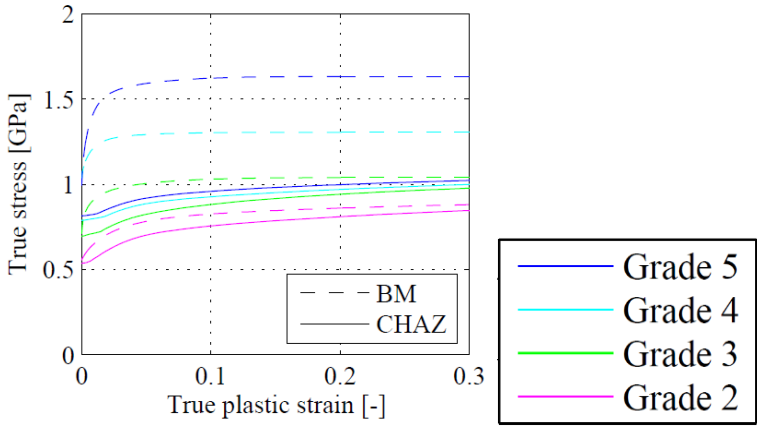

Figure 26: Base metal and Critical Heat Affected Zone strain hardening curves for the various tailor hot stamped steels in Figure 25 [45]

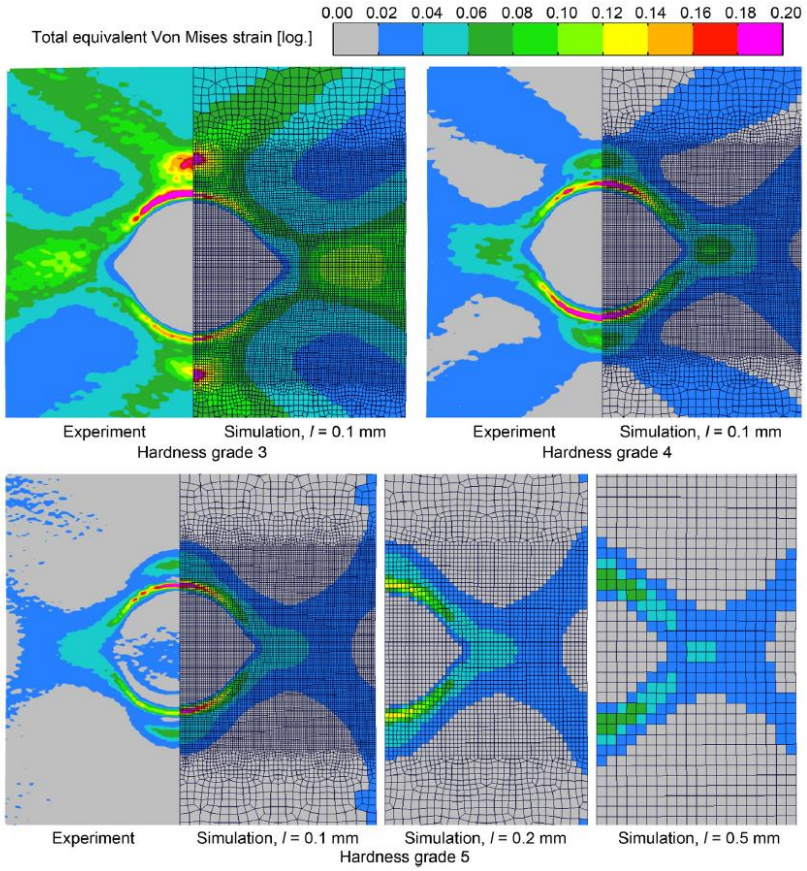

Figure 27: Measured and predicted strain fields of coupon tests of various tailor hot stamped grades [44]

Burget [46] used a thermo-mechanical testing system to create bulk material with the same microstructure as the HAZ in fully hardened steel. Specimens were then fabricated to determine the plastic and fracture behaviour of the region. Burget [46] then used a hardness traverse of the spot weld to obtain the hardness distributions and map the material properties onto a solid element mesh. Using von Mises plasticity and a ductile fracture criterion, the results shown in Figure 28 were obtained where the yielding and fracture in the specimen was accurately captured by the numerical model.

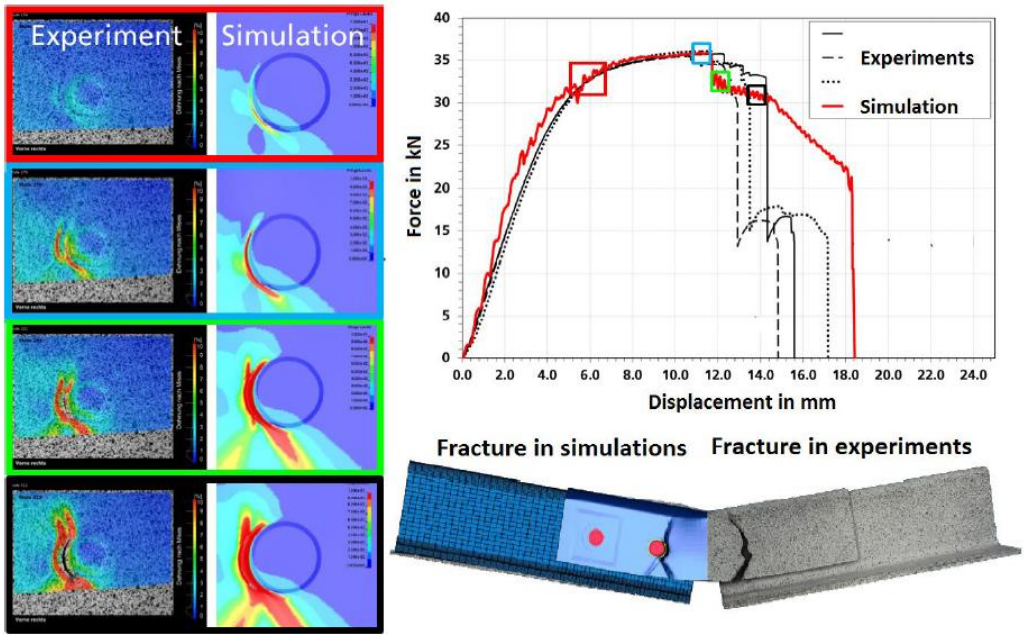

Figure 28: Comparison of local equivalent strain distributions, force vs. displacement curves and final deformed states of the 3-point bending tests on components from experiments and simulations [46]

1.4 Resistance spot weld groups

Since automotive structural components never contain only a single spot weld, the failure of weld groups is critical to understand how spot welds affect crash performance. Marya *et al.* [47] investigated how the number of spot welds in a lap shear specimen effected the maximum shear force and fracture mode. For welds of various diameters, as shown in Figure 29, the strength of the weld line under quasi-static loading conditions linearly increased with the number of welds.

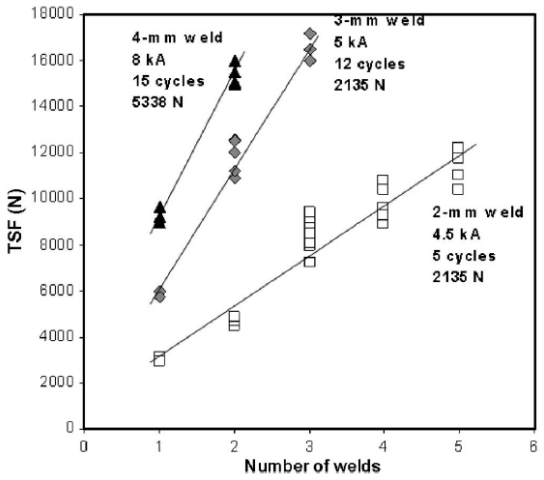

Figure 29: Variation of tensile shear force (TSF) with total number of welds at various weld diameters [47]

Marya [47] showed that for single spot weld lap shear specimens, nugget pull-out was observed at joint failure. Transitioning to the multiple spot welded specimens, as seen in Figure 30, the failure mode changed depending on the orientation of the spot weld group. Suggesting that the orientation of the spot weld groups influences the unloading of the joints.

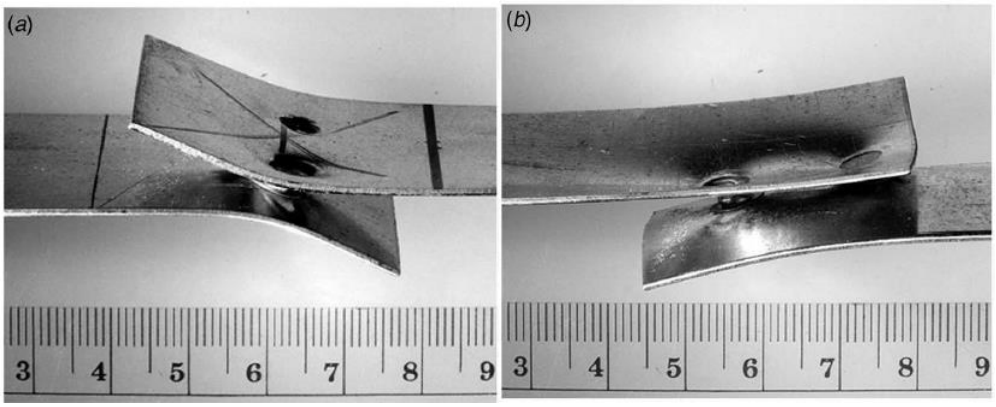

Figure 30: Two weld lap shear specimens with a 4.0 mm spot weld diameter [47]

Dynamically, the unloading behaviour of the weld largely impacts a structures ability to absorb energy. Schneider *et al.* [48] showed that the energy absorbed during the separation of spot-welds could differ considerably from the idealized deformation within the joint, contributing to the inability of finite element simulations to predict structural effectiveness in crash. Yang *et al.* [49] used a T-specimen like that shown in Figure 31 to validate the performance spot welds through extracted force-displacement data and visual inspection of the failed joints. As seen in Figure 32, the model accurately predicted the location and pre-weld failure deformation but the definition of weld failure caused the finite element simulation to largely under predict the peak force.

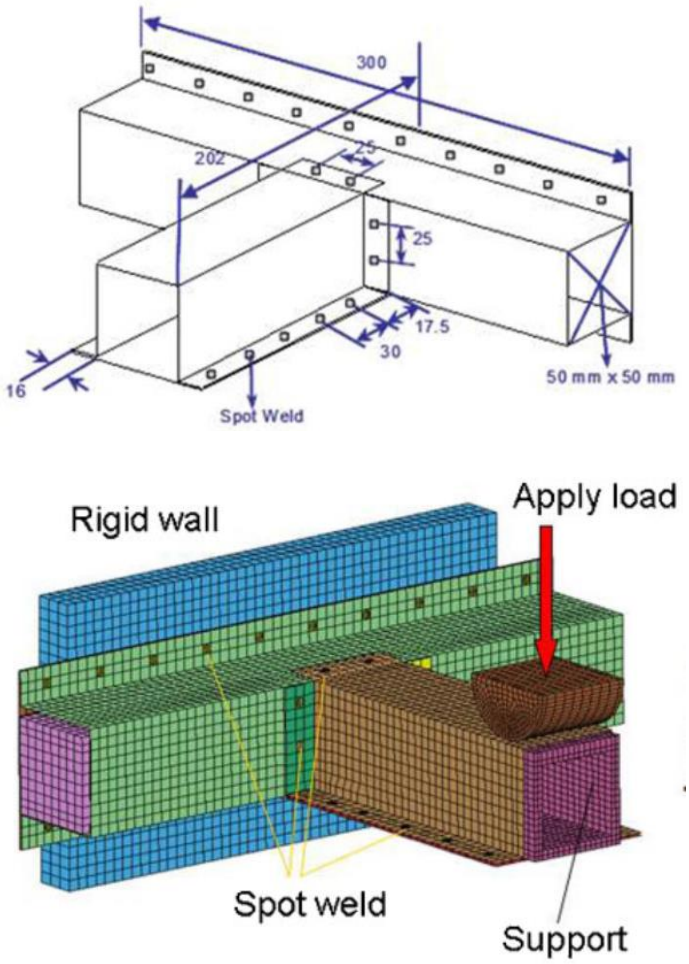

Figure 31: T-component geometry (top) and numerical simulation (bottom) by Yang [49]

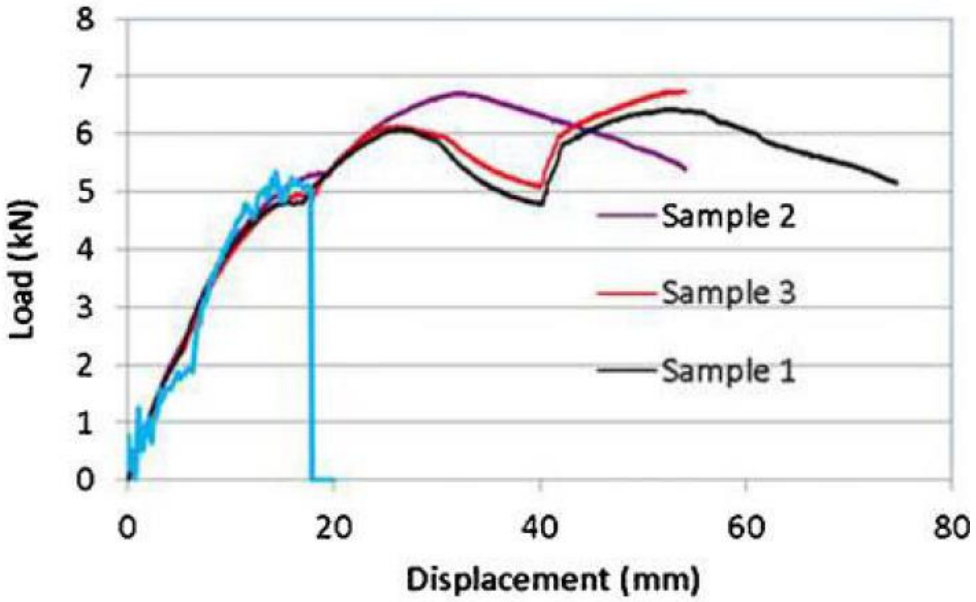

Figure 32: Comparison of load and displacement curves between testing (samples 1,2, and 3) and modelling (blue) of T-specimen by Yang [49]

While force-based failure criteria may represent the mechanical behaviour of an individual spot welded joint, in structural scenarios, these models typically produce non-physical results once a single weld fails. With the recent development of damage models that can capture the energy absorbed in joint failure, there is a new opportunity to improve numerical predictions made for RSW structures in impact simulations.

1.5 Imaging techniques

For the simulations shown in Section 1.3.2, force and displacement measurements were used to evaluate the numerical models. This is a macroscopic approach to characterizing the joint. To truly capture the mechanics that occur during an experiment, imaging techniques are required. In Section 1.3.3, Digital Image Correlation (DIC) was applied to the welds so that the strain field around the weld could be evaluated during the test and compared to the numerical predictions. Recently, there has

been interest in using both DIC and Infrared thermography as complementary imaging techniques to evaluate the thermomechanical behaviour of materials. While there are many examples of using DIC to characterize RSWs, not much thermography has been done to analyze the thermomechanical state of the welds during deformation. Since both DIC and Infrared thermography are employed over the course of the thesis, this section serves as a summary of each technique.

1.5.1 Base concepts of Digital Image Correlation

DIC is used to measure the material displacement field during a test by tracking the movement of a speckle pattern on the surface of the test specimen [50] as shown in Figure 33. This is done by comparing two images which represent the deformed and undeformed object. Each of these images are defined by a gray level distribution where each pixel can be tracked from the reference image to the deformed image thus determining the displacement field. Since the gray value of a pixel is not unique between two images, more information is required that is found in the group of pixels surrounding the pixel of interest called subsets. The tracking of each pixel is based on optimizing a specific correlation function representing the difference of the subset from undeformed to deformed state.

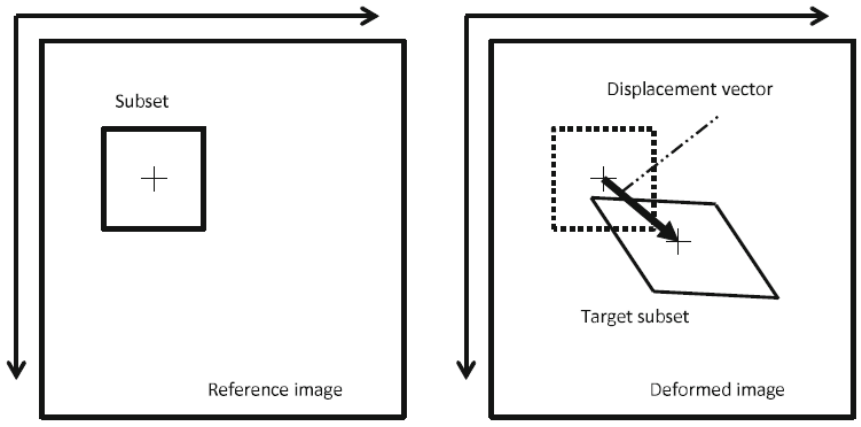

Figure 33: Principle of the subset-based DIC, tracking of a pixel from reference to deformed image [50]

The displacement measurements are then used to calculate the strain over the region of interest. There are three main parameters that affect the quality of the strain measurement; the pixel size, step size, and strain filter. Since the number of pixels on the cameras senor is fixed, the field-of-view ultimately controls the physical size of each pixel. Field-of-view is a function of camera sensor size, focal length of the lens, and working distance as shown by Figure 34. All of these parameters may be adjusted by modifying the experimental set-up but once a test is conducted they are fixed. Strain is a relative displacement over a gauge length that is calculated through numerical differentiation that can increase the noise contained in the computed value. To counter this noise, smoothing is done using local polynomial smoothing [51] over the Virtual Strain Gauge (VSG) as shown in Figure 35. Since subsets are used to determine the displacement of each pixel, not every pixel is used to calculate the strain, alternatively a step size is defined in which the strain tensor is calculated at each pixel a distance of one step size apart. The strains are then smoothed over a square called the VSG with a side length of strain filter times step size such that the measurement point is at the center of the VSG.

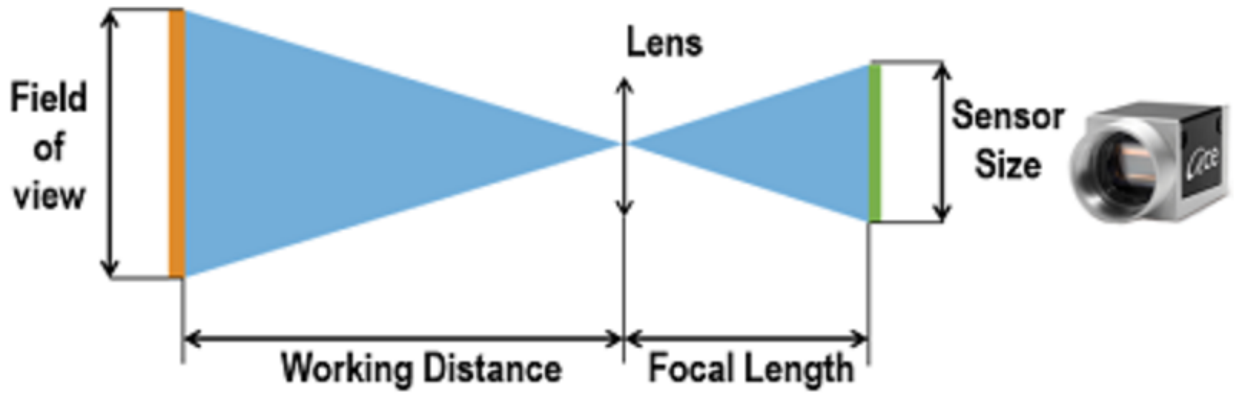

Figure 34: Camera field of view diagram [52]

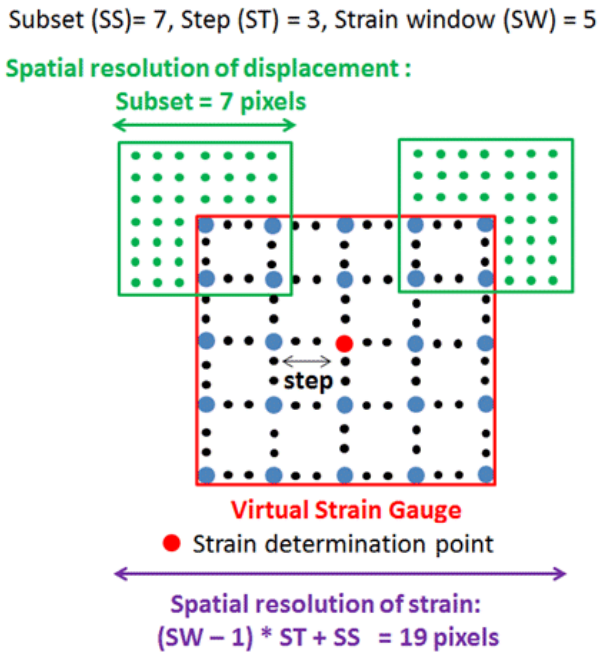

Figure 35: Visualization of Virtual Strain Gauge [51]

1.5.2 Base concepts of Infrared Thermography

The first law of thermodynamics states that the increase in the amount of energy stored in a control volume must equal the amount of energy that enters the volume minus the amount of energy that leaves [53]. This relationship is quantified by Eq. (2) where ΔE_{st}^{tot} is the change in the total energy of the system, Q is the net heat transfer to the system, and W is the net work done by the system. Strain energy is the energy required to deform an object that is quantified by Eq. (3) where U is total strain energy in the system, P is the force required to deform that system, and x_1 is the elongation produced by the applied load. If Eq. (2) is divided by the volume (V) of the system the strain energy is determined in terms of stress (σ) and strain (ε) as shown by Eq. (4). According to Eq. (2), the energy enters a control volume must exit, and if we consider strain energy as mechanical work input into the system that energy must dissipate through heat.

$$\Delta E_{st}^{tot} = Q - W \tag{2}$$

$$U = \int_0^{x_1} P dx \tag{3}$$

$$u = \frac{U}{V} = \int_0^{\varepsilon_1} \sigma d\varepsilon \tag{4}$$

Therefore as a material plastically deforms its temperature must rise to dissipate the mechanical work done. Using a thermal camera the temperature field in a region of interest may be monitored. The FAST-IR-2K [54] developed by Telops Inc. monitors the thermal state of the specimen by measuring the amount of radiant power emitted from a particular area within a given solid angle [55]. Since none of the materials characterized in this thesis are black bodies, the surface radiative property know as emissivity must be defined. Emissivity is the ratio of the radiation emitted by a surface to the radiation emitted by a blackbody at the same temperature. Since the thermal camera measures the emitted power from the heated specimen, properly characterizing the emissivity is critical for accurate temperature measurements. By using the thermal camera to monitor the test specimen over the experimental event the distribution and quantity of mechanical work can be visualized.

1.6 Current Work

As mentioned in section 1.3, the modelling of a spot weld and the effects of the softened HAZ in tailor hot stamped materials has been investigated in several studies. However, as discussed in section 1.4, there is limited literature that investigates the fracture behaviour of spot weld groupings in hot stampings and how structures respond to the progressive unzipping of spot welds. While a single beam element using a force based failure criterion is the simplest and most efficient modeling approach, when applied to structures, the joints may rapidly unzip after joint failure is initiated. As described in section 1.3.3, damage models to define the failure of the parent material and nugget can

significantly improve the fracture predictions at a coupon level but there has been limited application of this methodology to hot stamped automotive structures.

Both DIC and Infrared Thermography have been applied to material characterization to measure the thermomechanical state of a deforming material but there has been little application to RSW mechanical testing. Each of these methods offer new opportunities to obtain a local understanding of the mechanics of the deformation of a RSW. At a coupon level, these techniques could be used to evaluate the load sharing between the various materials present in the weld region. In automotive crash structures, infrared thermography could be applied to determine when and where strain energy localizes and fracture initiates. Each of these techniques will be applied in this thesis to characterize the mechanics occurring during RSW deformation.

In this thesis, the objective is to investigate the mechanical behaviour of RSW joints in various tailored hot stamped steel grades. This will be done using hardness, DIC, infrared thermography, force, and displacement measurements. Hardness maps will be used to evaluate the material properties within the welded region. DIC and Infrared Thermography will be applied to understand how load is shared between the various materials in the welded region. Force and displacement measurements will be used to evaluate accuracy of numerical models of the welded coupons and structures

In order for the automotive industry to fully utilize the capabilities of IDH components, properly capturing progressive spot weld rupture is critical. Within this thesis, a spot weld modelling technique is developed based upon extracted data from several test specimens representing different loading conditions. IDH will be employed to produce three USIBOR® 1500-AS tailored grades of varying strength and ductility. These conditions were obtained in coupon and hat channel specimens that were then spot welded together. The process of obtaining and characterizing the parent material for all test specimens and the mechanical testing of the grades is examined in Chapter 2. The

mechanical test plan of RSWs includes lap shear, cross tension, spot weld tensile, V-bend, and Caiman tests which are discussed in Chapter 3. To calibrate the spot weld model used, in Chapter 4, the experimental results from lap shear, cross tension, spot weld tensile, and V-bend specimens are presented. Chapter 5 focuses on the experimental results of the coupon level tests and the calibration of the inverse finite element models. The experimental data gathered from Caiman tests are then shown in Chapter 6 and the simulations are discussed in Chapter 7. The thesis concludes in Chapter 8 that provides a discussion and recommendations for future work.

2.0 Specimen preparation and characterization

2.1 Base Material

In this work, USIBOR® 1500-AS, a boron steel manufactured by ArcelorMittal, was used as the base material. To prevent oxidation during hot stamping, USIBOR® 1500-AS features an aluminum silicon coating that forms an intermetallic layer on the steel when it is heated [56]. The chemical composition of the material is shown in Table 1.

Table 1: USIBOR® 1500-AS Chemical composition

Element	**Composition (weight %)**
Carbon	0.2303
Silicon	0.23
Manganese	1.19
Phosphorus	0.016
Sulfur	0.001
Aluminum	0.040
Chromium	0.19
Copper	0.01
Molybdenum	0.00
Nitrogen	0.0055
Nickel	0.006
Niobium	0.001
Titanium	0.030
Boron	0.0030
Vanadium	0.002
Calcium	0.0016
Iron	Remaining

In the as-received condition, the microstructure is a mix of ferrite and pearlite which has a yield strength of 410 MPa and an ultimate strength of 566 MPa. Bardelcik [3] showed that by heating the steel to the austenite temperature range then cooling it at a rate of at least 30°C/s, a fully martensitic microstructure could be obtained. If a lower cooling rate is applied than the final microstructure becomes a combination of martensite, ferrite, and bainite.

2.2. Quenching

Prior to analyzing the deformation of spot welded joints on a structural level, coupon level tests were required to characterize the behaviour of a single joint in various loading conditions. Tailored components typically include multiple microstructures in a single part and therefore, a variety of microstructures were needed to determine how changes in the constituent composition of the parent material affected the performance of the weld. The tailoring conditions considered for 1.2 mm and 1.6 mm thick sheet corresponded to a fully quenched condition with a cooled die and quenching using dies at 400°C and 700°C. For this work, a heated die was developed to alter the cooling rate that the material experienced post austenization. Quenching was achieved by heating the material in a furnace above the austenization temperature of 850°C to 930 °C, transferring it to a flat die, and clamping the sheet in a hydraulic press. The system used to execute this process is shown in Figure 36.

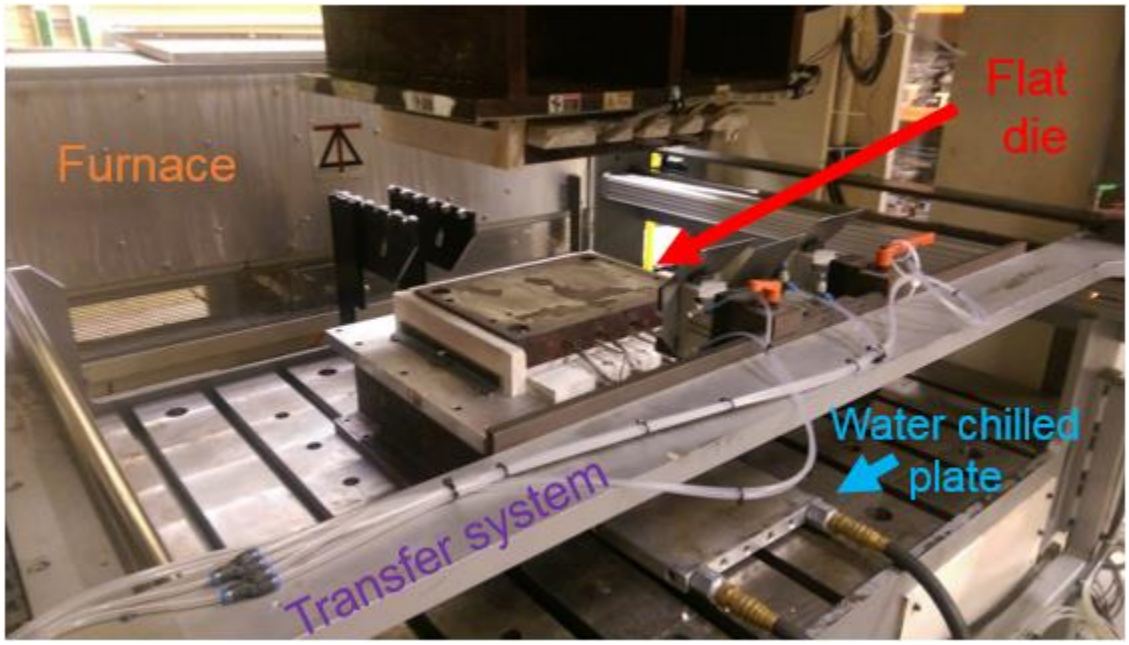

Figure 36: Quenching apparatus

The blank geometry used for quenching was a 304.8 mm by 304.8 mm square with 38.1 mm of material removed around the perimeter of the sheet prior to extracting specimens to ensure all samples had a consistent microstructure. The first step of the quenching process involved heating the blank above the austenization temperature in an 18 kW furnace from Deltech Inc. shown in Figure 37. The internal dimensions of the furnace were 1575 mm x 1220 mm x 203 mm. The furnace had six heating elements, three on the top and three on the bottom that spanned the entire 1575 mm x 1220 mm area. There were three separate control groups in the front, middle, and back of the furnace which ensured even heating within the furnace. During operation, the furnace maintained a temperature of 930°C and the blanks were left inside for 6 minutes to ensure a fully austenized microstructure [16]. To move the blank into the furnace and onto the press, a moving tray is incorporated within the furnace that is attached to pneumatic cylinders. Blanks were placed onto the tray and then moved into the oven for pre-heating. The heated blanks were removed from the oven by the tray prior to transferring to the quenching tool that was located adjacent to the furnace.

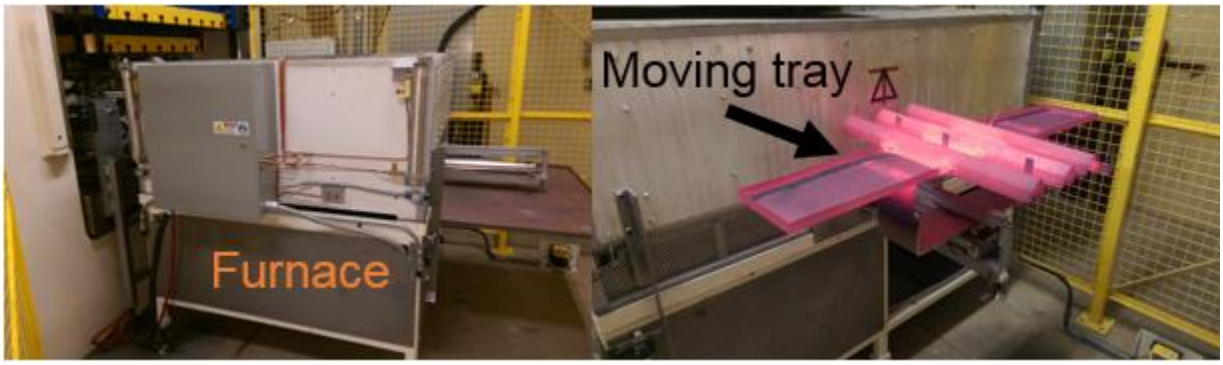

Figure 37: Furnace and blank tray

To transfer the blank from the furnace onto the flat die, a pneumatic transfer system was used which is shown in Figure 38. When the tray from the furnace fully extended towards the press, the transfer system grips the blank with pneumatic grips and pulls the blank over the flat die. Once in

position over the die, the grips release and an air cylinder pushes the blank out of the grips. The transfer process concluded by fully retracting the transfer system and cycling the press stroke

Figure 38: Gripper incorporated within the blank transfer system

All of the quenching and forming in this work was performed on a hydraulic forming press fabricated by Macrodyne Technologies Inc. The press was capable of exerting up to 900 tonnes of force using its main cylinder and also contained four smaller "kicker" cylinders that can generate up to 60 tonnes of force. For quenching on the flat die, a force of 60 tonnes was used to obtain an approximate contact pressure of 7 MPa on the blank.

The flat die set used in this work consisted of two identical halves. Each die was held at a constant temperature through the use of PID controllers and four 1900W, 600V resistance heaters that had a 19 mm diameter and 304.8 mm length. Each die had two control zones and PID controllers to monitor the temperature of the die via thermocouples and adjust the electrical current fed to the heaters to maintain the desired temperature. ZIRCAL-95 insulation board that was 25.4 mm thick was wrapped around the die to promote a more even temperature distribution across the die surface when it was heated.

Fully martensitic material was made by leaving the dies at room temperature and quenching the sheets for 10 seconds. Between cycles, an aluminum water chilled plate was put between the dies

to maintain room temperature (25°C). For the heated conditions, the die set was closed between press cycles to reduce heat loss. Bainitic/ferritic steel was produced by maintaining the die at 700°C and holding it for 4 seconds. The intermediate condition was created by heating the dies to 400°C and holding the sheet for 4 seconds. Once removed from the flat die, the sheets were left to air cool on a rack.

To validate the temperature distribution on the surface of the flat dies, a FLIR® infrared camera was used to capture the thermal state for the 400°C and 700°C die conditions shown in Figure 39. Note that the control thermocouples in the dies were maintained 50°C hotter than the intended temperature to ensure the tool surface was at the desired temperature at the end of the transfer sequence. To capture these thermal images, the dies were opened and the images were taken from the front once the press fully stopped. In the 400°C die condition, there was a large region in the back of the die which was at 450°C with a slight decrease to 400°C observed towards the front of the die. Width-wise, the temperature was relatively consistent within the heated region but strong temperature gradients down to 350°C were observed around the mounting bolts. For the 700°C die condition, the temperature was not as evenly distributed. Within the heated region, the temperature varied from 725°C to 675°C with the same gradients observed around the edges of the die that were observed at the 400°C die condition. To avoid inconsistent results, only the space between the black lines was used and 38.1 mm of material was removed from the edge of each quenched sheet to ensure homogeneous material composition.

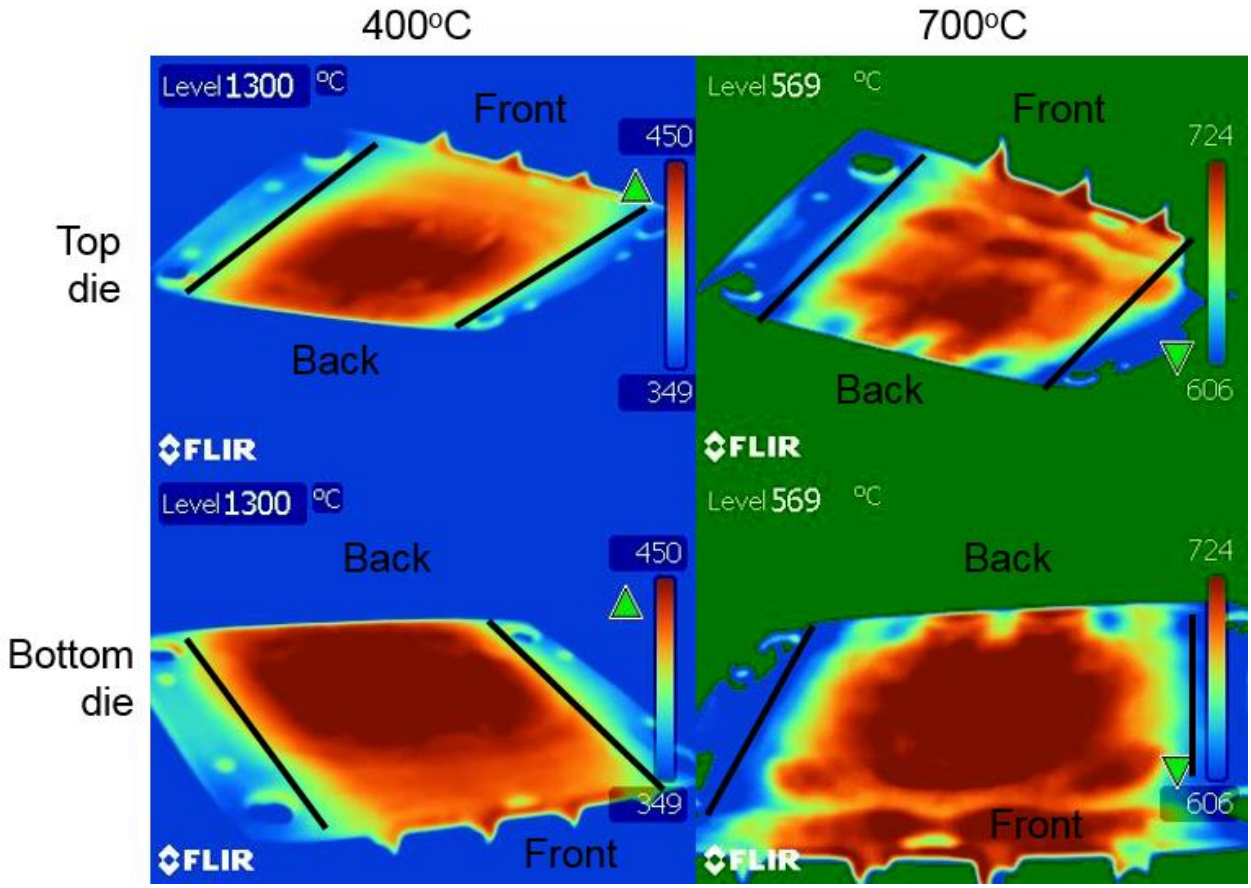

Figure 39: Temperature distribution of top and bottom dies at 400 °C and 700 °C quench conditions. The black lines are to show where the material was dropped when transferred from the oven and samples were only extracted from the quenched blanks in the regions where the temperature was relatively uniform

2.2.1 Base metal tensile testing

To determine the strength of each quench condition, tensile specimens, shown in Figure 40 based on Japanese Industrial Standards (JIS) [57] were extracted from the quenched flat sheets via laser cutting. This cutting method was used so that the specimen would have a smooth edge along the gauge length, prohibiting fracture from initiating on the edge of the specimen that could occur with shearing or water-jet cutting.

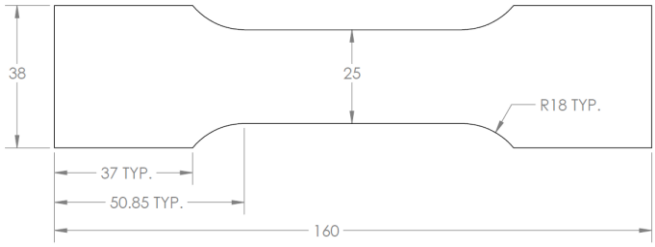

Figure 40: Tensile specimen geometry [57]

These tensile specimens were tested using a 100 kN MTS Criterion Model 45 tensile frame that is shown in Figure 41. All tensile tests were performed at a strain rate of 0.001 s^{-1}. DIC was utilized to measure displacements and compute surface strains for these experiments. For all tensile tests, two Point Grey Research GZL-CL-41C6M-C 5.0 MP cameras with 180 mm lenses was used to record 10 images with a resolution of 15 pixels/mm.

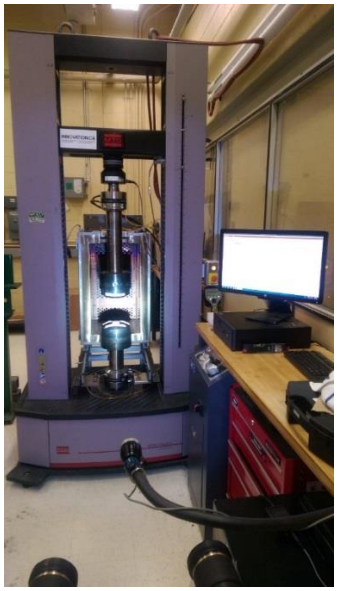

Figure 41: MTS Criterion Model 45

To capture and process the images, the software package from Correlated Solutions was used [58], VIC SNAP 2009 captured the images and VIC-3D 7 performed analysis. Rustoleum Painter's Touch white primer was used on each specimen to create a base coat, on which a random speckle

pattern was applied using Rustoleum Painter's Touch flat black spray paint. The speckles were used by the DIC software to compute displacement and strain by comparing images of the deformed specimen to a previous state. When post-processing the images, a subset of 29, step size of 1, and strain filter of 7 pixels was used resulting in a Virtual Strain Gauge Length (VSGL) of 0.5 mm.

The data collected from tensile testing is shown in Figure 42. Reviewing the data, the quench condition had a large impact on the results. The fully quenched (25°C die), 400°C, and 700°C tailored materials showed ultimate strengths of 1548 ± 26 MPa, 817 ± 18 MPa, and 671 ± 15 MPa. While the strength was relatively constant between the different thicknesses, the amount of deformation observed before necking was slightly larger for the 1.6 mm material compared to the 1.2 mm sheet. These results highlight the effect of in-die heating on the ductility and strength of as-quenched materials.

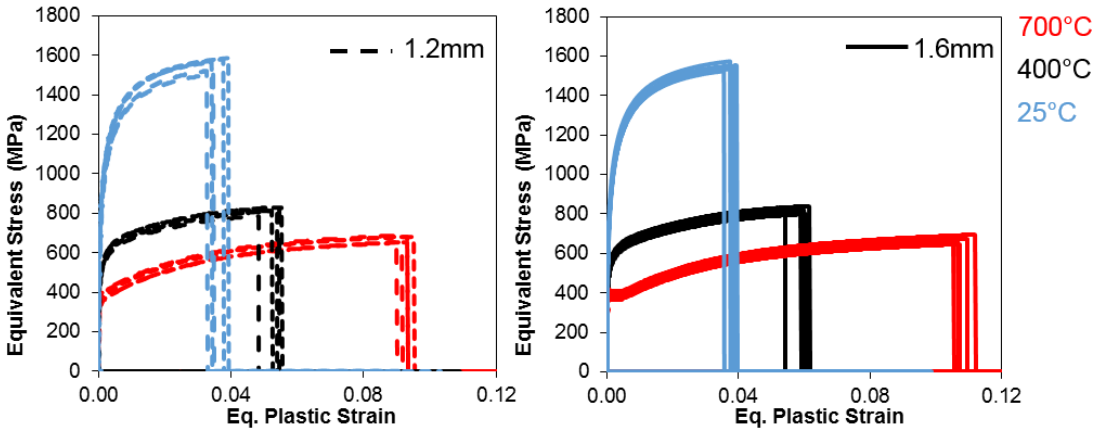

Figure 42: True stress-strain curve for all parent metals in uniaxial tensile tests

2.2.2 Base metal V-bend testing

Although the JIS experiments were sufficient to characterize the material strength, due to the onset of tensile instability these results were not a useful for measuring of ductility. Necking is undesirable in material testing since it causes the strain state at fracture to deviate from the desired

condition and measuring strain within the region is non-intuitive. Bending produces a plane strain loading condition which suppresses necking and the strain measurements can maintain a constant ratio between major and minor strain until fracture initiation. In bending there is a through-thickness strain gradient from tension on the outer surface to compression at the inner radius of the bend. The strain gradient helps to delay or suppress a tensile instability from occurring [59, 60]. To that end, plate bending tests were conducted on 40 mm squares specimens using the apparatus shown in Figure 43. During the experimental event, the punch was stationary and the rollers moved downwards at a speed of 20 mm/min. The rollers were spaced by 2.9 mm for the 1.2 mm and 3.7 mm for the 1.6 mm material in accordance with VDA 238-100 [61]. No lubrication was used on the punch and it had a radius at the tip of 0.4 mm. Load and displacement were measured in the actuator and stereographic DIC was taken on the top surface. These specimens were subjected to the same surface preparation as the tensile specimens and a VSGL of 0.5 mm was used for post processing.

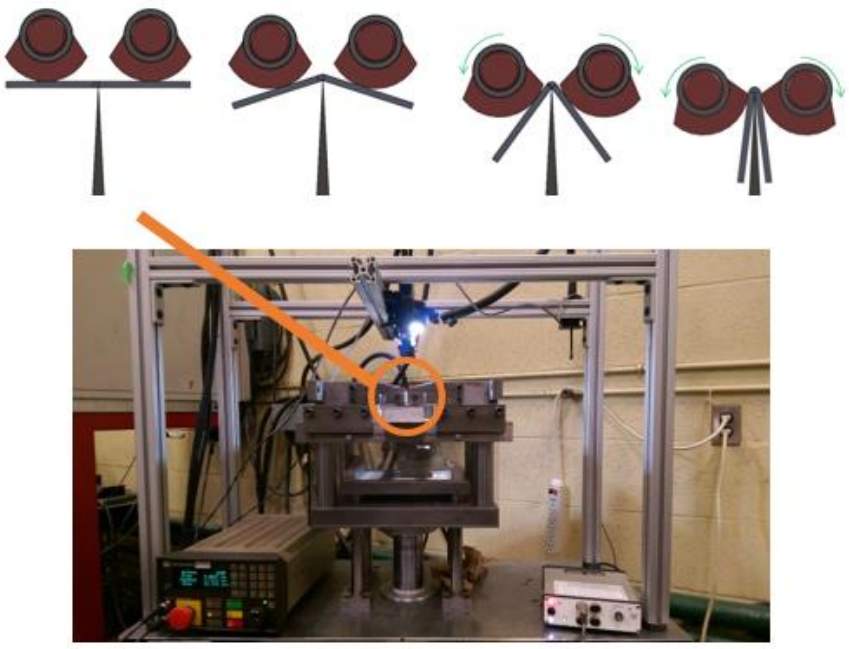

Figure 43: Plate bending apparatus

The failure moment was estimated by observing the peak force and then waiting until the load dropped by 30 N. At this instance, the equivalent strain and bend angle were measured and used to compare the ductility of each material condition. The bend angle was determined using the VDA relation [61] between roller radius (*R*), sample thickness (*a*), punch stroke (*S*), and roller distance (*L*) shown in Eq. (4). The variables *h*, *g*, and *i* are functions of the test geometry and the expressions can be found in VDA [61].

$$\theta = 2\left(\tan^{-1}\left(\frac{\sqrt{(R+a)^2-\left(\left(\frac{-\sqrt{(h^2-4g*i-h}}{2g}\right)+\left(R+\frac{L}{2}\right)\right)^2}-(R+a-S)}{\frac{-h-\sqrt{h^2-4g*i}}{2g}}\right)\right) \quad (5)$$

The strain, force, and displacement measurements for all material conditions are shown in Figure 44 and Figure 45. As expected, the martensitic condition was consistently the strongest material and exhibited rapid load drop after reaching peak force. The 400°C die quenched material was roughly one-half of the strength of the martensitic material but was able to withstand higher strain levels before the onset of cracking as it has a higher ductility than the martenisite. The 700°C material was the most interesting because it exhibited a higher hardening rate in the 1.6 mm condition causing it to be more ductile and higher strength than the 1.6 mm 400°C die quenched material. Looking at the strain paths measured during the experiments (Figure 45), the V-bend specimens were subjected to plane strain loading. This loading condition is useful because this is the strain state that sheet materials tend towards prior to fracture. The fully quenched metal was the least ductile material showing fracture strains about one-half of the strain of the heated die conditions when the VDA load threshold was met. Whereas the 400°C and 700°C die quenched materials were able to withstand similar strains.

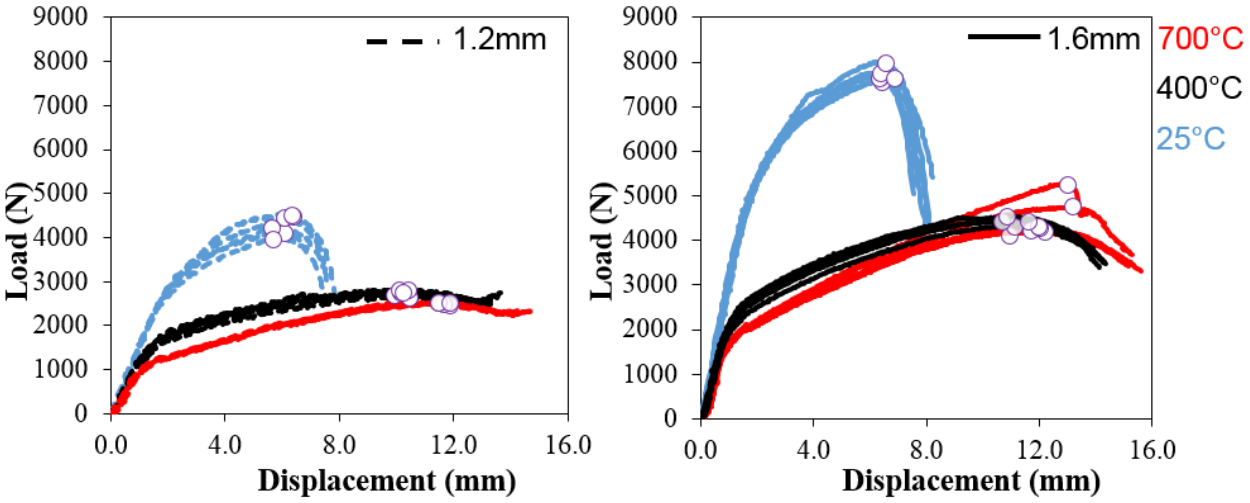

Figure 44: Force displacement measurements from V-bend testing with VDA load drop point marked

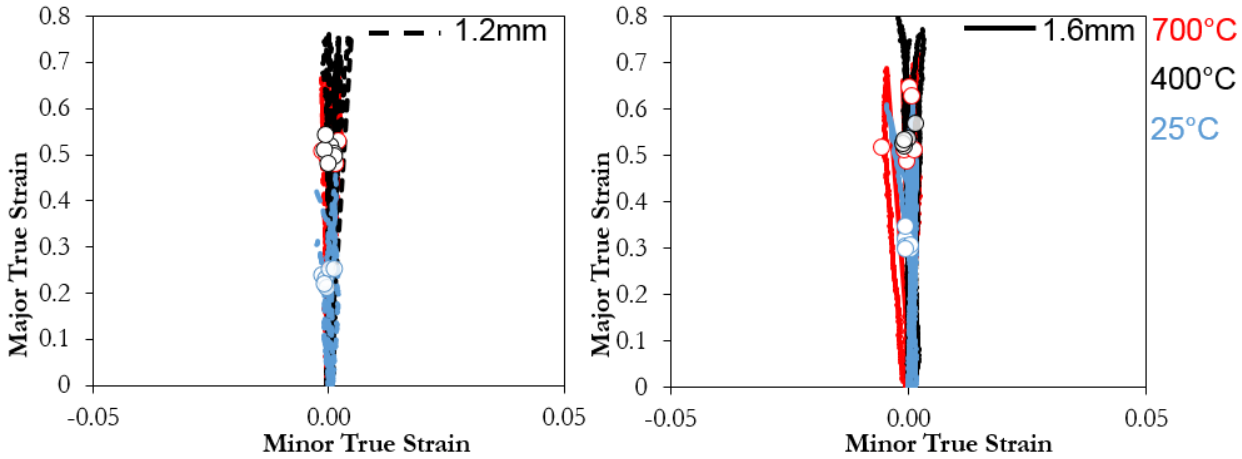

Figure 45: Strain paths for V-Bend testing with VDA failure point marked

Table 2: Summary of Plate bending tests

Material	Load at VDA Threshold (N)	Major Strain	VDA Bend Angle (°)
1.2 FQ	4261±233	0.23±0.02	51±3
1.2 400	2723±74	0.51±0.02	96±3
1.2 700	2478±36	0.50±0.02	113±3
1.6 FQ	7688±160	0.31±0.02	54±2
1.6 400	4346±200	0.54±0.02	103±5
1.6 700	4481±443	0.55±0.07	117±8

2.3 Hat channel forming

The main goal of this work was to investigate the unzipping behaviour of spot weld groups in tailor hot stamped structures. To achieve this objective, three configurations of hot stamped hat channels were produced and are shown in Figure 46. These tailoring schemes were used to investigate how ductility (quench condition) affected the unzipping behaviour of spot weld groups. Each formed part had a top hat cross section consisting of a C-channel with flanges on each side. The formed parts had a length of 600 mm, C-channel width of 60 mm, and total width of 125 mm.

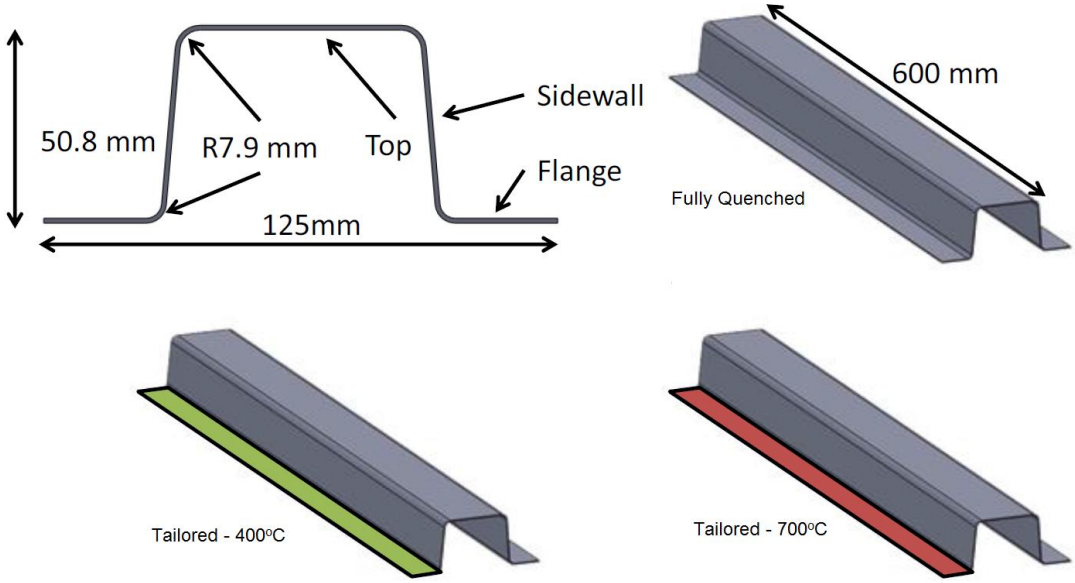

Figure 46: Hat channel tailoring conditions

The dimensions of the pre-formed blank were 590 mm x 200 mm as illustrated by Figure 47. The blank also included two tabs on both ends, one tab had a triangle slot while the opposing end had an obround hole. The holes in the tabs were used to align the blank on pins in the tooling and allowed for easy handling of the part during the forming process.

Figure 47: Hat channel blank geometry in millimeters

The same furnace used to austenize the blanks and the transfer system discussed in section 2.2 was also used in the rail forming process. The same transfer system from section 2.2 was used to move the blanks from the furnace to the die set but adjustments were made to the guide system to ensure the blank aligned within the die properly as seen in Figure 48.

Figure 48: Hat channel tool set installed in Macrodyne press

The tooling used to create the hat channels was designed by George [4] as part of the broader scope of the hot stamping project and is shown in Figure 49. The tool set consisted of three components, the die, binder, and punch. The die on the top half of the tool set was broken into two regions, a water-chilled area that formed the hat channel and a heated region that contacted the flanges.

The cooled punch was mounted to the bottom half of the tool set. The binder moved downwards with the press ram such that the sheet was drawn into the cavity as the press cycled. The binder was heated and mounted on four nitrogen cylinders that produced a constant pressure of 10.3 MPa. The diameter of the cylinders was 25.4 mm, that generated a total force of 6.0 kN when compressed by the die.

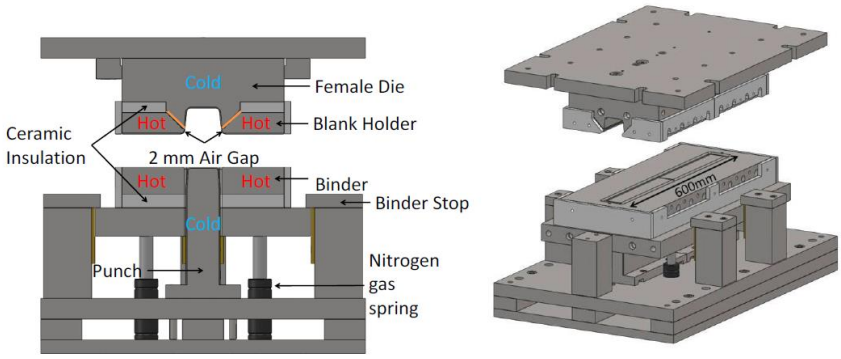

Figure 49: Tooling schematic showing heated and cooled regions of tool to produce tailored hat section from George [16]

Water was pumped through the cooled punch and die cavity to maintain a steady state temperature of 25°C. To insulate the chilled regions of the die from the heated flange portions, a 2 mm air gap was designed into the tooling as shown in Figure 49 [16]. The heated regions were held at a constant temperature through the use of PID controllers and several 700W, 600V heaters that had a 19 mm diameter. In the blank holder there were 16, 76.2 mm long heaters and in the binder there was 16, 101.6 mm long heaters. The heaters and thermocouples were wired such that there were 4 control zones in the top and bottom halves of the tool. To heat the tooling, a ramp function was used and once the desired temperature was reached the current would be adjusted to maintain constant temperature.

The heated parts of the tooling were insulated by 12.7 mm thick ZIRCAL-95. This material had a thermal conductivity of 0.31 W/mK at 200°C, 0.29 W/mK at 400°C, and 0.27 W/mK at 600°C

[62]. The ZIRCAL-95 can be seen in Figure 48 as the white coloured sheets surrounding the tooling. These external layers prevented excessive heat loss when the tooling was maintained at 400°C and 700°C.

Overall the forming process consisted of four stages. To start, the pre-formed blank shown in Figure 47 was placed on the oven rack shown in Figure 37 and placed within the furnace and heated to 930°C. After 6 minutes, the blank was transferred from the oven to the press by the pneumatic transfer system. Once placed on the binder, the female die was pressed over the male punch to form the part at a speed of 254 mm/s [4]. For the fully quenched material, the formed part was held in the die for a total of 10 seconds. In the 400°C and 700°C tailored flange specimens, the parts were held in the die set for a total of 4 seconds.

As a measure of temperature distribution across the die surface, a thermal camera was used to capture the state of the die as the press opened for the forming cycle. Still images are shown in Figure 50 with the emissivity set to 1.0 for each forming condition. Looking at these images, the temperature distribution was relatively uniform. In Section 1.5.2 it was shown that emissivity largely effects the temperature of a pixel. As mentioned in section 3, thermocouples were used to control the temperature of the die sets as they were heated and were set to 400°C and 700°C for the tailored flange conditions. When applying an emissivity of 0.8, the temperatures in the image did not match the thermocouple. The emissivity value was then reduced systematically from 0.8 until a value of 0.55 when the results converged. While the root of this problem was not firmly identified, the tool set did experience a considerable amount of oxidation which has been shown to drastically alter the emissivity of steel [63].

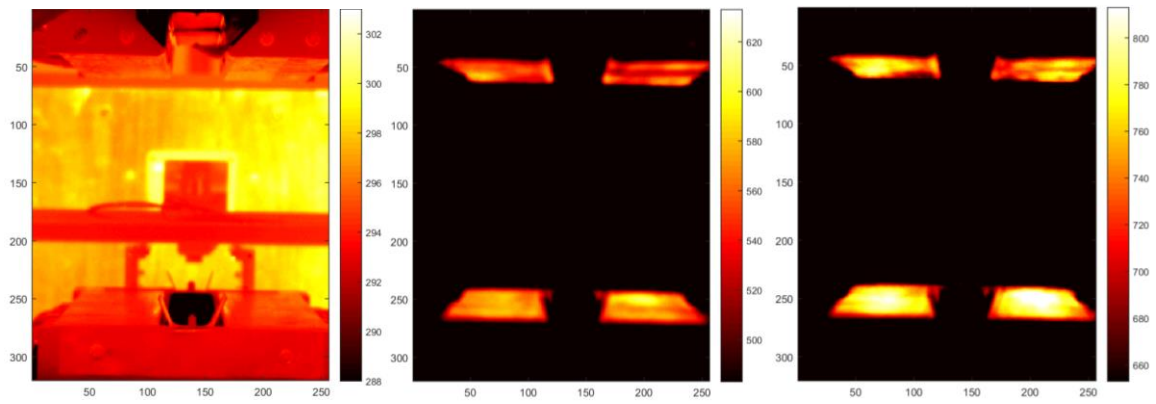

Figure 50: Thermal images of the hat channel die set at room temperature (Left), 400°C (Center), and 700°C (Right) tailored flange conditions

While the thermal images helped to inform on the temperature during forming they did not serve to validate the forming process. Once the hat channels were formed, Vickers micro-hardness measurements were taken to determine the hardness distribution through the cross section of the part. Strips of the hat channel were removed via laser cutting as shown in Figure 51. The strips were then further sectioned with a water cooled abrasive saw and mounted for precision grinding as shown to the right.

Figure 51: Hat channel hardness strip (left) and mounted specimen (right)

The sectioned hat channels were mounted in epoxy resin and polished using silicon carbon paper in grits of the following order: 120, 220, 500, 800, 1200, 2400, and 4000. After sample

preparation, hardness measurements were taken every 2.5 mm down the centerline of the cross-sectional area. These measurements were used to define the distribution of hardness through the area of the part. This work was completed on a Nanovea CB500 automated Vickers micro-hardness tester that used a 500g indenter load and 15 second dwell time. The Vickers micro-hardness is dependent upon the indenter load so it is important to note that unless otherwise specified, all hardness measurements correspond to a 500g indenter load.

The hardness measurements shown in Figure 52 were taken with the intent of investigating the resulting microstructure throughout the as-formed part for the different hot stamping configurations. They were also used to map the microstructural properties throughout the as-formed hat channels numerically. The fully quenched material showed an average hardness of 495 HV throughout the entire cross-section with little variability. This hardness indicated that the as-formed fully quenched channels contained a purely martensitic microstructure. In the 1.2 mm 400°C tailored flange hat channel, a hardness gradient existed in which the hardness ranged from 280 HV to 325 HV in the flange and increased up the sidewall towards the top portion. For the 1.6 mm channels the hardness was closer to 260 HV throughout with the sidewall and bottom flange experiencing more aggressive hardness gradients. These hardness levels in the flange correspond to a mixed bainite/martensite microstructure, whereas the top portion was martensitic with the region in between comprising of a gradual increase in martensite content. For the 1.6 mm 700°C tailored flange hat channel, the flange exhibited a hardness of 200 HV corresponding to a ferrite microstructure, with the bottom flange and sidewall serving as a transition region to a martensitic region at the top of the channel. All the formed conditions aligned with the quenched flat sheets in the single weld work except for the 400°C tailored flange which was slightly harder than the flat sheets quenched in Section 2.2. Since the same welding parameters were used to bond these components, it is assumed that the same softening profile from Figure 54 existed at each weld within the specimen.

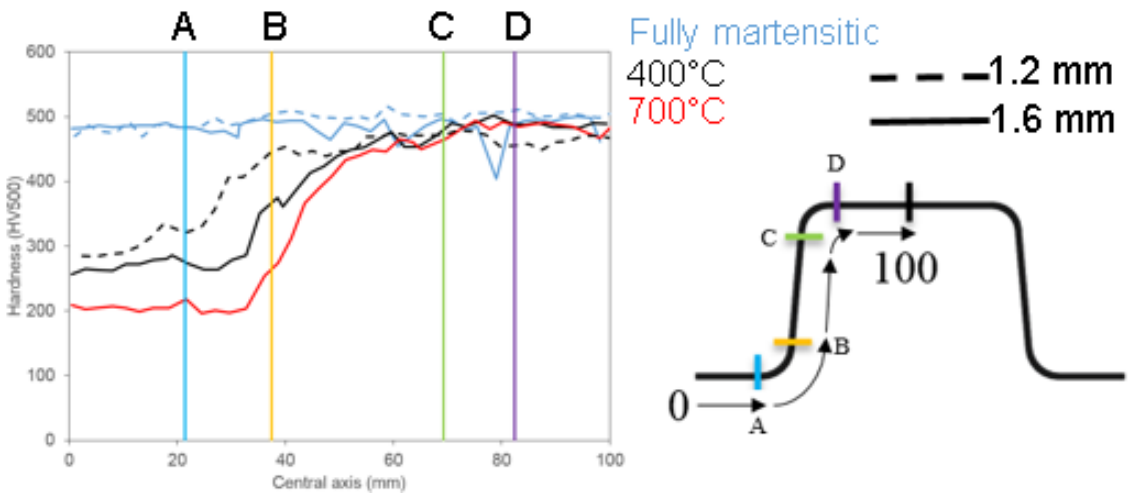

Figure 52: Hardness distribution measured through the cross section of formed channels

2.4 Resistance Spot welding

All resistance spot welding shown and discussed throughout this thesis was done by the Promatek Research Centre. For each thickness, a set of spot weld parameters was determined by the Promatek Research Centre to ensure the settings were consistent with typical industrial practices. The settings used for each material thickness is shown in Table 2.

Table 3: Resistance spot weld settings

Thickness	Pre-heat		Weld		Force (N)
	Time (ms)	Current (kA)	Time (ms)	Current (kA)	
1.2	33	8	400	7	3425
1.6	33	10	400	7	4003

As described in section 1.3.1, the spot welding process induces a thermal transient which results in a solid nugget of joined material. To investigate how this process altered the microstructural composition in and around the spot weld, through-thickness specimens were used for micro-hardness maps and microscopy.

Pairs of quenched blanks, processed using the various quench conditions described in section 2.2, were welded together using the settings given in Table 2 and 48 mm squares were removed via water jet cutting. Specimens were sectioned through-thickness using an abrasive water saw to reduce the 48 mm squares into 25mm squares and then cutting 3 mm off weld center such that, after polishing, the center plane of the weld would be measured. Afterwards, the welds were mounted in epoxy resin pucks and polished using silicon carbide paper of the following grits: 120, 220, 500, 800, 1200, 2400, and 4000.

Hardness measurements were performed at ArcelorMittal Dofasco R&D. Hardness maps across the welded cross-sections of the samples were taken using the pattern shown in Figure 53. In the through-thickness direction, measurements were spaced by a distance of 300 microns whereas in the sheet in-plane direction the spacing was 150 microns. To make the indents, a 500 gram force was used and a 15 second dwell time. After hardness testing, the specimens were polished with 6 μm, 3 μm, and 0.5 μm diamond paste so that the specimen could be etched with 2% Nital and then soaked in a 10% Sodium Metasulfite aqueous solution.

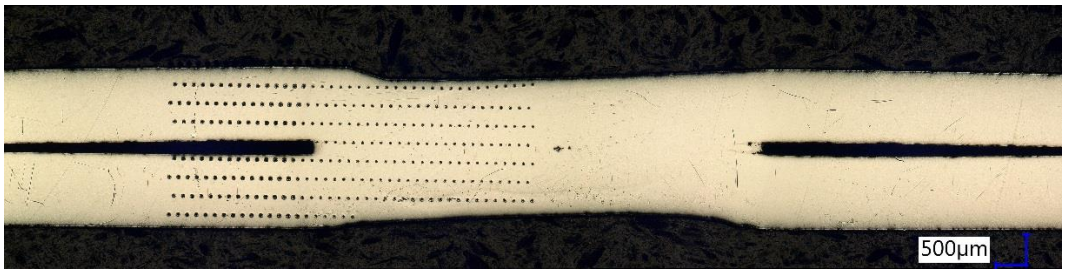

Figure 53: Resistance spot weld hardness map measurement pattern

Figure 54 shows the hardness maps measured in the welded region for each material condition and the corresponding hardness traverses are shown in Figure 55 with a summary of the data shown in Table 4. Reviewing the data, the fully quenched material exhibited the most softening, while a small degree of softening with the HAZ was seen in the 400°C material. No discernable HAZ softening was

seen in the 700°C welds. While the spot weld process parameters for each thickness were unique, the size and severity of the softened region was relatively constant for each respective quench condition.

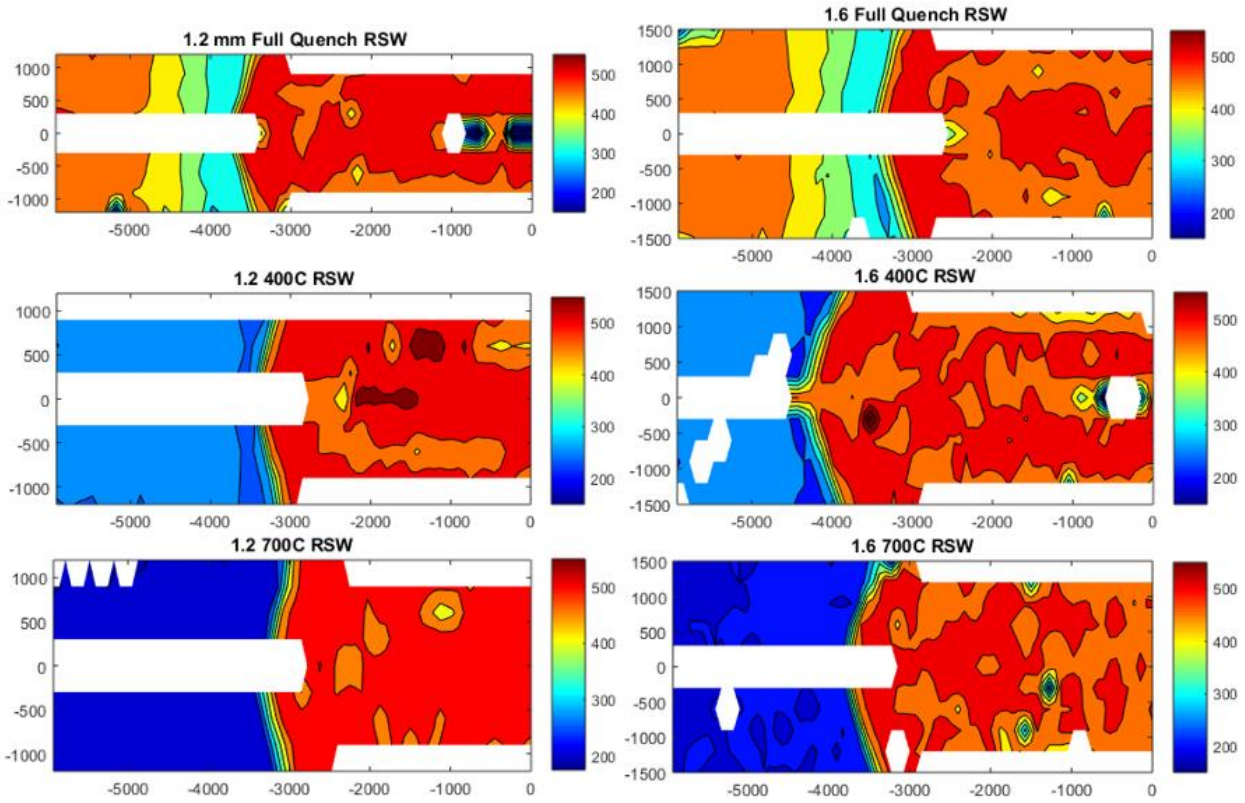

Figure 54: Hardness maps of all resistance spot welded die quenched flat sheets

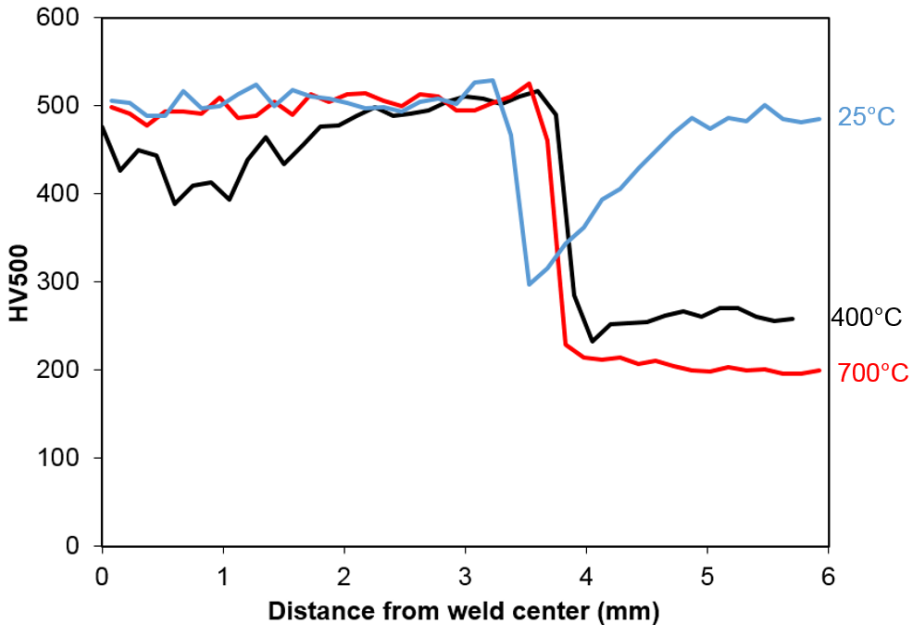

Figure 55: Traverses extracted from hardness maps

Table 4: Summary of RSW hardness maps with average hardness and variation between largest and smallest measurement in each region of the weld

Condition	Base material		Nugget		HAZ	
	Average	Variation	Average	Variation	Average	Variation
1.2 FQ	486	1.58%	504	4.30%	318	8.37%
1.2 400	262	2.44%	513	5.09%	239	2.00%
1.2 700	211	2.89%	513	3.75%	N.A	N.A
1.6 FQ	485	1.06%	496	4.44%	302	6.97%
1.6 400	262	3.38%	497	4.59%	235	2.59%
1.6 700	201	3.49%	490	6.86%	N.A	N.A

To determine the phase distribution throughout the joint, optical micrographs shown in Figure 56 were taken in the nugget, HAZ, and base metal of each material condition. In the nugget, all quench conditions showed a coarse martensitic microstructure which transitioned to a finer grain on the edges of the nugget. For the fully martensitic conditions, the subcritical HAZ served as a transition region between the bainite in the critical HAZ and the martensitic nugget. Moving towards the base metal, a gradual change was seen from the bainitic HAZ to the martensitic base metal. For the 400°C die

quenched material, a change in microstructure was observed around the weld but the affected region was much smaller and was similar to the base metal. Both the base metal and HAZ appeared to be a combination of martensite and bainite with a slight change in grain size within the HAZ. The 700°C tailored metal was unique in that there appeared to be no intermediate HAZ but simply a transition from the martensitic nugget to the base metal.

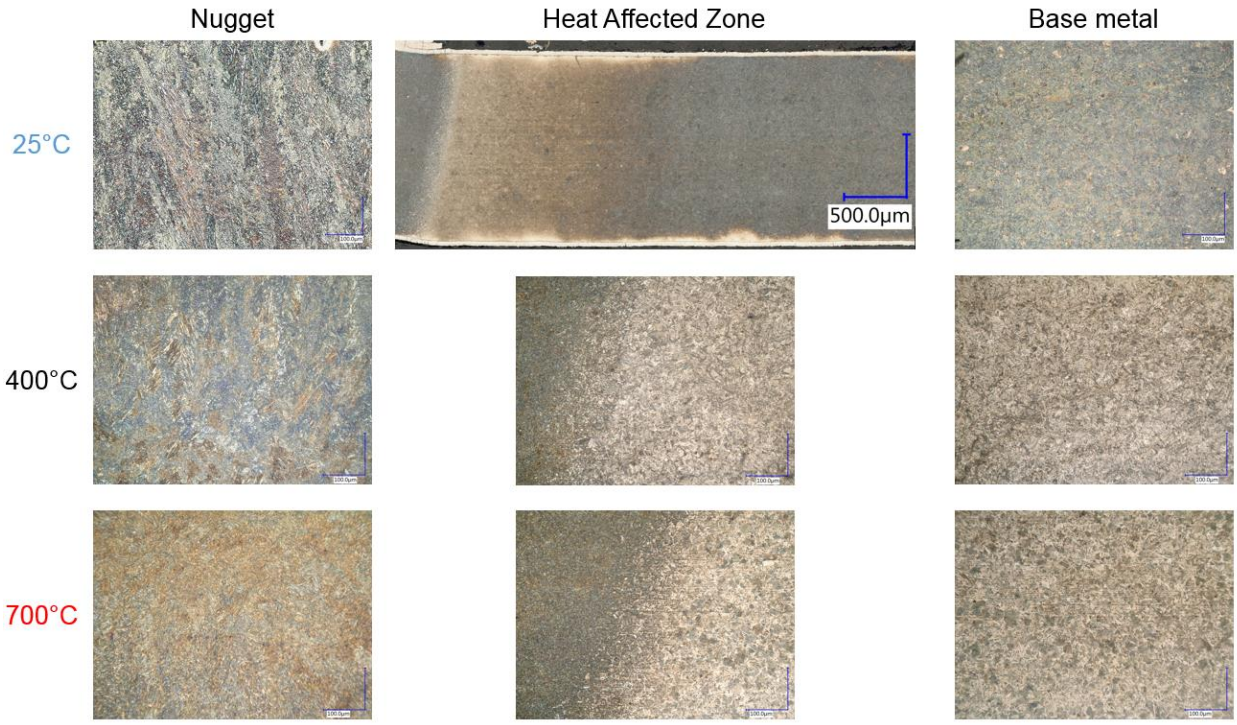

Figure 56: Optical micrographs of nugget and HAZ for all die quenched flat sheets

3.0 Spot weld mechanical testing program

To investigate the behaviour of resistance spot welded joints in IDH tailored USIBOR® 1500-AS, several assemblies were constructed using the hot stamped flat sheet and hat channels described in Section 2.0. The quenched sheets described in Section 2.2 were used to construct single spot weld coupons that subjected the joint to several different loading conditions. The hat channels discussed in Section 2.3 were used to manufacture spot weld group specimens to subject the chain of welds to Mode I (aperture) loading.

3.1 Coupon test plan

The test geometries selected to reveal the mechanical behaviour of the welded joint comprised lap shear, cross tension, spot welded tensile, and V-bend. All of these specimens were cut from flat sheets that were quenched using the flat die described in Section 2.2. The intention of the coupon test regimen was to identify the deformation and fracture behaviour of an individual spot weld under different loading conditions. These tests were performed on both the 1.2 mm and 1.6 mm material quenched using dies at either room temperature, 400°C, or 700°C. To weld the specimens, the processes described in Section 2.4 were utilized. All welding described in this thesis was performed by Promatek Research Centre.

3.1.1 Lap shear

Classically, the lap shear test is used to determine the shear strength of the welded joint. For this work, the lap shear test procedure outlined in the American Welding Society Standard AWS D8.9M:2012 [24] was used with the coupon shown in Figure 57. To fabricate these specimens, the

single part shape was laser cut from the quenched sheets and welded in the tensile shear specimen configuration.

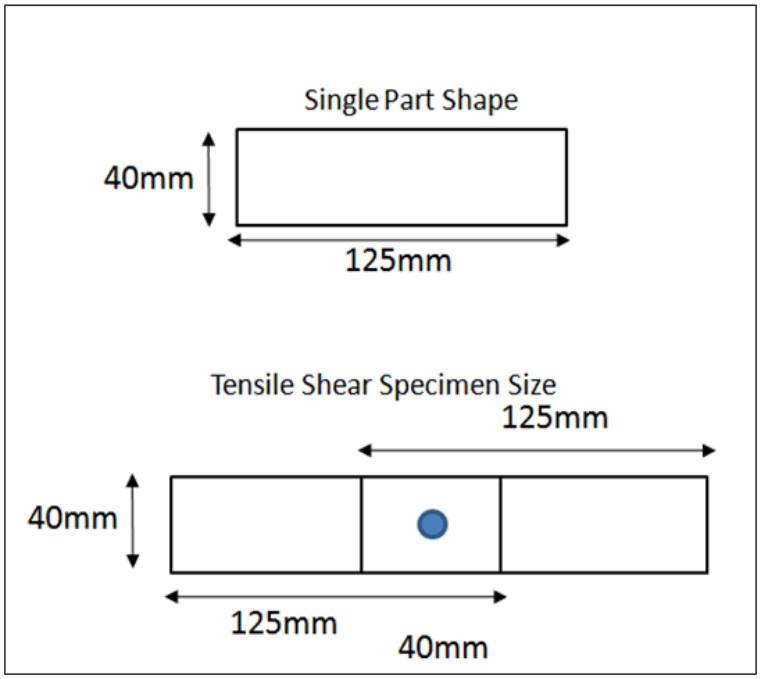

Figure 57: Lap shear specimen [64]

To test the lap shear specimens the material testing system shown in Figure 41 was used. As described in [24], shims were used to ensure the specimen was properly orientated in the grips of the machine. The knurled grips on the MTS frame were hydraulically driven and applied a constant gripping pressure of 3000 psi. The cross head on the frame was set to move at a rate of 10 mm/min upwards as per the AWS standard.

During the test, load and displacement data was measured at 500 Hz with a 100 kN load cell and a LVDT attached to the crosshead. The data was then assembled in the program TW Elite which exported the data in a comma separated text file for post-processing. After the specimens were tested, the nugget diameter was determined by measuring the minimum and maximum nugget sizes and averaging them as described in the AWS D8.9M standard [24].

3.1.2 Cross tension

Cross tension tests were used to investigate the deformation behaviour of the welded joint in tensile loading. The test procedure shown in the AWS standard D8.9M [24] was followed when executing these tests. The coupon, shown in Figure 58, was removed from the quenched sheets via laser cutting and spot welded together.

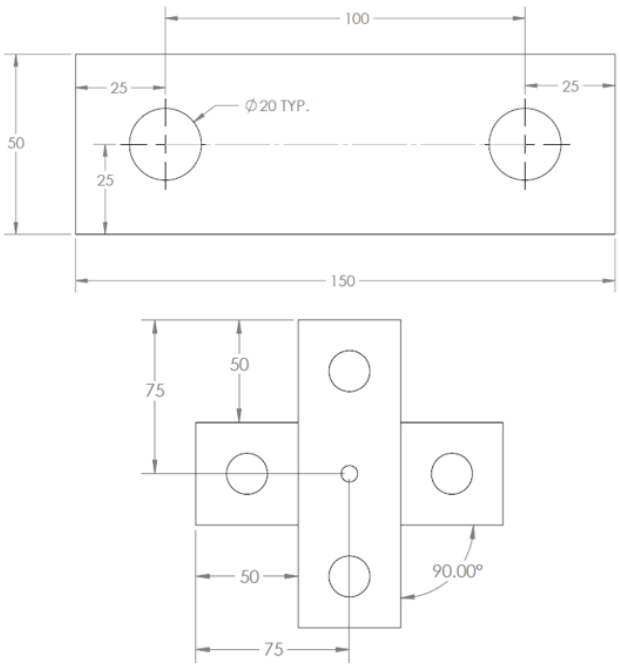

Figure 58: Cross tension specimen in millimeters

Similar to the lap shear tests, the 100 kN MTS test frame shown in Figure 41 was used to deform the specimens. The fixtures shown in Figure 59 were used to hold the specimens in the proper orientation within the MTS. During the test, the cross head of the MTS was set to move at a rate of 10 mm/min and the knurled grips exerted a pressure of 3000 psi on the fixtures when clamping.

Figure 59: Cross tension fixtures

The same data collection scheme discussed in section 3.1.1 was utilized during the cross tension experiments. Both the lap shear and cross tension tests can provide insight into deformation at the macroscopic level but since the failure mode was dominated by through-thickness shear concentrated at the weld notch, the critical strains were not visible. Consequently, these tests could not be used to directly measure the weld fracture strain.

3.1.3 Spot welded V-bend

The V-bend specimens were used to investigate the deformation behaviour of the HAZ in plane strain loading. The square specimens shown in Figure 60 were extracted from quenched sheets which were spot welded together with an offset so that the HAZ would be in the strained region.

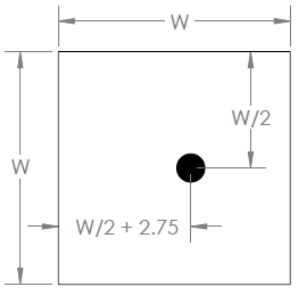

Thickness (T)	Width (W)
1.2	48
1.6	64

Figure 60: V-bend specimen in millimeters

To perform these tests, the apparatus shown in Figure 43 was used with a procedure similar to the VDA standard used for base metal testing. Initially, the spot weld specimen was placed such

that it lay flat across the supports and knife. Once the test initiated, the circular supports descended the specimen onto the knife edge at a rate of 20mm/min, inducing bending. To record force data during the experiment, a 70 kN load cell was placed between the hydraulic actuator driving the motion and the displacement was measured using an LVDT within the hydraulic actuator.

Random speckling was applied to the top surface of the specimen and DIC techniques were used with the cameras described in Section 2.2.1 and 35 mm lenses producing a resolution of 56 pixels/mm. For post processing of the images, a subset size of 55, step size of 3, and strain filter of 5 was used, resulting in a VSGL of 0.31 mm.

3.1.4 Tensile spot weld

The tensile spot weld specimen was used to investigate the in-plane deformation behaviour of the HAZ, similar to the work conducted in [45, 65]. To fabricate the coupon shown in Figure 61, the tensile geometry in section 2.2.1 was removed via laser cutting from quenched sheets and joined using the weld parameters in Section 2.4.

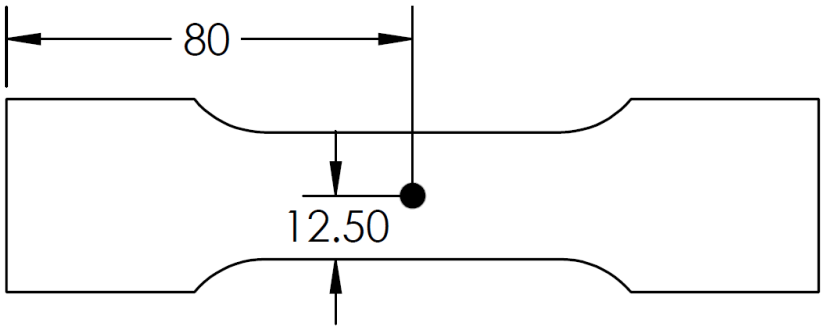

Figure 61: Spot welded tensile specimen in millimeters

The main benefit of this test was the opportunity to use DIC strain measurements in the welded region to determine how strain was distributed throughout the joint. To track strain on the surface of the specimens, a random speckle pattern was required. Initially, the specimen was media

blasted and sanded with 800 grit aluminum silicon sand paper to produce a surface roughness suitable for paint adhesion. At low strains, the Al-Si coating will flake-off and compromise the DIC speckle pattern and had to be removed. The specimens where then painted using the same procedure outlined in Section 2.2.1. To measure the evolution of the strain field, the cameras and software detailed in Section 2.2.1 were used. For post processing a subset of 29, step of 1, and strain filter of 7 were used to obtain a VSGL of 0.5 mm. To obtain force and displacement data, the scheme described in Section 3.1.1 was used. For the 1.6 mm specimens, the peak load was above the capacity of the system shown in Figure 41 and therefore a higher capacity machine was required. To address this, the MTS Criterion 64 shown in Figure 62 was used. For these tests, only force and displacement data was recorded due to the drive system interfering with the line of sight of the cameras.

Figure 62: MTS Criterion 64

3.2 Weld group experiments

The coupon level tests described in the previous section are useful for characterizing an individual weld under different loading conditions; however, in real structural joints, spot welds are never used in isolation and groups of welds are used to transmit structural loads. To numerically predict the mechanical response of these structures in a crash event, the progressive failure of spot weld groups must be characterized. In this work, an experiment was developed which examined the Mode I unzipping behaviour of spot weld groups. The intention was to characterize how spot welds progressively failed in tension as a result of two components separating. To fabricate the specimen for this work, the hat channels described in section 2.3 were laser cut and spot welded using the procedures in Section 2.4 as per Figure 63.

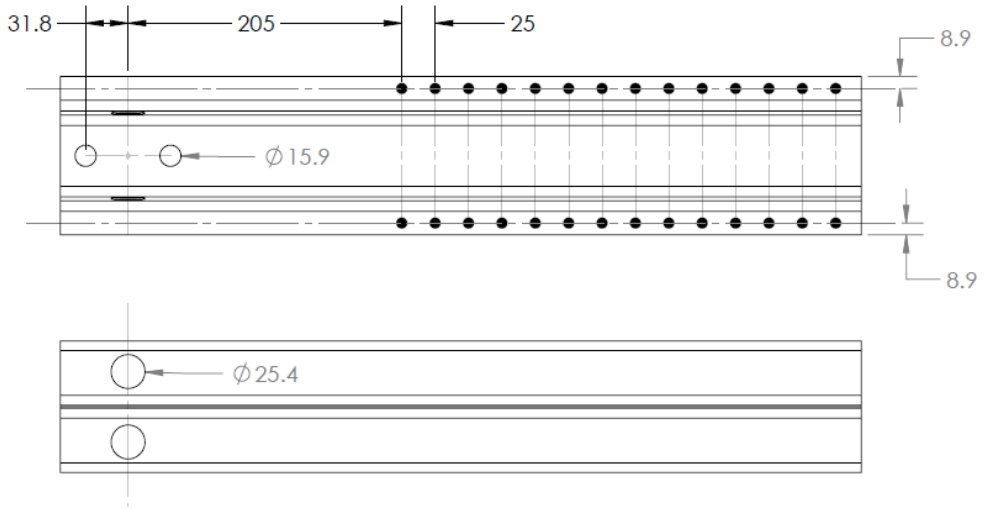

Figure 63: Mode I structural specimen in millimeters

3.2.1 Mode I quasi-static

To induce Mode I quasi-static loading of the weld group, a test configuration, dubbed the "Caiman", was developed to investigate the structural performance of the joining method. The fixtures

and boundary conditions implemented in this test are shown in Figure 64. The tooling consisted of bosses that clamped the specimen and a clevis that displaced the inner clamp via the dashed 19.05 mm diameter pins. The bottom clevis was clamped in the grips of the tensile machine shown in Figure 41 with a pressure of 3000 psi and the top clevis threaded into the crosshead load cell that was displaced upwards at a rate of 50 mm/min producing the deformation shown in Figure 65. During testing it was discovered that as weld failure propagated towards the end of the weld line, the displacement between weld failures increased significantly. Due to this, the specimens were only pulled to 250 mm of maximum displacement to reduce experimental run time.

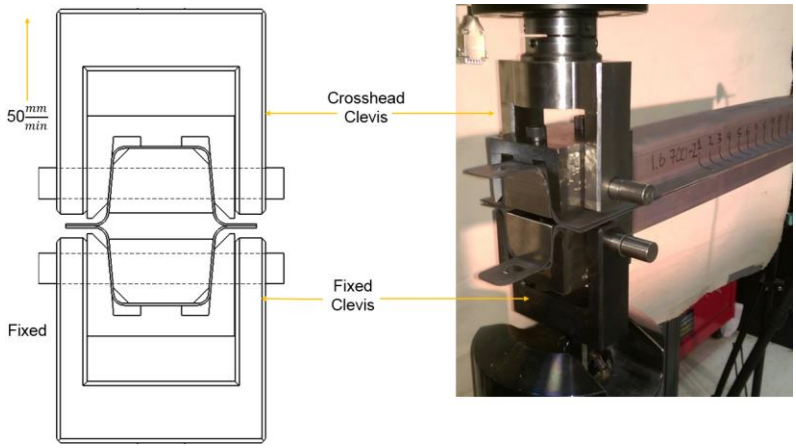

Figure 64: Mode I quasi-static fixturing and boundary conditions

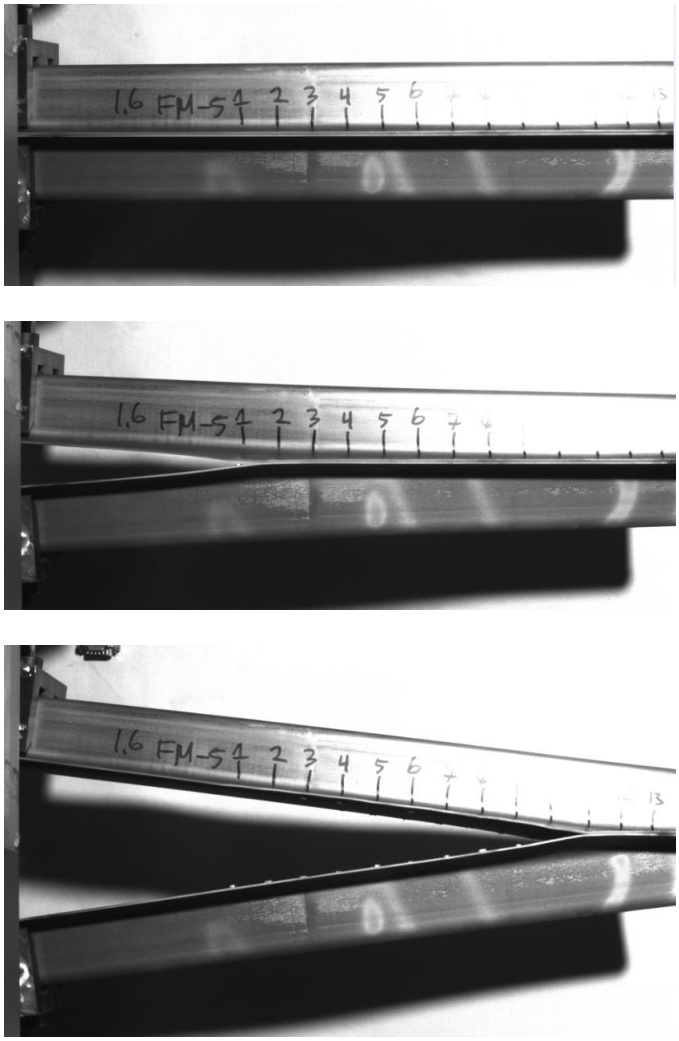

Figure 65: Start (top, first weld failure (center), and end (bottom) side images of Mode I quasi-static test

As a proof of concept, 1.2 mm fully quenched and 400°C tailored flange specimens were tested using the apparatus shown in Figure 66. In these experiments strain field measurements were taken using DIC, similar to the approach mentioned in sections 3.1.3 and 3.1.4. To apply a random speckle pattern to the first spot weld, the same surface preparation described in section 3.1.3 was used. When the specimen was clamped within the fixtures, the cameras and lenses described in section 2.2.1 were used to capture images at 10 Hz with a resolution of 34.4 pixels/mm up until the first weld completely failed. For post processing, a subset size of 95, step size of 3, and strain filter of 5 was used resulting in a VSGL of 0.44 mm. From the side, a macro view was obtained with a Point Grey Research GRAS-

50S5M-C 5.0 MP camera at a frequency of 4 Hz. VIC SNAP 2009 was used to capture the images so that force and displacement data could be synchronized to the visual data.

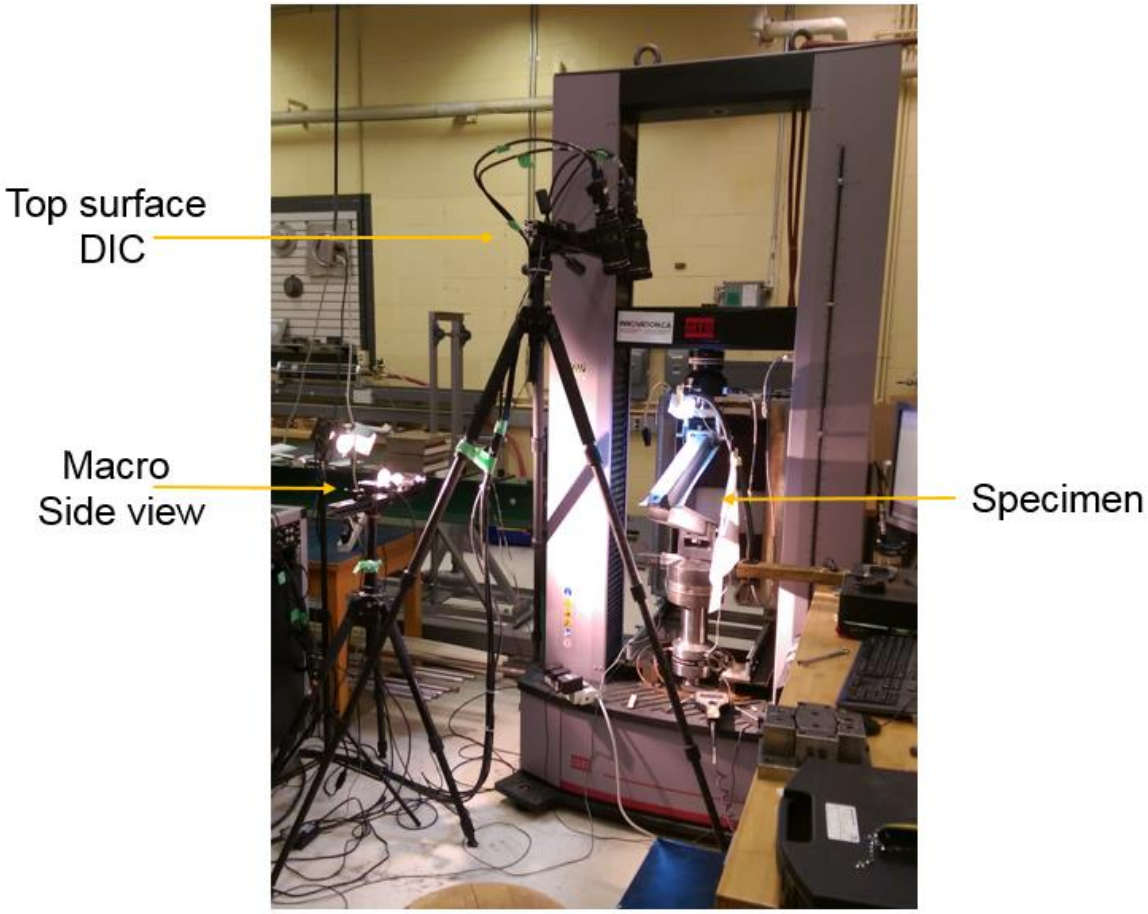

Figure 66: Proof of concept Mode I quasi-static camera set up

Next, 1.6 mm fully quenched, 400°C and 700°C tailored flange specimens were tested and the set-up was modified as shown in Figure 67. From the proof-of-concept tests it was observed that there was minimal surface strain due to the stress intensity at the notch within the weld which is discussed further in Chapter 6. Therefore, for the 1.6 mm material the set up differed from the original set up in that the DIC system was removed and replaced with thermal imaging. The thermal camera used in this work was the Telops Fast-IR-2K and the HypeIR software was used to perform the data

collection and post-processing. During the experiments the camera was set to trigger once the load reached approximately 700 N afterwards images were taken at 4 Hz until the end of the test.

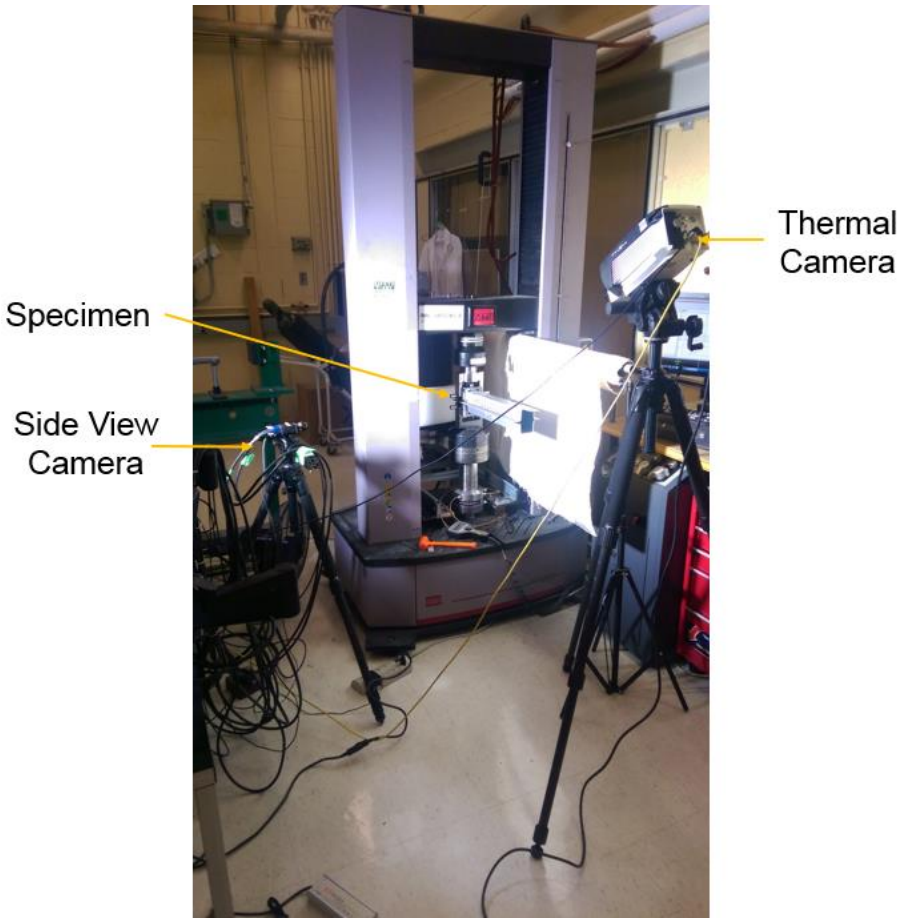

Figure 67: Mode I quasi-static set-up

Attempts were also made to utilize piezo-electric acoustic emission sensors to detect acoustic events associated with weld failure. Unfortunately, a high sample rate was required to capture the acoustic event, whereas a long duration was required to record the entire test duration; as a result, the amount of data gathered during each test was too large and exceeded the storage capacity of the available AE system. Consequently, this measurement method was abandoned and left for future work. Regardless, the thermal imagery proved adequate to track weld failure propagation within the spot weld group.

3.2.2 Mode I dynamic

The ultimate goal of this work was to improve the manner in which spot welds are modelled in crash simulations. While the quasi-static Caiman was sufficient for comparing the structural response of spot welds to that seen in the single weld testing described in section 3.1, crash events are not quasi-static. To induce dynamic Mode I loading on the specimens shown in Figure 63, the apparatus shown in Figure 68 was used. The idea was to replicate the deformation produced statically so that comparisons could be made between the dynamic and quasi-static versions. Since the way in which the boundary conditions are applied to the deforming pin are fundamentally different in the quasi-static and dynamic tests, different set-ups were required.

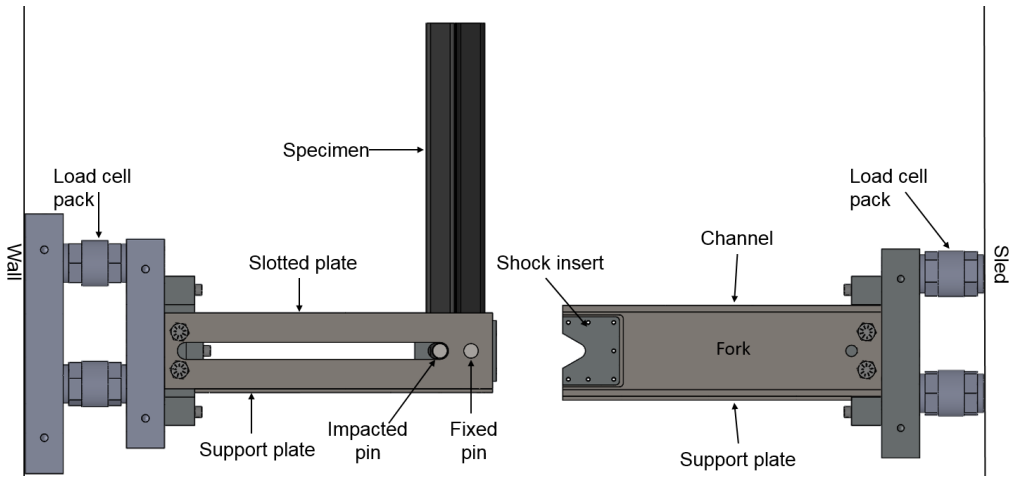

Figure 68: Mode I dynamic apparatus CAD please add arrow showing the sled movement

The dynamic set-up used the same boss system that the quasi-static test used to clamp the specimen but instead of the clevises, two sub-assemblies enforced displacement boundary conditions. To conduct the dynamic testing, the sled at the University of Waterloo was used. The fork was mounted to the sled and it consisted of 2 channels that were reinforced by a plate on the bottom and had shock inserts bolted in that impacted the free pin on the wall assembly. The boss-specimen assembly was held in position by two pins that contacted the inner bosses of the assembly. These pins

were held in place by two plates that were mounted to the wall and had a hole and a slot machined into them. The hole farthest from the wall was used to hold the specimen in place during the test and the slot was intended to allow free motion of the impacted pin. During the experiment, the shock insert impacted the pin closer to the wall at a speed of 7.4 m/s producing roughly the same deformation mode as the quasi-static testing shown by Figure 69. Pins were used to enforce displacement in the system because the bosses needed to rotate as deformation occurred.

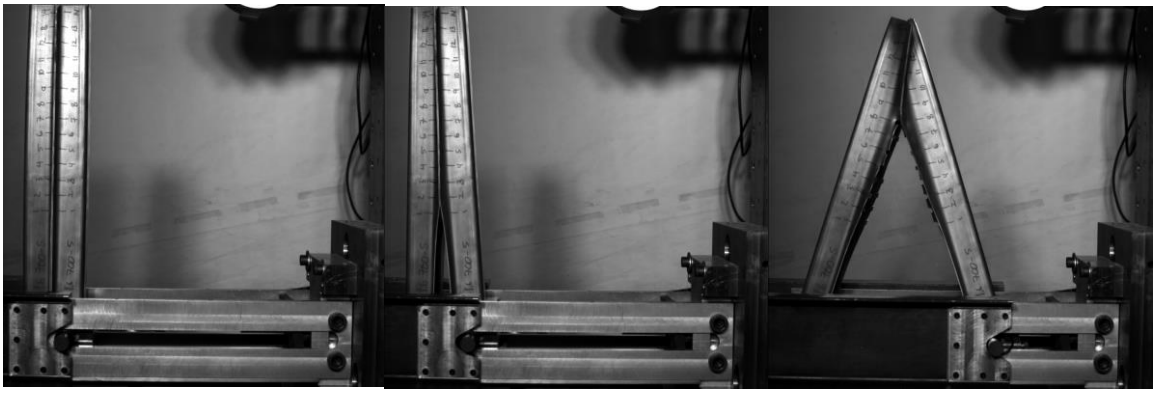

Figure 69: Start (left), first weld failure (center), and end (right) side images of Mode I dynamic test

Plascore 5052 honeycomb with a nominal crush strength of 3.69 MPa (535 psi) [66] was mounted on both sides of the specimen assembly to stop the sled after the majority of the test distance was reached. The crush distance for all dynamic tests was 250 mm. Two 150 mm x 150 mm blocks of honeycomb with a length of 200 mm were mounted 185 mm above the base of the sled; one on each side of the crush specimen. Once contacted, the honeycomb served to bring the sled to a complete stop prior to the fork assembly contacting the rigid wall, thereby preventing damage to the equipment.

The fork and wall assemblies were mounted using three 120 kN load cells and 2 mounting plates. The total force applied by the sled onto the parts was equal to the sum of the forces measured by the cells within each pack. The load cells were placed in a triangular pattern at a spacing of 233 mm. The sampling rate used to acquire the load cell data was 10,000 Hz. The crash sled incorporates

two accelerometers with one mounted on each side. The accelerometers measure the deceleration experienced by the sled during crash. The sampling rate for these accelerometers was the same as the piezoelectric load cells (10,000 Hz). The displacement of the sled was calculated by integrating the deceleration data obtained from the accelerometers.

The dynamic experiment was recorded using three high-speed Photron SA4/5 digital cameras, with a frame rate of 5,000 Hz. The first of these cameras was mounted to the side of the specimen, the second was mounted such that it provided an isometric view, and the third was mounted above. The thermal camera used in quasi-static testing was also utilized in this experiment at a capture rate of 5,000 Hz. The assembled apparatus with all cameras and lighting used in testing is shown in Figure 70 with still images from each high speed camera shown in Figure 71. The two data acquisition systems (the piezoelectric load cells and the accelerometers) as well as the cameras were activated by a laser trigger that was located on the rails of the sled. During a dynamic crush test, once the sled crossed the trigger, the data acquisition was turned on for two seconds that was sufficient to capture the impact.

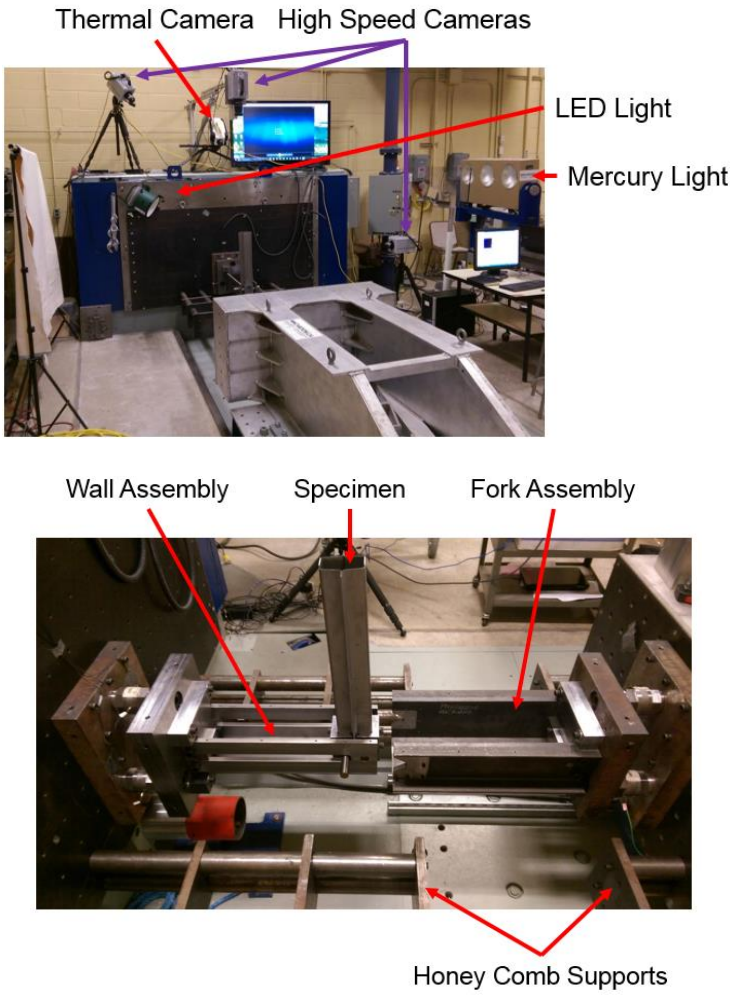

Figure 70: Mode I dynamic experimental set up

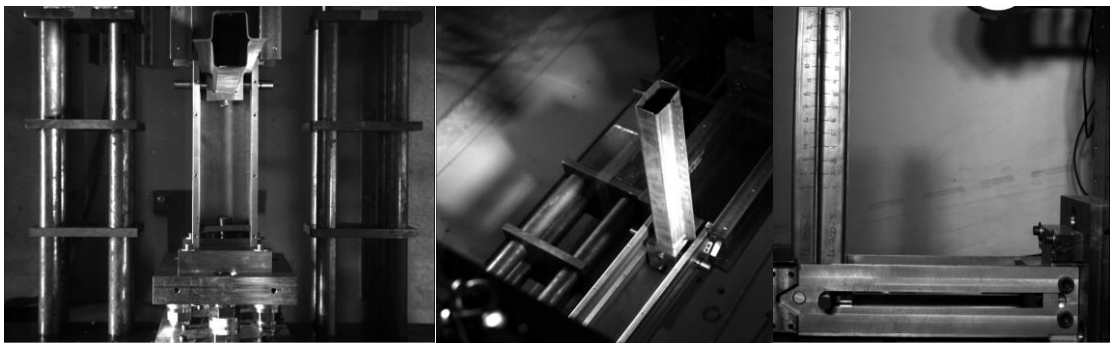

Figure 71: Still images of Mode I dynamic set up from top (left), isometric (center), and side (right) views

4.0 Mechanical performance data for Single Spot Welds

4.1 Cross tension

To assess the tensile response of single spot welds, cross-tension experiments were performed. In Figure 72, the force-displacement measurements taken from the cross-tension experiments on single weld coupons for all material conditions are shown. Overall, the peak load levels were similar for all quench conditions of like thickness with the more ductile materials experiencing more deformation before fracture and during the fracture event. As the thickness of the material increased, so did the resistance to bending, resulting more Mode I opening at the edge of the weld with more bending. The quench condition affected the amount of displacement sustained before fracture. For the fully quenched material, softening was seen around the nugget whereas for the tailored materials, little to no softening was observed. There were two distinct post fracture behaviours which emerged from the data. The first corresponded to a sudden drop after the peak load corresponding to the left image in Figure 73 and Figure 74, in which the weld pulled completely out of the coupon after reaching the peak load. The second mode corresponds to a plateau in force that was observed after the peak load; this mode corresponded to the "double fracture" shown on the right side of Figure 73 the majority of the weld pulled out of one coupon, after which it continued to transmit load prior to completely pulling out of the opposite coupon. The critical measurements extracted from the data are summarized in Table 3. Reviewing the data, a large variation was observed in these tests, in particular for in the 400°C tailored material. Several factors could contribute to this, such as weld position relative to the centre, coupon alignment, fixture alignment, and clamping force. The fixtures shown in Figure

59 used to execute these tests were difficult to control such that the same clamping conditions could be reproduced for every test.

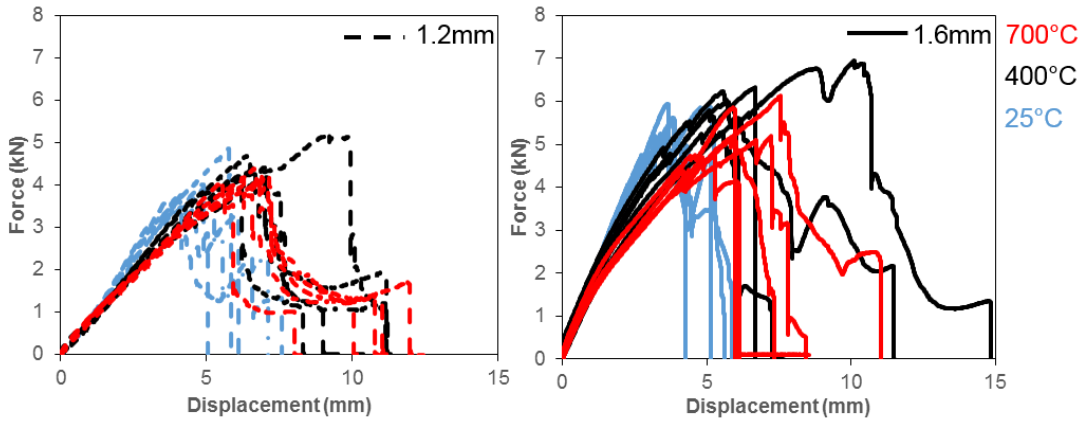

Figure 72: Force displacement measurements taken from all cross tension tests

Figure 73: Cross tension single (left) and double (right) fracture images

Full Quench		400°C die quench		700°C die quench	
Single pullout	Double pullout	Single pullout	Double pullout	Interfacial	Double pullout
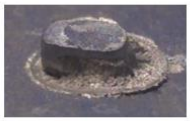	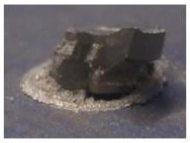	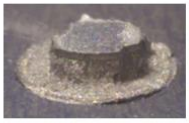		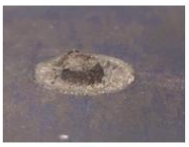	

Figure 74: Cross tension failure surfaces

Table 5: Average and standard deviation for critical measurements from cross tension testing

Material	Peak Force (kN)	Displacement (mm)	Absorbed Energy (J)	Nugget (mm)
1.2 FQ	4.0±0.4	4.8±0.7	13.7±1.7	5.3±0.3
1.2 400	4.5±0.4	7.2±1.0	24.3±5.4	5.4±0.3
1.2 700	4.1±0.1	6.4±0.5	21.7±3.6	5.3±0.5
1.6 FQ	5.5±0.3	3.9±0.5	17.4±2.0	5.3±0.4
1.6 400	6.3±0.4	6.6±1.7	34.7±12.3	6.2±1.1
1.6 700	5.4±0.5	6.4±0.8	25.4±6.0	4.5±0.7

On a structural level, it is important to characterize the amount of energy a welded joint absorbs through deformation. To that end, the measurements shown in Figure 72 were integrated over the force-displacement history and energy as a function of displacement is shown in Figure 75. While thickness slightly increased the amount of energy the joint absorbed over the experimental event, parent metal strength largely controlled the response. In the fully quenched material, the HAZ had a lower yield strength so deformation quickly localized in the HAZ and resulted in rapid weld failure. The parent metal strength in the fully quenched material is high and that limits parent metal deformation such that overall energy dissipation is low. For the tailored specimens, more deformation occurred in the parent metal allowing the joint to absorb more energy. The large variation in total energy absorbed in the experiment is mainly due to how fracture initiated and propagated in the

specimen. In the fully quenched specimens, the failure mode was consistently double pull out for the 1.2 mm material in that the specimen experienced a drawn out fracture process but since the parent metal absorbed little to no strain energy, the work done throughout the test was relatively consistent as shown by Figure 75. For the 1.6 mm fully quenched material, single pull out was observed causing the specimens to completely fail at lower displacements than the 1.2 mm coupons. In the tailored materials, two different fracture modes were observed as shown in Figure 73 and Figure 74. In the specimens which experienced fracture in both coupons, the amount of energy absorbed was significantly higher than those specimens that only fractured in a single weld coupon.

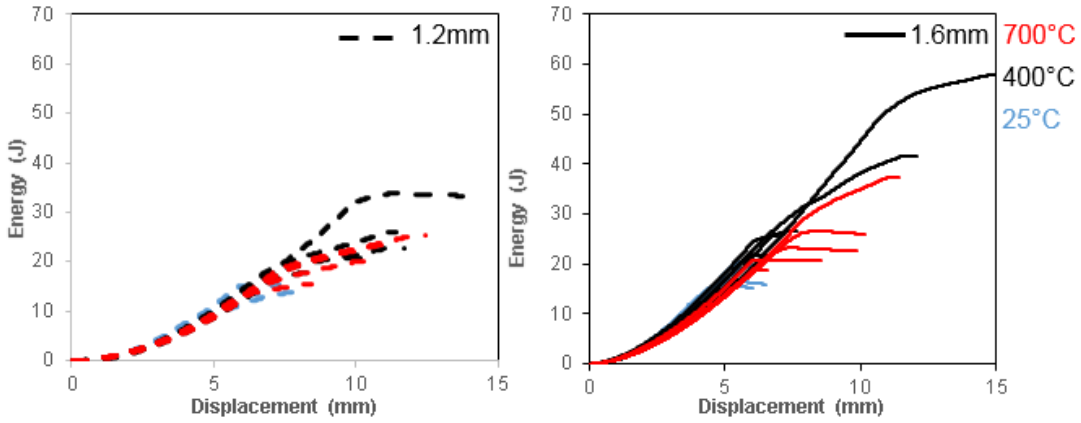

Figure 75: Absorbed energy versus displacement for all cross tension tests

4.2 Lap shear results

In order to characterize the shear strength of the joint, lap shear specimens were tested. The measured force displacement results are shown in Figure 76. Overall, the peak load increased with base metal strength and the amount of displacement observed at fracture initiation and during the fracture event increased with ductility. By decreasing the material thickness, the surface area of the nugget-HAZ interface shrinks, the amount of bending in the sample is higher, and there is a larger

Mode I load at the edge of the weld reducing the amount of strain energy picked up by the material and lowering the load bearing capacity of the joint. Parent metal ductility also affected the response of the welded joint; in the fully quenched materials, little to no yielding was observed whereas the 400°C and 700°C die quenched specimens exhibited more deformation before fracture. This is highlighted by the amount of rotation seen in Figure 77 and the failure surfaces in Figure 78. In terms of the fracture event, when stable nugget pull out occurred like in the thicker heated die materials, the force response was consistent but when fracture propagated all the way around the weld as seen in the fully quenched specimens, the peak load and displacement saw larger variation. After the test, the nugget was measured with a set of analog calipers and the diameter along with other critical measurements is shown in Table 6. It was observed that the thinner material consistently had a smaller nugget. This likely occurred because there was less heat used to bond the thin metals compared to their thicker counterparts. Contrary to the cross-tension results, a larger variation was measured in the lap shear nuggets because in the pullout fractures shown in Figure 78, a small amount of material remained attached to the nugget after it pulled out.

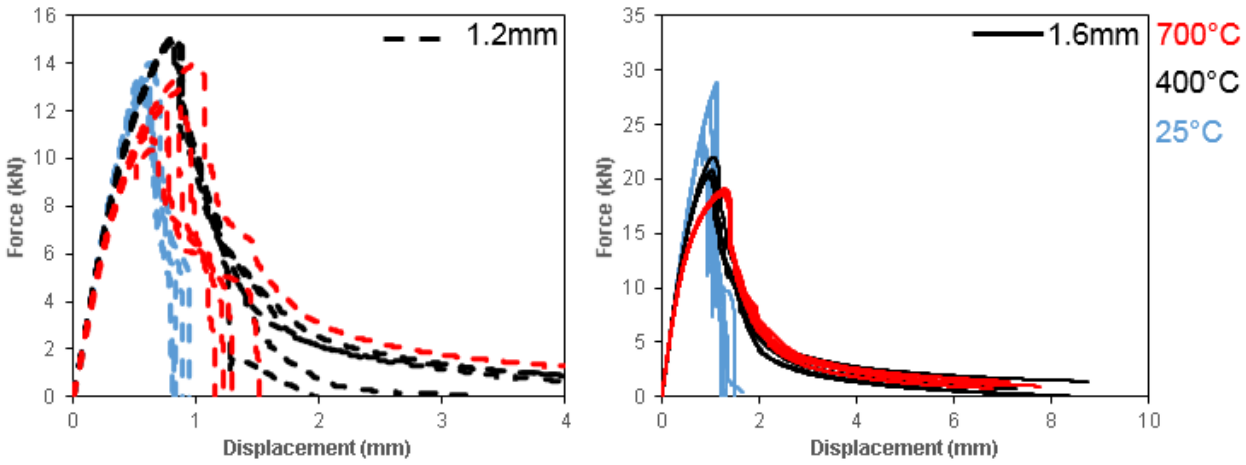

Figure 76: Force and displacement measurements gathered during lap shear testing

Table 6: Average and standard deviation for critical measurements from lap shear testing

Material	Peak Force (kN)	Displacement (mm)	Absorbed Energy (J)	Nugget (mm)
1.2 FQ	13.2±0.5	0.6±0.03	6.8±0.5	5.4±0.2
1.2 400	15.0±0.1	0.82±0.01	16.7±3.0	7.5±0.8
1.2 700	12.1±1.3	0.78±0.14	12.2±6.0	6.0±1.3
1.6 FQ	26.5±2.1	0.98±0.13	19.0±2.7	6.1±0.2
1.6 400	20.8±0.6	1.00±0.04	34.6±4.5	8.7±0.1
1.6 700	18.8±0.2	1.28±0.02	36.9±1.6	8.8±0.2

In the ductile materials where the HAZ was harder than the base metal, the strain was distributed throughout the base metal with the largest concentration being at edge of the weld. Small strains were measured on the surface of the specimen because there is a large amount of out-of-plane bending and through thickness shear placing the critical strains at the weld notch which is not visible as discussed in Section 1.3.2.

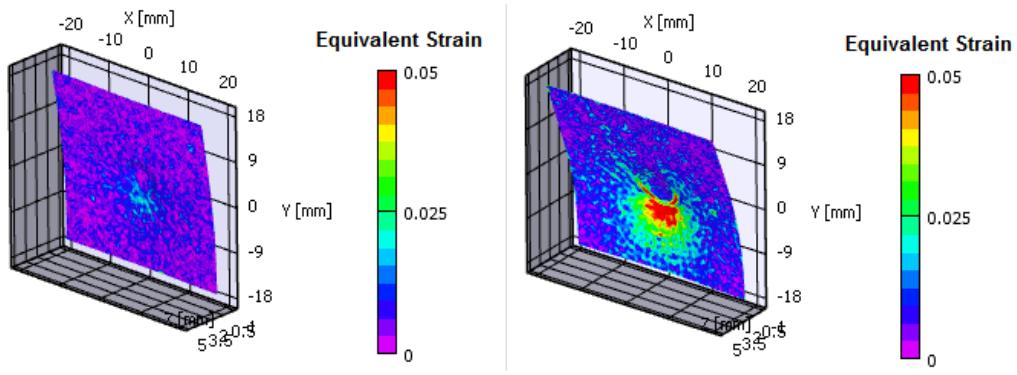

Figure 77: Strain fields measured on fully quenched and 700°C die quenched lap shear specimens during testing

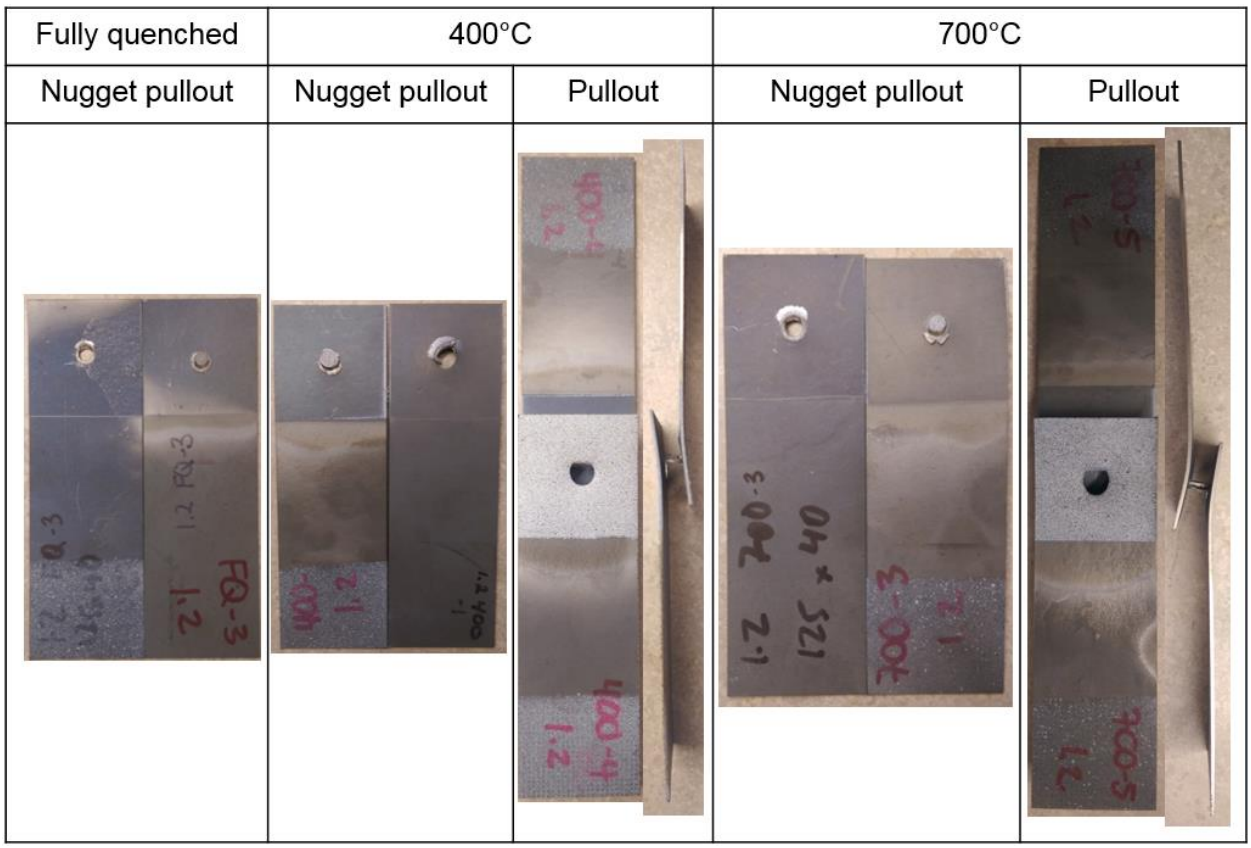

Figure 78: Lap shear specimen failure modes

Using the data shown in Figure 76, the absorbed energy was calculated by integrating the force *versus* displacement. Energy was then plotted *versus* displacement as shown in Figure 79. For the 1.6 mm material, there is little difference between the 400°C and 700°C tailored materials. When weld failure occurred by inducing fracture in the parent metal, the strength of the parent metal seemed to have little influence on the amount of energy absorbed by the joint. Comparing the 1.2 mm and 1.6 mm samples, the thickness was observed to affect the strength of the specimen. While the mechanical response of the fully quenched and 400°C scaled with thickness, the 700°C tailored material experienced a change in the spot weld fracture mechanism. This can be explained by the size of the welded region, the volume around the weld in the thinner material is smaller and therefore, plastic strain energy density is higher, increasing strain concentration in the material close to the nugget. This

gave the material less area to dissipate plastic energy over and causing fracture to propagate around the weld at lower displacement values.

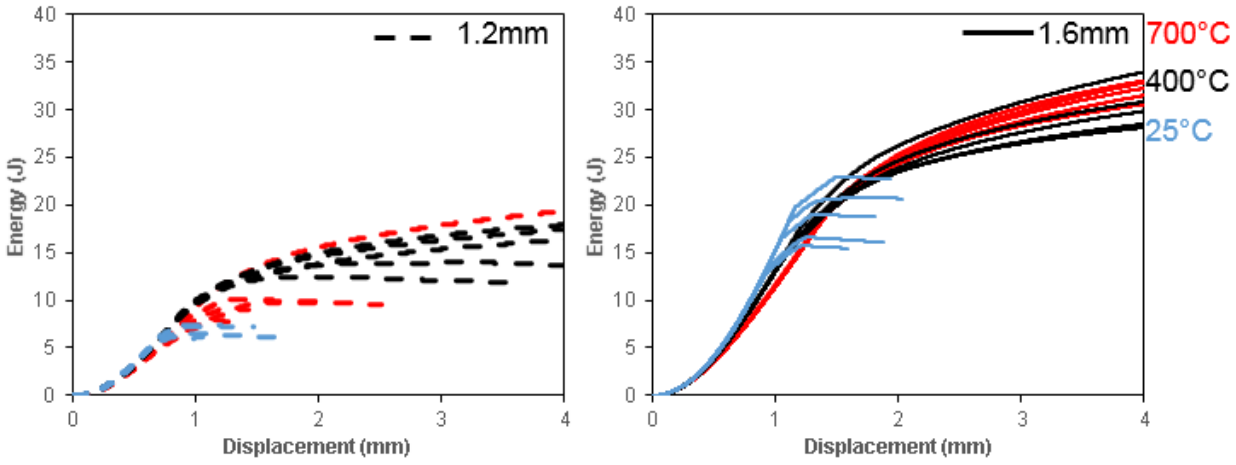

Figure 79: Energy plotted over displacement for all lap shear tests

4.3 Spot welded V-bend results

While the lap shear and cross tension tests are useful to determine the maximum force and energy which the joint could endure in tensile and shear loading, they were not useful for extracting local fracture strains. To that end, spot welded V-bend specimens were tested so that the strain distribution across the nugget-HAZ-parent metal zones could be examined. In Figure 80, the force-displacement measurements are presented. Reviewing the force measurements, the thickness and quench condition both distinctly influenced the failure process. When looking at the different quench conditions, the fully quenched material is the strongest and least ductile, whereas the 400°C and 700°C die quenched materials show similar strength and ductility. Also, for both of these material conditions even after fracture initiated, the force continued to increase. In the thicker specimens, the forces were larger and the variation between displacement at peak load and weld release for the quenched materials was amplified. Similar to the base metal data shown in Figure 44, the 700°C die quenched material

exhibited more hardening in the 1.6 mm condition causing it to be stronger and more ductile than the 400°C metal. While force measurements were useful to identify trends in the material strength, the true value of this test was in the strain measurements

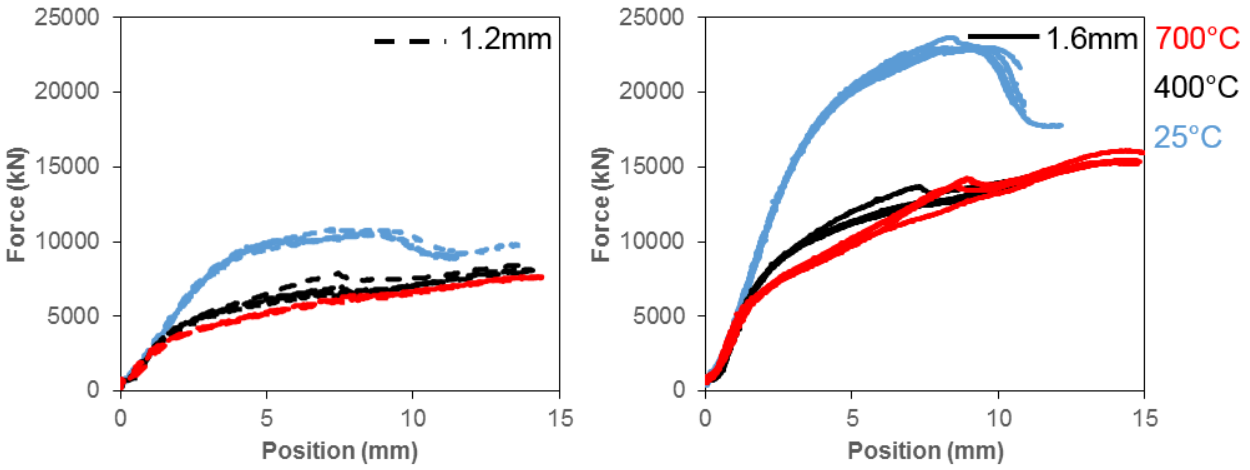

Figure 80: Force displacement measurements gathered during V-bend testing

To process the strain field data sampled over the test event, true strain data was extracted at the point where fracture initiated. The strain paths and equivalent strains at fracture shown in Figure 81 were extracted with VIC-3D. In the fully quenched and 400°C die quenched material, the strain localized on the nugget-HAZ interface where softening occurred causing fracture to initiate early in the deformation process. Although a crack formed in the HAZ, the load continued to increase because the surrounding parent metal continued to take up load as the rollers displaced. For the 700°C material, as was shown in the lap shear specimens, a different failure mode was seen in the 1.2 mm and 1.6 mm specimens. In the thinner materials, the strength gradient in the welded region caused strain to localize at the lowest hardness location adjacent to the weld but in the thicker material, a larger amount of material was available to absorb strain energy and fracture initiated in the parent metal. Contrary to previous testing methods, this procedure resulted in strain levels much higher than

those seen in lap shear. This high strain occurred because the weld notch was placed close to the initial location of neutral axis of the bend suppressing its effect on the joint.

In Table 7, outside of the 1.2 mm 700°C die quenched material, all welds exhibited similar failure strains and bend angles when a crack formed. For the 1.2 mm 700°C material strain localized in the parent metal with the weld acting as a stiffener significantly improving the performance of the specimen. Otherwise strain localized in the HAZ suggesting that the strength gradient around the weld caused strain to localize and fracture to initiate at a major strain of approximately 0.20 strain in the HAZ. Since these strains were much lower than that observed in the parent metal (0.3 for fully hardened at 0.5 for tailored material) it is clear that strain energy localizes in the softened region surrounding the weld during deformation inducing fracture early due to the high strain energy density in the HAZ.

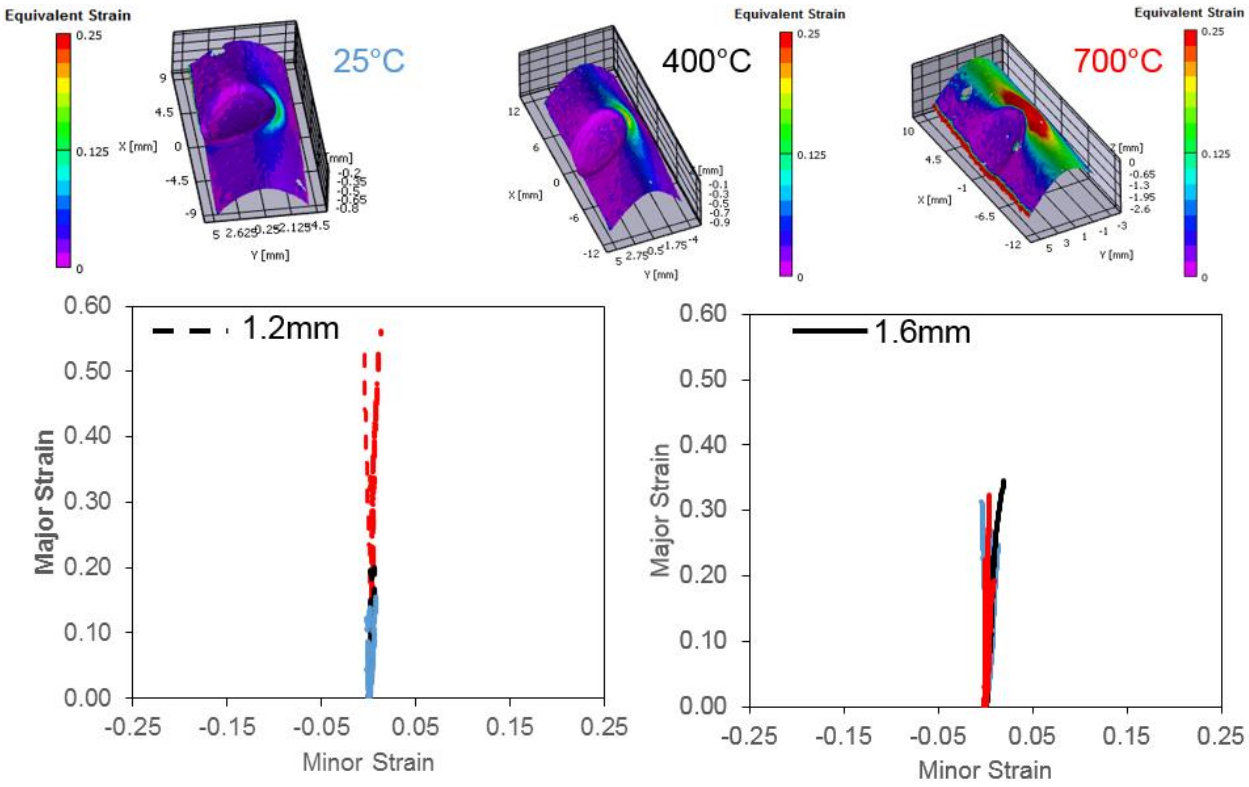

Figure 81: Contour plots (top) of equivalent strain one frame before fracture for V-bend tests (25°C left, 400°C center, 700°C right) and strain paths at critical point until crack initiation (bottom)

Table 7: Average and standard deviation for critical measurements from V-bend testing at the VDA load threshold

Material	Peak Force (kN)	Displacement (mm)	Fracture Strain	VDA Bend Angle
1.2 FQ	10.6±0.2	3.8±0.5	0.14±0.01	27±4
1.2 400	8.0±0.3	3.8±0.3	0.18±0.02	27±3
1.2 700	7.6±0.1	7.8±1.6	0.48±0.09	61±11
1.6 FQ	23.1±0.2	4.8±0.1	0.25±0.03	33±1
1.6 400	14.1±0.2	3.9±0.7	0.20±0.08	27±4
1.6 700	15.8±0.3	5.4±0.6	0.22±0.05	38±4

4.4 Spot welded tensile tests

Similar to the V-bend specimens, spot weld tensile specimens were used to provide insight into how the strain field is distributed across a spot welded joint. In Figure 82, the force-displacement measurements taken during the test are presented. As can be seen in the force-displacement curves, the presence of the weld had little influence on the response of the specimen. Since the 1.6 mm specimens reached loads higher than 100 kN, a larger system was required and due to physical constraints of the apparatus, only force-displacement data was extracted from these experiments. While the fully quenched material was able to support small strain values in the JIS specimens, the welded samples show significantly less ductility. This can be explained by examining the measured strain fields.

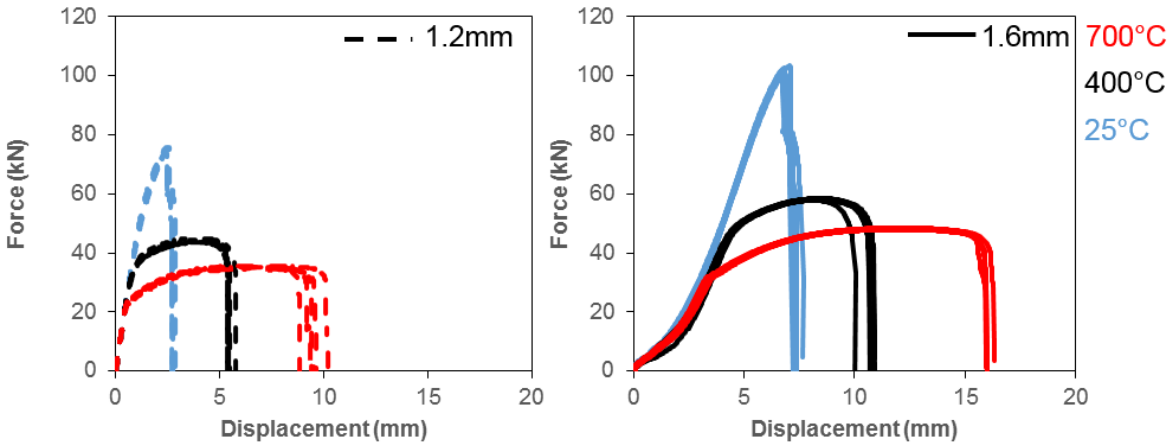

Figure 82: Force displacement measurements gathered during spot welded tensile testing

From the strain field data, true strain was calculated over the entire gauge length resulting in the equivalent contour plots shown in Figure 83. There was a clear localization around the weld in the fully quenched material where normal shear bands occurred in the heated die material conditions. These results served to validate the behaviour discussed in the previous sections, since strain clearly

localized in the softened HAZ of the fully quenched specimens but in the tailored specimens because there was no significantly softening around the weld causing fracture to occur in the base metal.

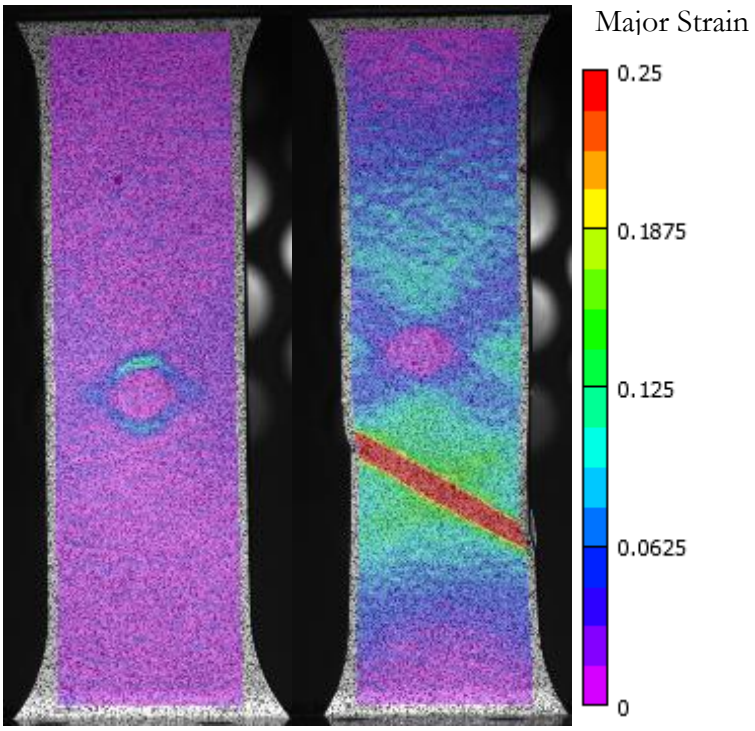

Figure 83: Equivalent strain contour plots one frame before fracture for spot welded tensile tests of fully quenched (left), and 400°C (right) specimens

4.5 Summary of Single Weld Experimental Data

The single weld testing shown in this chapter illustrated how the ability of the base metal to dissipate plastic work influenced the performance of the joint. In normal (Mode I) loading, all welds showed similar strengths with the more ductile metals seeing more displacement before fracture. The resulting fracture surface showed nugget pull out consistently with a shorter onset of cracking in the thicker sheet. When loaded in shear, the effect of tailoring was observed with the ductile quench conditions experiencing rotation and the fully hardened material showing little. The fully hardened material saw nugget pullout with fracture contained within the welded region. For the ductile quench conditions, nugget pull out was observed with fracture transition from the welded region to the base metal. The V-bend experiments showed how strain distributed in the joint and how this impacted fracture. The fully hardened and 400°C quenched material saw strain localize in the HAZ which caused rapid fracture initiation and propagation at equivalent strains. 700°C quenched material showed a more even distribution and higher strain at failure. The single weld work was then concluded by the JIS testing which showed that strain localization and failure occurred in the weld for the hardened material whereas the tailored grades showed strain localization and fracture occurring within the base material.

5.0 Numerical characterization of single weld deformation and failure

In this chapter, a numerical model of resistance spot weld (RSW) failure is presented and compared to the data sampled during the single resistance spot weld experiments described in Chapter 4. The objective of this model was to provide predictions of RSW failure that are compatible for use within current industrial computer aided engineering (CAE) of a full vehicle crash response. With this in mind, the model is not cast at a meso- or micro-scale, but rather adopts a macro-scale treatment using shell-based finite element formulations. For this model the technique described by Seegar [67] was used and the material properties were iteratively determined by comparing predictions of cross tension and lap shear simulations to experimental data. For all numerical work presented here, LS-DYNA MPP R7.0.0 [68] was used.

When modelling spot welds on a structural level, computational efficiency is of vital importance so the schemes used to define spot weld deformation and rupture are only intended to describe the macroscopic performance of the joint. In these simulations, deformation and fracture of the Usibor® 1500-AS parent metal, in the various tailored conditions, was modelled using the hardness dependent mapping technique described by Omer [14]. The weld was characterized using linear hardening and a stress-based failure criterion, with a so-called "fade energy" parameter used to control post-failure response after failure initiation. The material model used to define the spot weld in LS-DYNA is discussed in this Section 5.1.2. Calibration of the model was performed for the three material (quench) conditions and sheet thicknesses considered in the weld characterization studies presented in the previous chapter. The cross tension results were used to calibrate the normal strength

of the weld, while the lap shear data was utilized to characterize the yield strength, linear hardening rate, shear strength, and fade energy of the joint.

5.1 Base material and spot weld modeling technique

This section contains a description of the meshing strategy and material models used for the parent metal and spot weld. While the method of modelling the parent metal is not developed as part of this study, a quick review serves to strengthen the discussion herein. In the weld model, the yield strength, hardening modulus, weld size, normal strength, shear strength, and fade energy were investigated and the effects of each variable are examined in a parametric fashion at the end of this chapter.

5.1.1 Mesh distribution within spot weld region

Although the overall mesh distribution changed between the lap shear and cross tension simulations, an approximation of the mesh shown in Figure 84 was used in all numerical models in this chapter. The parent metal was defined using fully integrated shell elements with 7 through thickness integration points. The weld was defined by a beam element that is automatically converted by LS-DYNA into a cluster of 8 hexahedron solid elements when the simulation initialized. In the cross tension simulation, 3.1 mm shell elements were used, while in the lap shear simulation 2.8 mm elements were applied.

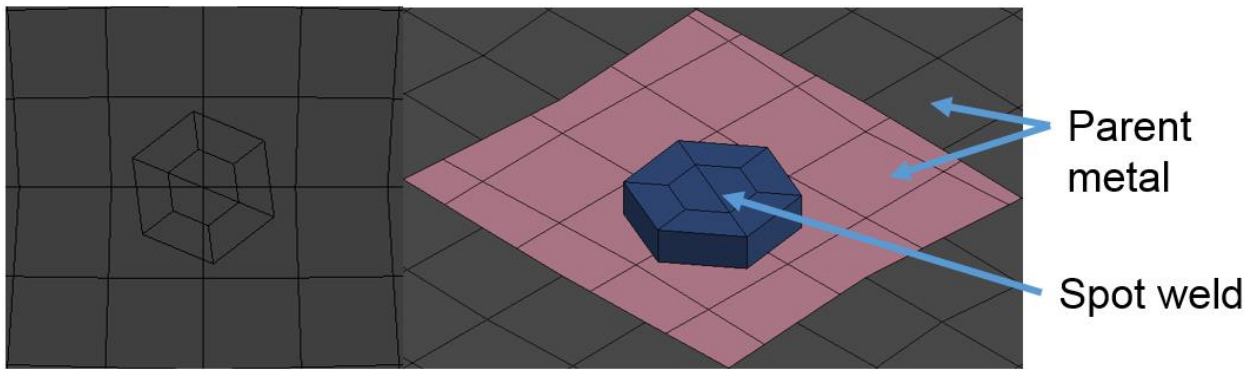

Figure 84: Welded region mesh distribution

5.1.2 Parent Material Model Properties

The parent metal constitutive and fracture behaviour makes use of extensive efforts by the Forming and Impact Group to characterize USIBOR® 1500 [11, 3, 13, 17, 14, 7]. The yielding behaviour was modelled using the von Mises yield criterion and the hardening curves shown in Figure 85 which were made strain rate dependent by adopting the phenomenological relations proposed by Bardelcik and Omer [11, 14]. A set of flow stress curves was defined for each base metal hardness as shown in Section 4.2.1. Fracture of the parent metal was modeled using the Generalized Incremental Stress State dependent damage Model (GISSMO) developed by Daimler and DYNAmore for the modeling of failure in ductile materials [12, 69]. This failure model utilizes a phenomenological approach to damage prediction in which damage is accumulated over a given strain increment based upon the ratio of plastic strain increment to the failure strain in proportional loading that varies as a function of stress state. The fracture locus under proportional loading, developed by ten Kortenaar [13] for each of the quench conditions considered in the current work, is taken as the primary input data to the GISSMO model with the damage exponent fixed at 2.

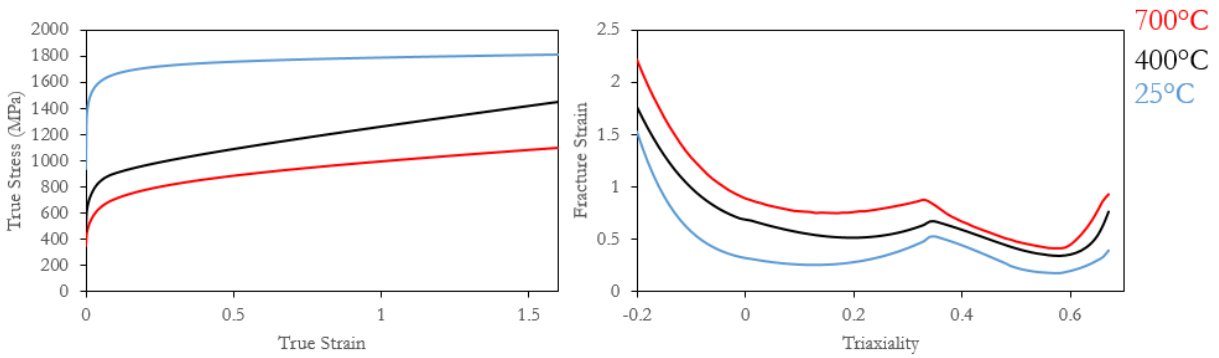

Figure 85: Flow stress curves and fracture loci of fully quenched (25°C), 400°C tailored (262 HV), and 700°C tailored (211 HV) USIBOR® 1500-AS used in numerical models

5.1.3 Spot Weld Material Model Properties

For the spot weld, an isotropic linear hardening model was used to define yielding and a stress dependent damage model was used to account for failure. The constitutive response of the spot weld elements was characterized using the flow stress curve shown in Figure 86. In this curve, after yield the material hardened at a linear rate specified by the user (E_h) until failure initiated after which the weld absorbed a defined amount of energy prior to complete failure to resemble the onset and progression of cracking.

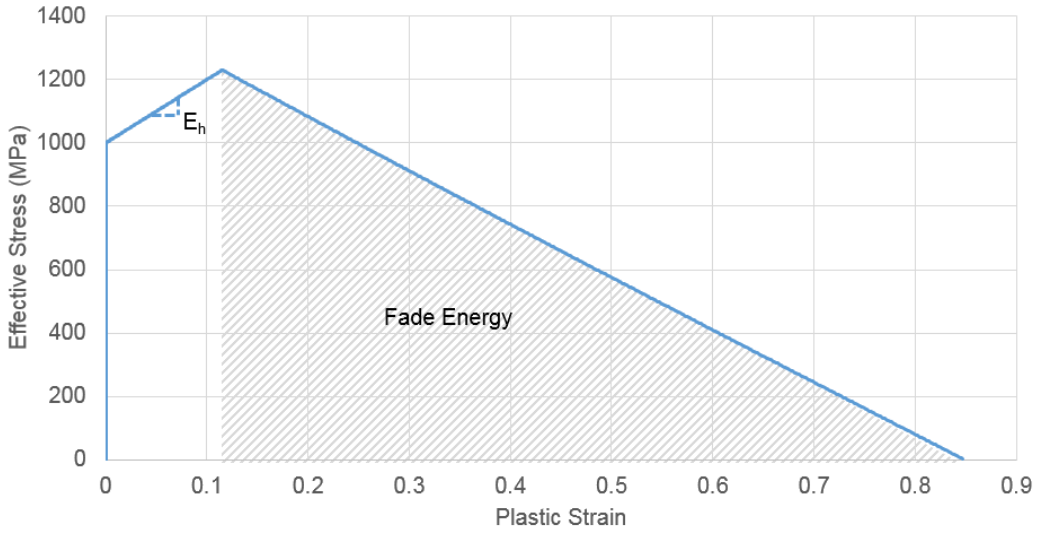

Figure 86: Sample numerical flow stress curve of spot weld from a lap shear simulation

The failure function used for this work is shown by Eq. (5) through Eq. (8). The failure function, Eq. (5), has 6 user-defined parameters, Normal Strength (σ_n^F), Bending Strength (σ_b^F), Shear Strength (τ^F), and the respective exponents (m_n, m_b, m_τ). The normal stress in the weld (σ_n) is calculated by dividing the normal force (N_{rr}) transmitting through the weld by the area (A) of the weld, as shown by Eq. (6). The bending resultant is determined by dividing the moments perpendicular to the weld $(M_{rs}\ and\ M_{rt})$ by the moment of inertia (Z) as shown in Eq. (7). The shear resultant (τ) calculated using Eq. (8) in which the moment parallel to the weld (M_{rr}) which is scaled by a user defined factor *SCLMRR* and the force resultants perpendicular to the weld $(N_{rs}\ and\ N_{rt})$ are divided by the area of the weld.

$$f = \left(\frac{\sigma_n}{\sigma_n^F}\right)^{m_n} + \left(\frac{\sigma_b}{\sigma_b^F}\right)^{m_b} + \left(\frac{\tau}{\tau^F}\right)^{m_\tau} - 1 \tag{5}$$

$$\sigma_n = \frac{N_{rr}}{A} \tag{6}$$

$$\sigma_b = \frac{\sqrt{M_{rs}^2 + M_{rt}^2}}{Z} \tag{7}$$

$$\tau = SCLMRR\ x \frac{M_{rr}}{2Z} + \frac{\sqrt{N_{rs}^2 + N_{rt}^2}}{A} \tag{8}$$

The energy absorbed by the spot weld after failure is calculated using Eq. (9) through Eq. (11). In Eq. (9) the damage is determined by dividing the consumed strain energy by the total fade energy and then the softened stress in the weld ($\hat{\sigma}$) is determined based by multiplying the scaled Cauchy stress tensor (σ^{ep}) by the linear damage relation shown. To determine the amount of energy consumed thus far, Eq. (10) is used where F_{ij} is the deformation gradient and $\Delta\varepsilon$ is the strain increment which occurred over the last time step. Since the loading state can change after the onset of failure, the undamaged Cauchy stress tensor (σ^{wp}) is scaled such that the scalar product of $\sigma_{ij}^{n,ep}\Delta\varepsilon_{ij}$ is the same energy increment in comparison to $\sigma_{ij}^{n-1,ep}\Delta\varepsilon_{ij}$ making $\sigma_{ij}^{n,ep}$ equipotential to $\sigma_{ij}^{n-1,ep}$ [67] as seen in Eq. (11).

$$\hat{\sigma} = (1 - \frac{G_{used}}{2\ x\ GFAD})\sigma^{ep} \tag{9}$$

$$G_{used} = G_{used}^{n-1} + \det(F_{ij}\sigma_{ij}^{ep}\Delta\varepsilon) \tag{10}$$

$$\sigma^{ep} = \frac{\sigma_{ij}^{n-1,ep}\Delta\varepsilon_{ij}}{\sigma_{ij}^{wd}\Delta\varepsilon_{ij}}\sigma^{wd} \tag{11}$$

To bond the spot weld elements to the parent shell elements, tied contact was used which constrained both translational and rotational degrees of freedom in the contacting spot weld nodes to the parent metal surface. This was implemented in LS-DYNA using the *CONTACT_TIED_SHELL_EDGE_TO_SURFACE keyword.

5.2 Cross tension simulation

Since the cross tension specimens were not clamped within the grips of the material testing system, the fixtures needed to be meshed so that the force response of the entire system could be compared to the experimental results described in Section 4.2.2. The meshed assembly shown in Figure 87 was used to represent the experiment. To mesh the fixtures and clamping squares, elastic solid elements were used with the properties shown in Table 3. To increase computational efficiency, the bolts were reduced to a force boundary condition (green arrows in Figure 87) applied to rigid washers which held the coupon in place with of 30 kN of clamping force applied linearly in the first two seconds of the simulation prior to any deformation. After this, a second stage occurred where a velocity of 10 mm/min was assigned to the blue node set in the top fixture, mimicking the displacement of the crosshead in the experiments. The other red node set shown in Figure 87 was fixed during this stage, representing the bottom (fixed) grip in the material testing system. To enforce contact between all the components within the assembly, surface-to-surface penalty function-based contact algorithms where used. All steel-to-steel contact used a friction coefficient of 0.4 except the squares because the contact surface was knurled, so the coefficient of friction was arbitrarily doubled to 0.8.

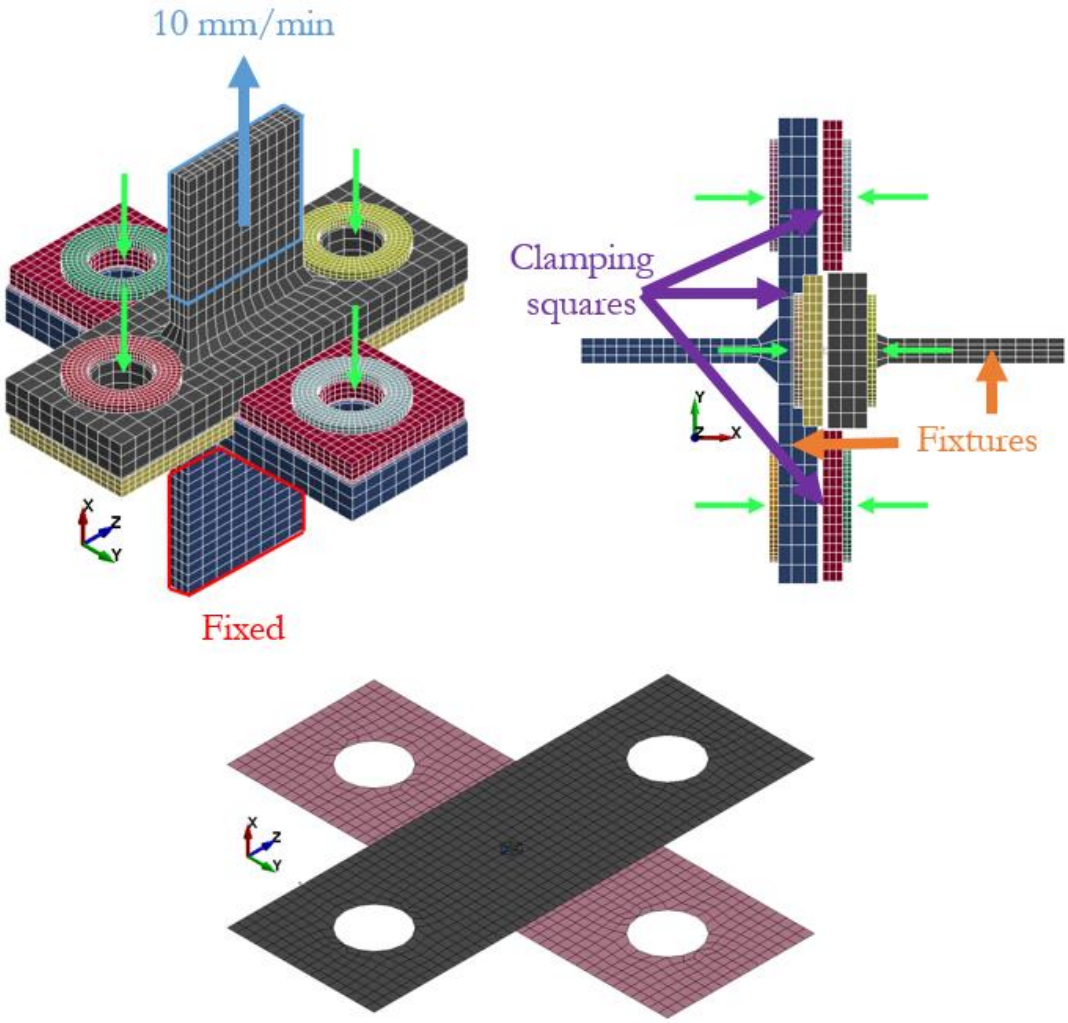

Figure 87: Cross Tension assembly (top) and coupon (bottom) mesh plot and boundary conditions

Table 8: Tool steel material properties

Density (tonne/mm^3)	7.88E-09
Young's modulus (MPa)	200000
Poisson's ratio	0.3

During the development of this simulation, a parametric study was conducted on the normal strength and size of the weld with the effects of each variable discussed in Section 5.4. This study was undertaken to highlight how the weld material properties affected the predictions.

5.3 Lap Shear Simulation

The lap shear simulations allowed for calibration of the weld plasticity model and the shear failure criterion. Since the specimen was clamped within the grips, the model was simpler than the cross tension model, as shown by the mesh in Figure 88. The mesh comprised two sheets of the parent metal represented by shell elements and bound by a spot weld beam element. A spring was placed between the top coupon and the displaced node to account for the elastic compliance of the test frame

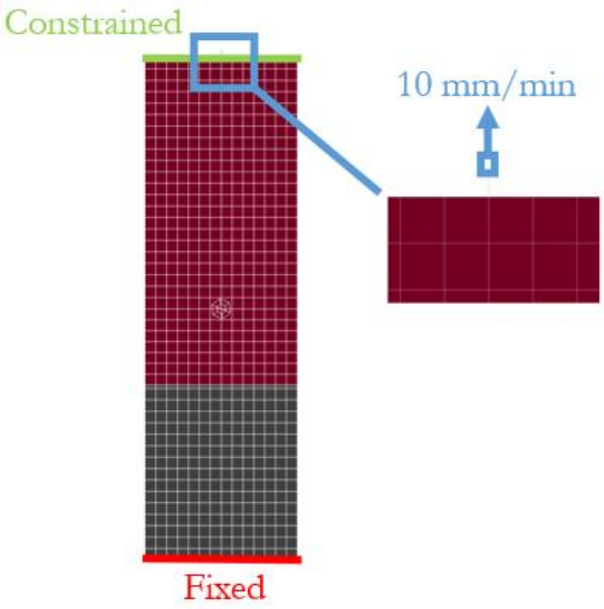

Figure 88: Lap shear mesh plot and boundary conditions

To enforce the experimental boundary conditions, the nodes at the bottom red line in Figure 88 were fixed, representing the edge of the gripped material. The top green node set was constrained such that the vertical displacements were common and a spring was placed between this node set and the top blue node. Since the MTS machine compliance was unknown, a stiffness of 80,000 N/mm was assigned based on the outer diameter and length of the circular column of the MTS. To enforce the deformation, the top node was displaced at a speed of 10 mm/min and this continued until the weld released. To account for contact between the steel components, surface-to-surface contact

algorithms were used with a friction coefficient of 0.4. For this simulation, the yield strength, hardening modulus, shear strength, and fade energy of the weld were parametrized and the effects of each variable is discussed in Section 5.4.2.

5.4 Single weld numerical results

In this section, a numerical model is calibrated based on experimental data using the meshing scheme in Section 5.1 and the material model in Section 5.2. By conducting sensitivity studies on the variables described at the end of Sections 5.2 and 5.3, a model was generated for each material condition examined in this work. The following section describes the effect of each parameter and concludes by showing the results of each calibrated material model.

5.4.1 Cross tension sensitivity study and calibrated results

In the cross tension simulations, spot weld material models were calibrated in normal loading where the weld normal strength and spot size were determined through iterative sensitivity studies. Since force and displacement measurements were the only data sampled during the test, the relationship was used to benchmark the numerical results. The nugget diameter measured on the specimens after testing was used to weld diameter in the simulation and normal strength was taken by dividing the maximum force by the spot area. To highlight the sensitivity of the material models to the calibrated values, a parametric study is presented with 1.2 mm fully quenched USIBOR® 1500-AS as the baseline.

The final predictions for all material conditions are shown in Figure 89 to align with experimental data using the material parameters shown in Table 9. Figure 90 shows the predicted

deformation of the mesh after failure for two quench conditions (1.6 mm fully quenched and 700 °C die quench) alongside the deformed samples from the respective experiments. The visual correspondence of the predicted and observed deformed shapes was good. Figure 91 (right) shows the predicted and measured peak loads for the entire range of conditions considered. Table 9. In general, the predicted loads agreed with the measured values. The accuracy of the predicted energy absorption (toughness) was not as good, with the model under-predicting toughness. Attempts were made to calibrate the absorbed energy through the fade energy (GFAD) parameter, however, the predictions did not improve. Part of the issue in the predictions is likely due to the fact that failure often occurs through pull-out of the heat affected zone which occurs within the parent metal and cannot be directly represented using standard shell elements. Further work is required to improve the toughness predictions for normal failure of the weld.

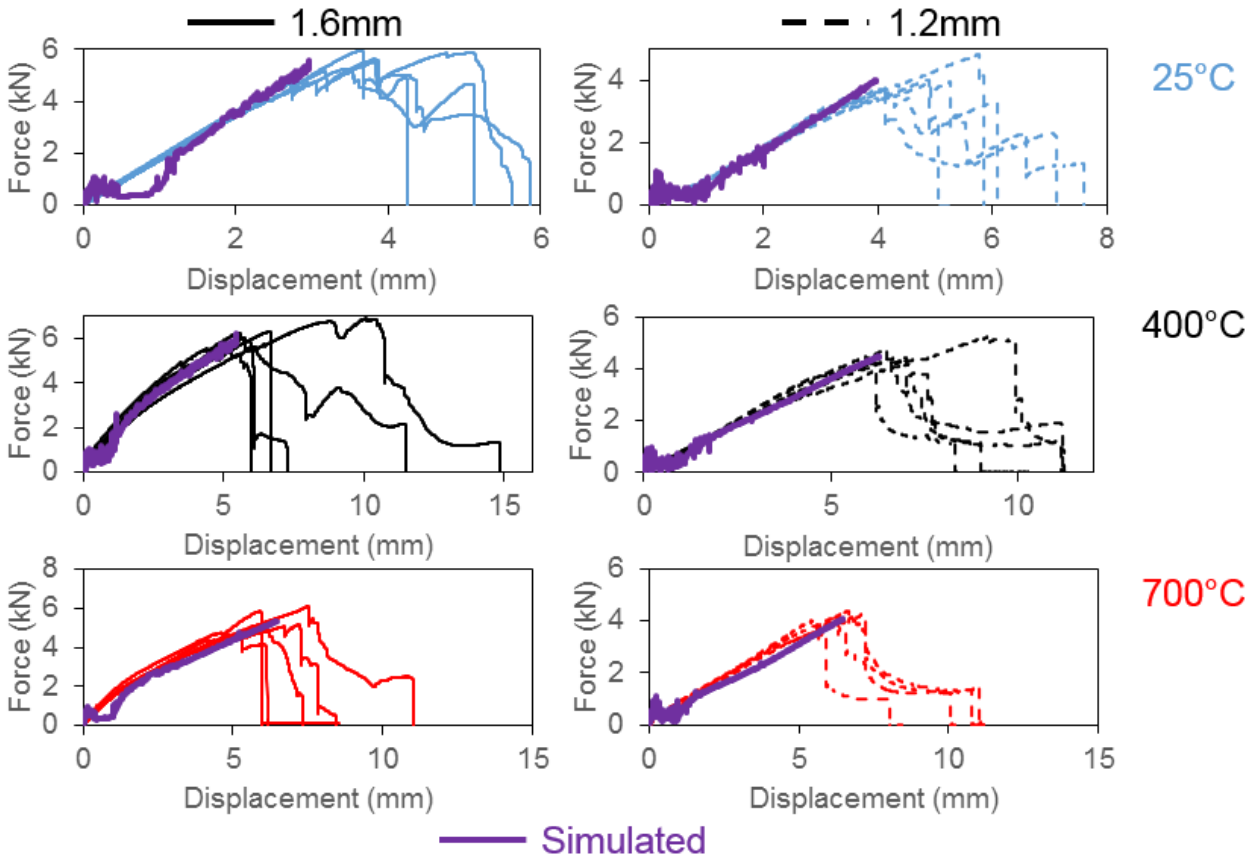

Figure 89: Final simulated cross tension results plotted over experimental data for all material conditions

Table 9: Calibrated parameters from cross tension simulations with the average and standard deviation shown from the experimental data

Material	Peak Force (kN)		Toughness (J)		Normal strength (MPa)	Weld size (mm)
	Simulated	Experiment	Simulated	Experiment		
1.2 FQ	4.0	4.0±0.4	7.2	13.7±1.7	182	5.3
1.2 400	4.5	4.5±0.4	14.3	24.3±5.4	196.9	5.4
1.2 700	4.0	4.1±0.1	13.1	21.7±3.6	185.2	5.3
1.6 FQ	5.6	5.5±0.3	7.2	17.4±2.0	250.6	5.3
1.6 400	6.2	6.3±0.4	18.3	34.7±12.3	208	6.2
1.6 700	5.3	5.4±0.5	19.2	25.4±6.0	344	4.5

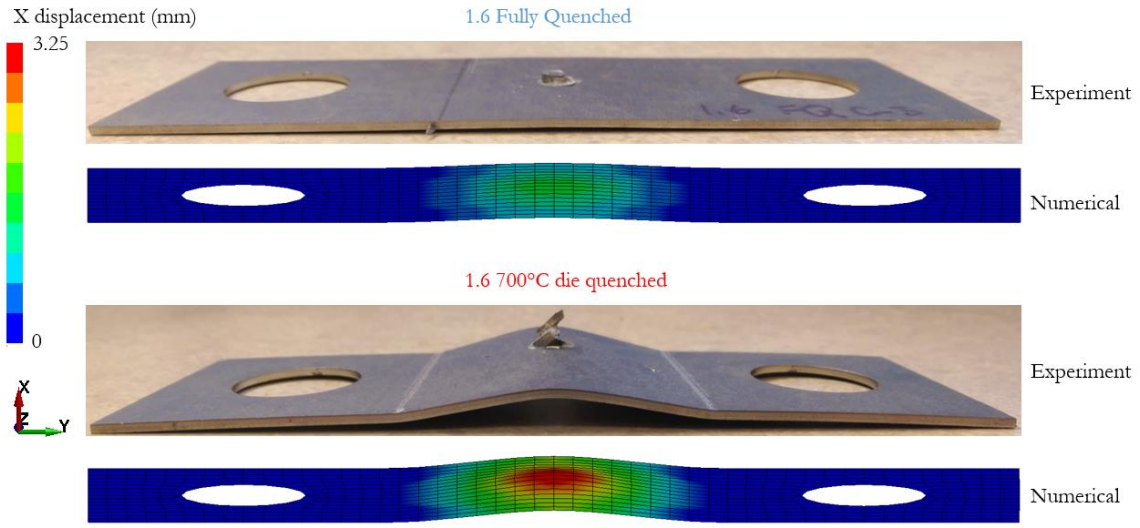

Figure 90: 1.6 mm fully hardened (top) and 700 C die quenched (bottom) cross tension predicted versus actual deformation

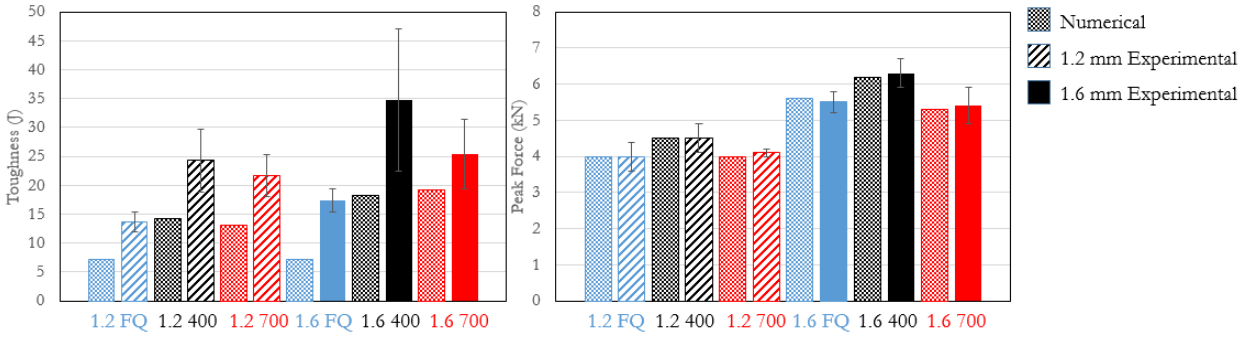

Figure 91: Bar charts comparing Toughness (left) and Peak load (right) from Cross Tension simulations and experiments

A parametric study was conducted to determine the sensitivity of the numerical model to the spot size and its normal strength. The normal strength controlled the amount of stress required to initiate damage, as shown by Eq.(5). Since the two coupons were only held together by a solid nugget, a simple force over area calculation was used to determine the normal strength. Normal strength is a construct to define normal failure numerically and therefore since it was not physical, it was adjusted to ensure the peak load at failure in the simulations aligned with the experimental cross tension data. The sensitivity of the cross tension simulation to variation in the normal strength is identified by inspecting the predicted peak loads at failure shown by Figure 92. With lower normal strength like the

100 MPa case, the specimen failed at the lowest load and displacement, as normal strength was increased the force and displacement required to initiate damage increased.

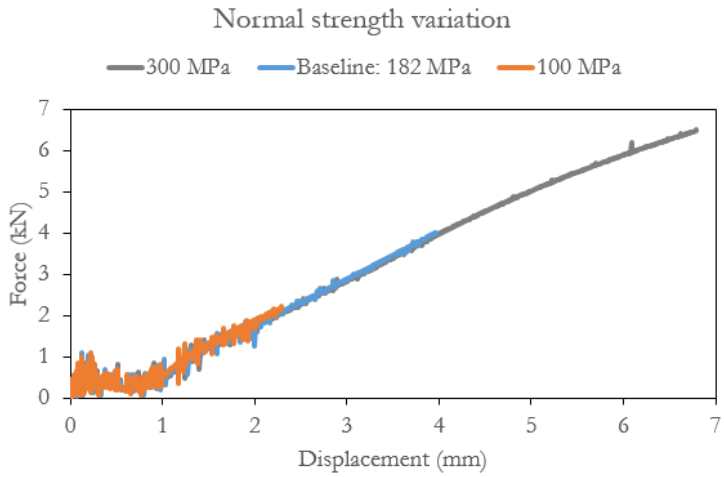

Figure 92: Effect of varying normal strength on the predicted force and displacement for a cross-tension test

In the numerical models, the weld size was constant however experimentally this parameter varied so it is important to see how variations of this value can affect the predictions. In Figure 93, the size of the weld changed the level of stress which caused the weld to fail. The normal and shear stresses compared to the user defined values are averaged over the entire welded assembly. Therefore, as the weld diameter increased, the amount of force required to initiate damage increases because the area increased.

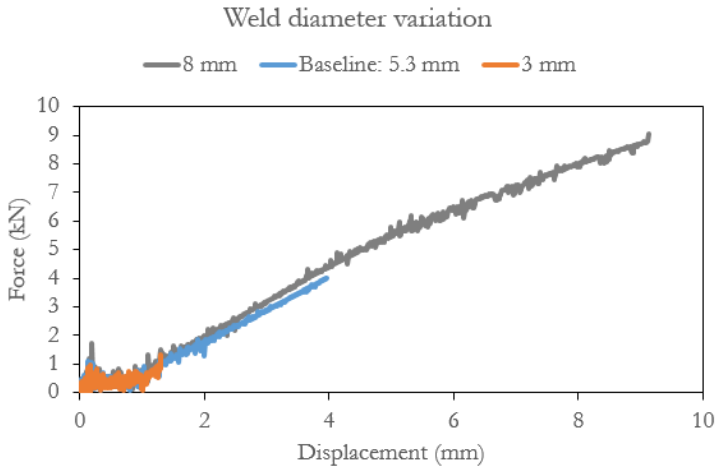

Figure 93: Effect of varying weld diameter on cross tension force displacement predictions made by the simulation

5.4.2 Lap shear sensitivity study and calibrated results

To calibrate the weld model for each material condition, first the yield strength and hardening rate were calibrated to mimic the experimental data, afterwards the shear strength was determined so the peak load of the simulation matched the experimental data and finally the fade energy was calibrated so that the simulated strain energy matched what was measured. The results from each calibrated spot weld material model is shown in Figure 94 and Table 10 with the corresponding input parameters specified in Table 11. The Y displacement (out-of-plane) of the lap shear numerical models is shown alongside the experimental data in Figure 95. Contrary to the cross tension simulations, the deformation of the specimen was not captured by the simulation. The difference in out-of-plane displacement is due to the mesh being too large to capture the localization around the weld. Physically there is a stress concentration around the radius of the weld due to the strength distribution at the weld. Numerically the boundary conditions applied to the top and bottom of the coupon could be too rigid causing the mesh bodies to be stiff. Regardless, the predictions for toughness and peak load from the lap shear simulation aligned rather well with the experimental data as shown in Figure 96.

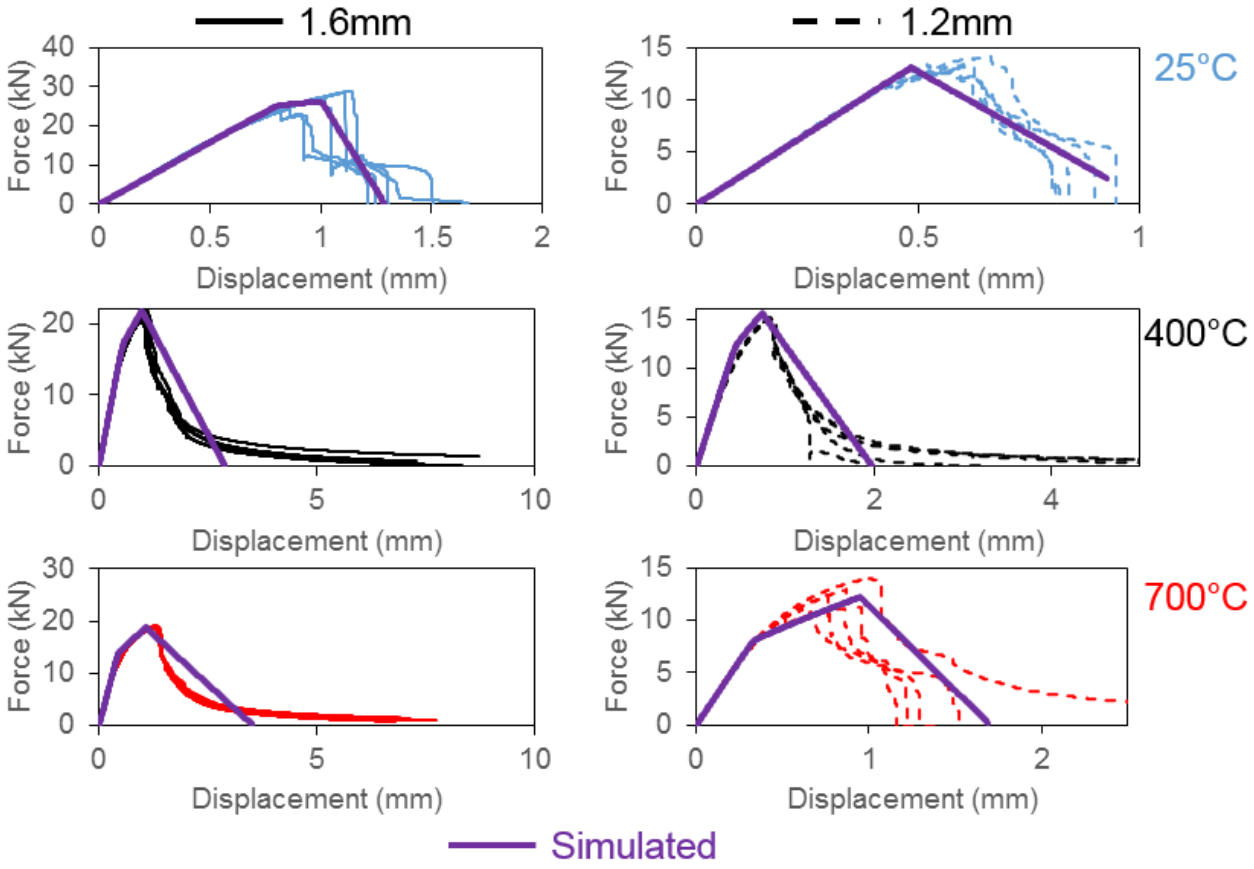

Figure 94: Final lap shear results for all material conditions overlaid on experimental data

Table 10: Calibrated results from lap shear models with the average and standard deviation shown for the experimental data

Material	Peak Force (kN)		Toughness (J)	
	Simulated	Experiment	Simulated	Experiment
1.2 FQ	13.1	13.2±0.5	6.6	6.8±0.5
1.2 400	15.6	15.0±0.1	16.6	16.7±3.0
1.2 700	12.2	12.1±1.3	12.3	12.2±6.0
1.6 FQ	26.2	26.5±2.1	19.1	19.0±2.7
1.6 400	21.4	20.8±0.6	29.2	34.6±4.5
1.6 700	18.8	18.8±0.2	36.5	36.9±1.6

Table 11: Calibrated material parameters from lap shear models

Material	Weld size (mm)	Yield strength (MPa)	Hardening (MPa)	Shear strength (MPa)	GFAD (mJ)
1.2 FQ	5.4	700	1000	600	230
1.2 400	7.5	500	1800	375	250
1.2 700	6.0	480	1400	440	200
1.6 FQ	6.1	1500	900	1050	290
1.6 400	8.7	385	1500	500	280
1.6 700	8.8	400	900	315	275

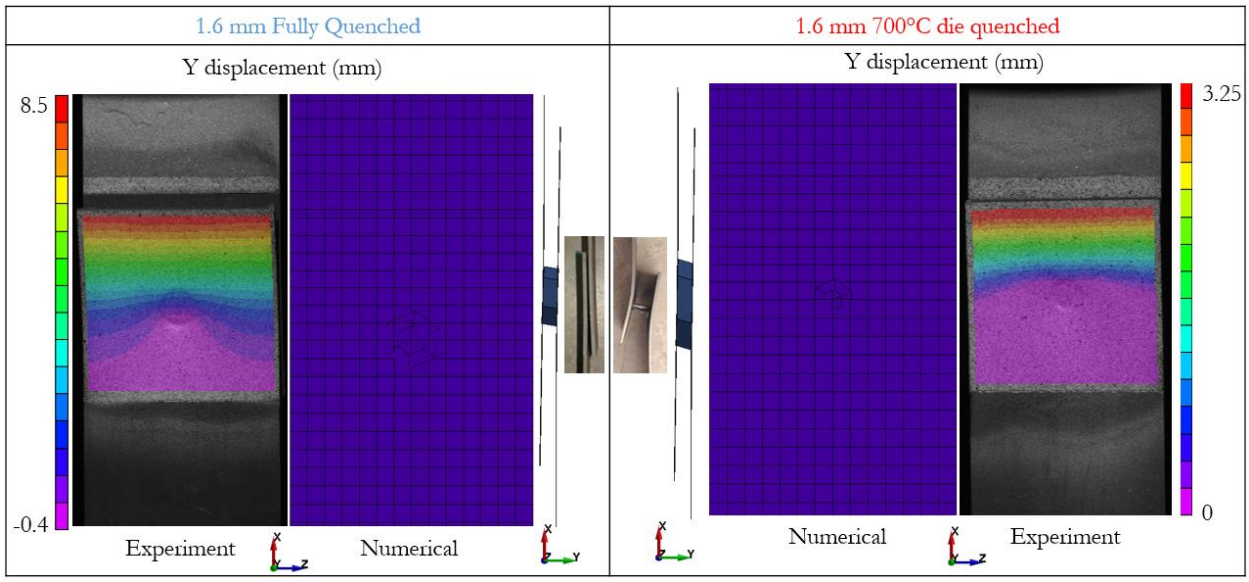

Figure 95: 1.6 mm fully hardened (top) and 700 C die quenched (bottom) lap shear predicted versus actual deformation

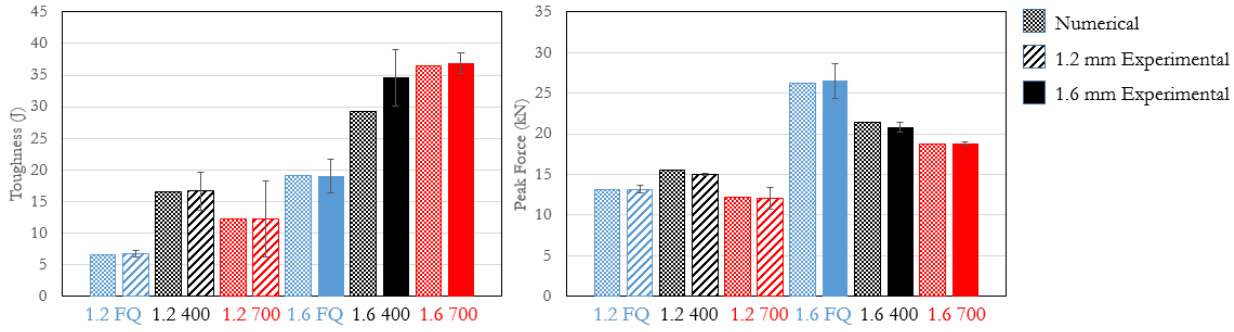

Figure 96: Bar charts comparing Toughness (left) and Peak load (right) from lap shear simulations and experiments

Although tensile and shear were used to define the stress state of the weld for damage initiation, the current spot weld model did not account for the amount of energy released by a spot weld in different stress states. While the failure response of the fully martensitic material was well suited for the material model used, the more ductile material showed fracture in the parent metal that was not captured by the model. A more robust technique would be to mesh the weld region more finely and then define each material throughout the region. Since fracture models are usually calibrated with small elements, a mesoscale model is required to properly calibrate a spot weld fracture model that can accurately capture the energy absorbed during weld failure.

Sensitivity studies were also conducted with the lap shear simulations so that the effect of weld yield strength, hardening modulus, shear strength, and fade energy could be shown. As a baseline for comparison, the calibrated lap shear model for 1.6 mm fully hardened USIBOR® 1500-AS model was used to identify the effects of the parametric variations. First, the yield behaviour was examined which controls the amount of deformation observed before the weld failed as shown by Figure 97. The yielding behaviour was determined by first looking at the point where the force response started to diverge from the experimental force displacement data if elastic deformation of the weld continued. By adjusting the yield strength and hardening modulus, the force predictions made by the simulation could be calibrated to match the experimental data.

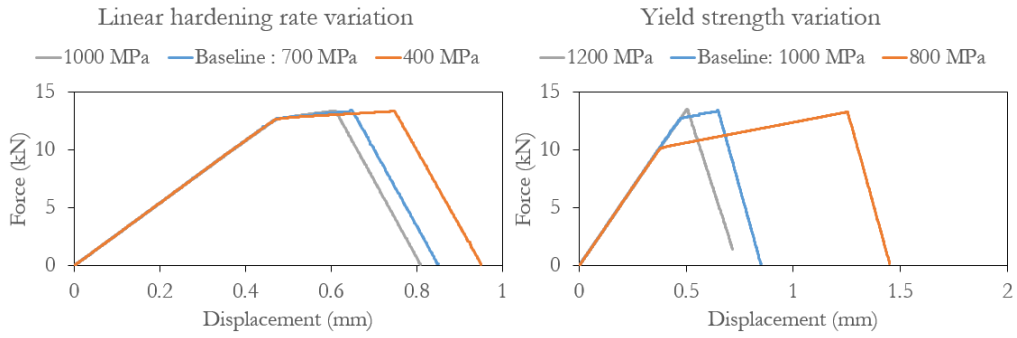

Figure 97: Effect of varying yield strength (right) and hardening rate (left) on the force displacement relation measured during the lap shear simulation of 1.2 mm fully hardened USIBOR® 1500

As discussed in Section 4.2.3, when the ductility of the parent metal was increased, so did the amount of rotation which the nugget experienced as shown by Figure 77 and Figure 78 . This produced a mixed mode loading state which was both normal and shear loading. While the lap shear test did not produce a pure shear state, shear still dominated the failure mode. Similar to the normal strength in the cross tension simulation, the shear strength controlled the peak load of the simulation as shown by Figure 98. Increasing and decreasing the amount of shear strength the spot weld could endure changed the maximum force predicted by the simulation where the simulation with 450 MPa had a peak load of 9.7 kN and the 850 MPa model had a peak force of 16.6 kN.

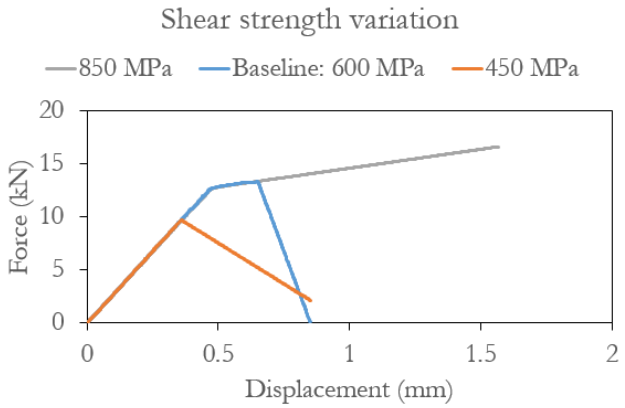

Figure 98: Effect of varying shear strength on the force displacement relationship measured over the simulated lap shear test of 1.2 mm fully hardened USIBOR® 1500

After the peak load was reached experimentally, the weld continued to absorb strain energy as fracture propagated around the weld. To account for this behaviour numerically, a "fade energy" was specified that controlled the amount of internal work done by the spot weld as it unloaded. Due to the large element size used in the modelling technique, it was not possible to match the mechanical work done during the onset of cracking as shown in Figure 95. To prevent the weld from automatically deleting after failure initiation, the amount of fade energy released by the spot weld after peak load was calibrated such that the work done by the mesh assembly matched the experimental data shown

in Figure 76. In Figure 99, the value was increased and decreased from the calibrated value to show the sensitivity to the parameter.

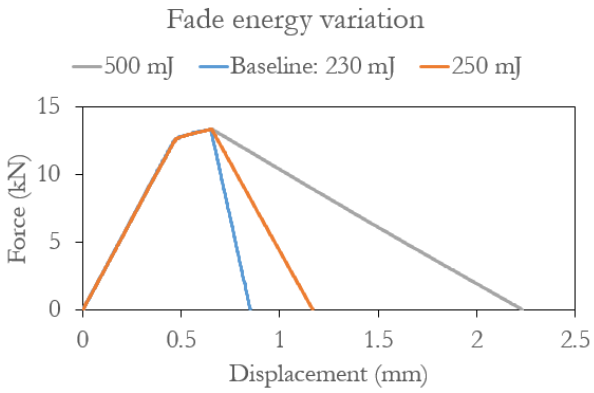

Figure 99: Effect of fade energy on the force response of measured in lap shear simulations of 1.2 mm fully hardened USIBOR® 1500-AS

5.5 Summary of Single Weld Simulations

Numerically, only the cross tension and lap shear experiments were replicated because the weld model used was intended for application in crash models that do not have the mesh density required to capture the localized deformation and fracture that occurred in the V-bend and Tensile RSW specimens. Since the cross tension and lap shear simulations were used to calibrate the weld model, the material model has not been evaluated yet since so far the model was forced to match experimental data. The real evaluation of these spot weld material models will occur when they are applied to structures in Chapter 7.

Cross tension was challenging because the displacement was measured far away from the critical region. Due to this the fixturing needed to be modelled to capture the compliance of the system but error was introduced due to the complex surface interaction at the bolted connections. In normal loading, the spot weld model was not able to capture the softening of the weld after failure had initiated. Since the simulations were performed using an implicit solution procedure and the onset of cracking was not smooth, equilibrium was broken over the time step used in the simulation causing it to crash once fracture initiated. In terms of the numerical results, spot weld normal strength correlated to experimental data because the spot weld was in a pure tension state when damage initiated.

Lap shear was better suited for implicit modelling because the force response of the specimen during the onset of cracking was smoother, the softening profile after weld failure was less aggressive than that observed in cross tension, and there were fewer elements used to mesh test. In shear the spot weld model was able to capture the response of the RSW both before and after damage initiation since the duration of the test was smaller and the welds did not exhibit an abrupt drop in force response after weld failure. Contrary to the spot weld material parameters from the cross tension simulation, shear strength, hardening, and yield from lap shear did not correspond directly to the

experimental data. Even though the fully martensitic specimen didn't have the highest peak load experimentally, , it had the highest shear strength for both 1.2 mm and 1.6 mm specimens since less rotation occurred. Also specimen toughness increased with parent metal ductility, the amount of fade energy the weld released after failure initiation decreased for the heated die material conditions.

The spot weld model was able to capture the compliance of the joined assembly in lap shear and cross tension because all simulations have been calibrated to match the experimental data. The true test of this spot weld model will be when it is applied to structures and no modifications are applied to the material model to align the numerical predictions with experimental data. Structurally the fade energy and load sharing behaviour of RSW is critical to accurately predict the deformation of automotive crash structures. If the spot welds fail prematurely or the softening after damage is not captured properly, the structure can detach instead of deforming significantly and under estimate the response of the structure to crash. If the weld model was stronger than the physical weld the model could give a satisfactory result but when performing physical testing the structure may not perform as intended.

6.0 Spot weld group experimental results

The primary objective of this aspect of the work was to investigate the performance of resistance spot weld groups. To conduct structural testing, a new experiment was developed, dubbed the "Caiman", and was performed on the specimens described in Section 3.2 using the parts created in Section 2.3. The purpose of these experiments was to observe how spot weld failure propagated within groups of welds and how the absorbed energy, for example, was influenced by the ductility of the parent metal. In this chapter the results for quasi-static and dynamic versions of the Caiman test are discussed.

6.1 Quasi-static Mode I structural testing

Figure 100 visualizes the deformation that occurred during the quasi-static Caiman experiments. Shown are still images from the side video camera at the start of the test, the first weld failure, and the end of the experiments for each material condition. Note that the 1.2 mm specimens represented the first round of testing and afterwards, process refinements were made when testing the 1.6 mm material to improve the procedure. For the side images, a backdrop, weld location markers, and LED lighting were implemented for the 1.6 mm data. In the fully martensitic condition, the majority of the strain energy was absorbed by the spot welds and this caused fracture to propagate down the weld line rapidly, producing the largest amount of weld failure for a given load point displacement. For the tailored flange conditions, for which the flanges consisted of 400°C and 700°C die quenched material, more energy was absorbed through the deformation of the flanges that caused the weld line to exhibit a stronger, more stable fracture mechanism because strain energy was more evenly distributed throughout the specimen. As a crude measure of weld failure propagation, the side video served as a visual means of determining when each weld failed but since only one side was

captured, it did not fully capture all of the failure events because the flange on the opposite side of the sample was not visible.

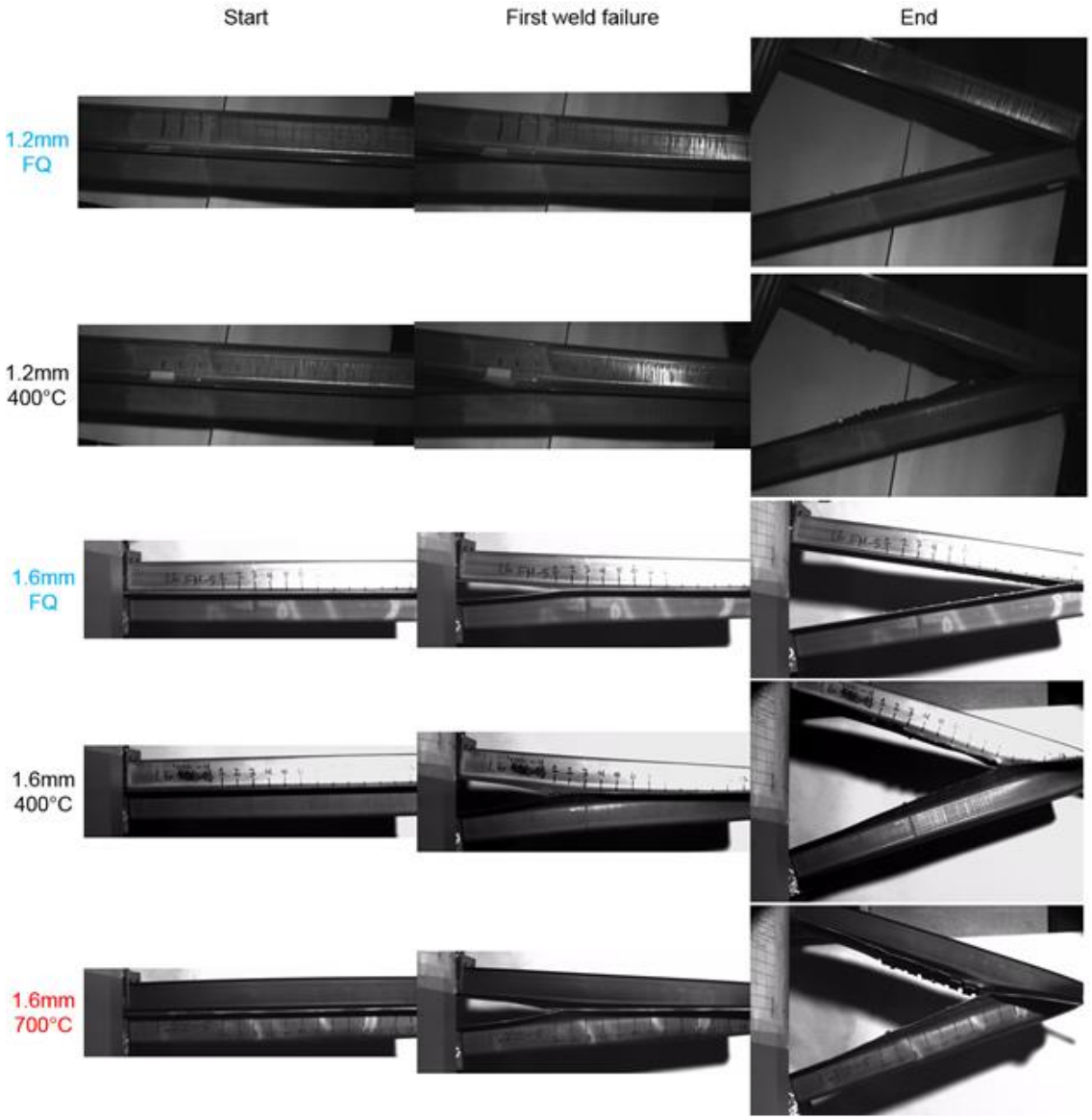

Figure 100: Side images taken at the start (left), first weld failure (center), and end (right) for all 1.2 mm (top) and 1.6 mm (bottom) quasi-static forming conditions

6.1.1 Quasi-static Caiman weld failure modes

After conducting each test, the recovered specimen was to assess the weld fracture mode based on the fracture surfaces shown in Figure 101 and Figure 102. In the martensitic material, interfacial, partial interfacial, and pull out weld failure was observed with fracture contained within the weld region. For the tailored material, fracture occurred at the edge of the weld close to the side wall which then propagated around the weld out the flange. While all specimens experienced the same top pin displacement, the ductile materials showed superior weld performance because the parent metal deformation and fracture delayed crack propagation across the spot weld group along the flange. As shown by Figure 101 these fracture mechanisms and the corresponding strained volume affected the number of welds which failed in the assembly. The fully hardened 1.6 mm material had the lowest volume of strained material causing 12 welds to fail along the flange. In contrast, the 1.6 mm tailored flange specimens had only 8 weld failures because a larger amount of metal was straining, delaying crack propagation.

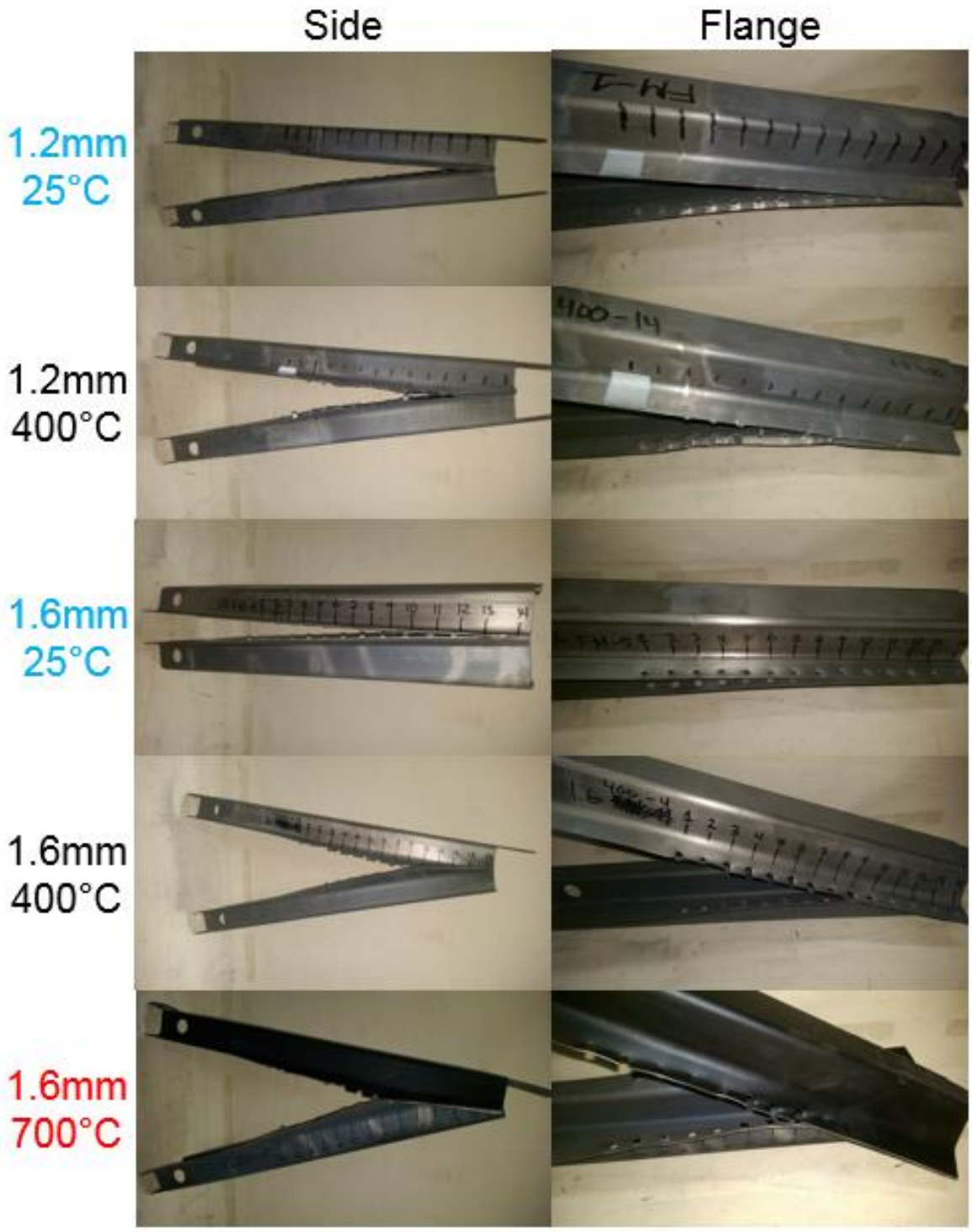

Figure 101: Side (left) and flange (right) images of quasi-static caiman specimens after testing for all material conditions tested

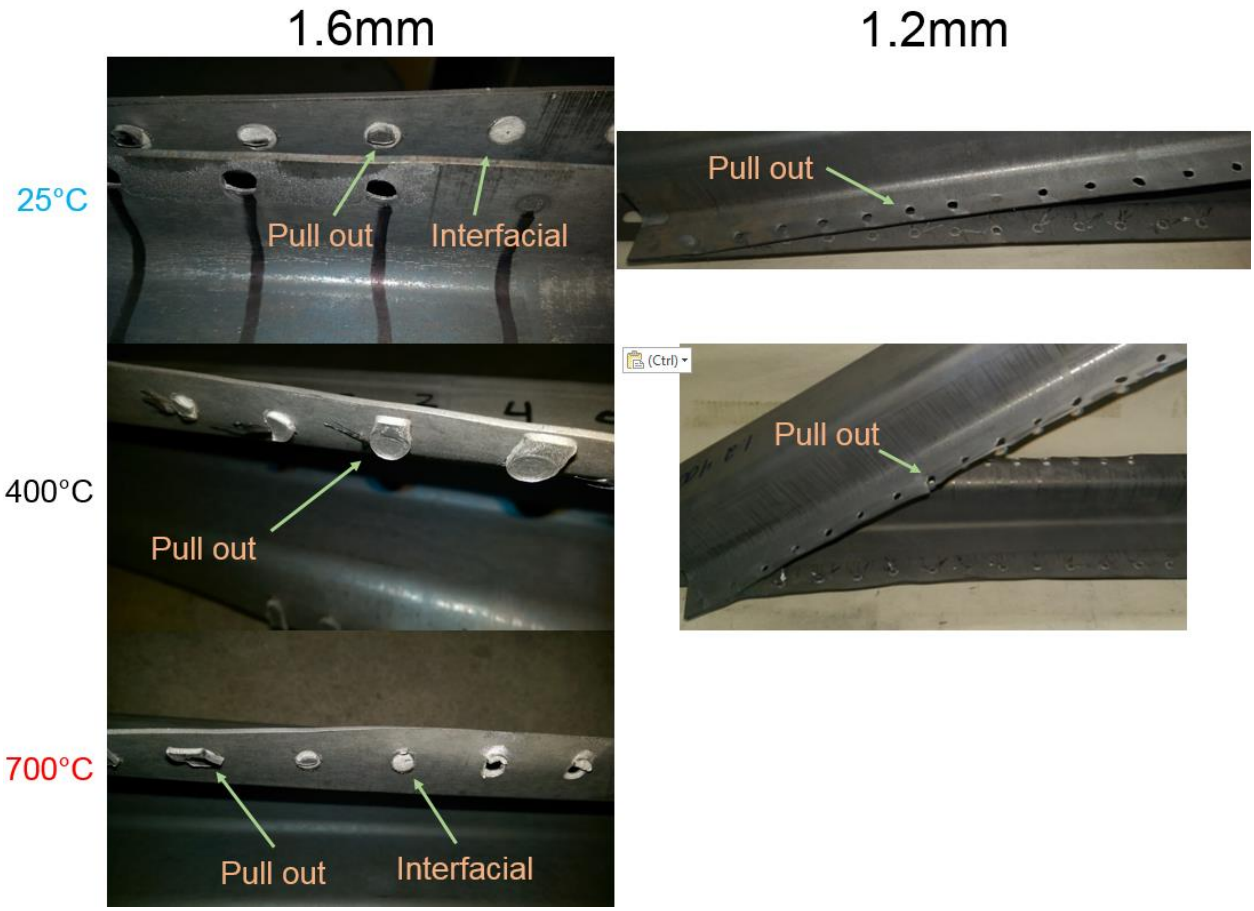

Figure 102: Weld failure modes from quasi-static caiman tests

6.1.2 Quasi-static Caiman mechanical response

In Figure 103, the force-displacement results gathered from quasi-static testing are shown. Looking at the data, the scatter seen between tests is large. As the weld electrode tips became worn, contact properties changed and the thermal load input into the material is altered [70] causing the welds to experience geometric and microstructural variations as the electrode cap wore. Even though there was variation in the observed fracture mode and force response, the materials appeared to be contained within response corridors that outline the upper and lower bounds of weld line strength in mode I unloading. The fully martensitic material tested showed both nugget pullout and interfacial failure, as shown in Figure 102, but consistently had the most aggressive crack propagation and

variation. Due to the presence of either initial weld defects or HAZ softening, the joints detached causing the overall strength of the assembly to be compromised. In the 400°C and 700°C tailored flange conditions, pull out was observed as shown in Figure 102 which was more stable and caused the weld to exhibit a less abrupt force drop.

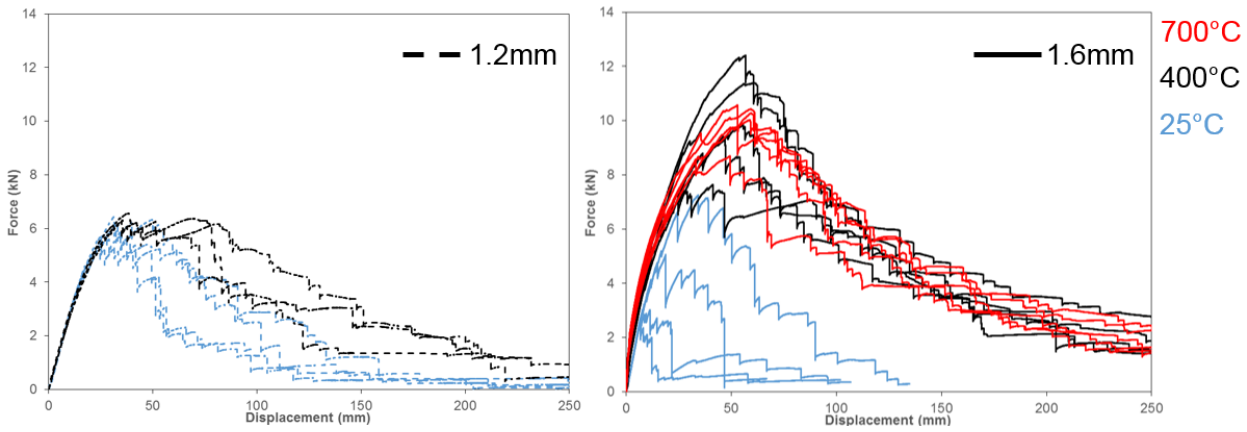

Figure 103: Force versus pin displacement plots for all quasi-static caiman testing. Note that the 1.2 mm, 700 °C condition was not tested.

Absorbed energy was calculated by integrating the force-displacement data for each experiment. As shown by the plot of absorbed energy in Figure 104 for the quasi-static results gathered, the stiffness of the parent metal had a clear effect on the response of the specimen. In the fully martensitic material where weld failure propagated suddenly down the weld line, a lower level of energy was absorbed because the hat channels detached through weld failure before absorbing significant strain energy. In the Section 4.1 the Mode I response of RSW in each tailored grade was shown to be similar but in ductile material plastic deformation was enabled prior to weld failure. With increased parent metal ductility, the energy absorption capabilities of the caiman specimen were almost doubled. Interestingly, the difference in parent metal strength between the 400°C and 700°C tailored samples seemed to have little effect on the absorbed energy response of the specimen because the

strength gradient introduced by the weld as shown in Figure 54 likely produced similar loading conditions in both 400°C and 700°C tailored flanges.

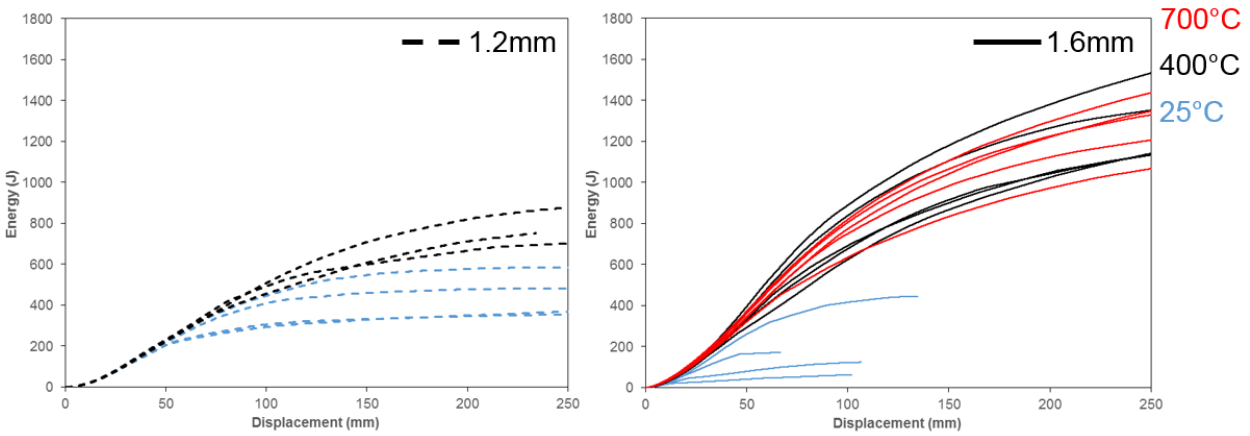

Figure 104: Energy versus pin displacement for all quasi-static Caiman experiments

6.1.3 Quasi-static Caiman strain and thermal measurements

In the first round of testing conducted on 1.2 mm fully quenched and 400°C tailored flange specimens, DIC measurements were performed on the first weld of the specimen in an effort to measure the local strain distribution at failure initiation. As shown by Figure 105, the strain measured on the surface of the specimens was quite low since the majority of the deformation (strain) acted through the thickness of the flange (as in weld pull-out response) or within the weld nugget (for interfacial failure) and could not be measured using DIC techniques. Since the DIC measurements did not show any strong trends, future experiments did not consider DIC measurement of the surface strain fields.

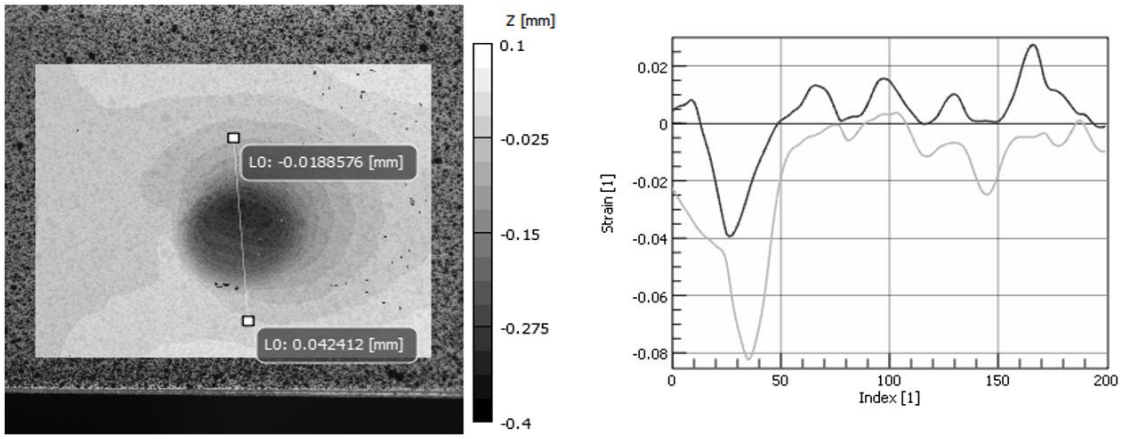

Figure 105: Out-of-plane position (left) and principal strain along the line slice (right) for the first weld of a 1.2 mm 400°C tailored flange specimen

Although the side images provided a qualitative means of assessing weld failure, it was not a robust procedure because there was no quantifiable measure of weld failure. To that end, thermal imaging was used so that the heat generated by plastic deformation could be monitored and compared to the rest of the measured data. As shown in Figure 106, there was a clear thermal spike when the welds released. Since these tests were quasi-static, there was enough time for the material to dissipate the heat as the specimen was strained causing a temperature gradient of only a few degrees Celsius at fracture. Nonetheless, the time and location of the thermal peak were useful to identify the instance of individual weld failures which could then be correlated with the pin displacement and force measurements. Qualitatively, the thermal images also provided a means to assess how strain energy was being distributed in the specimen as it deformed. In the fully hardened specimens, a small region experienced an abrupt thermal increase corresponding to the weld failure. In the tailored Caiman samples, a smoother thermal gradient was observed to surround the weld, highlighting the ability of the softer parent metal to deform plastically and absorb energy.

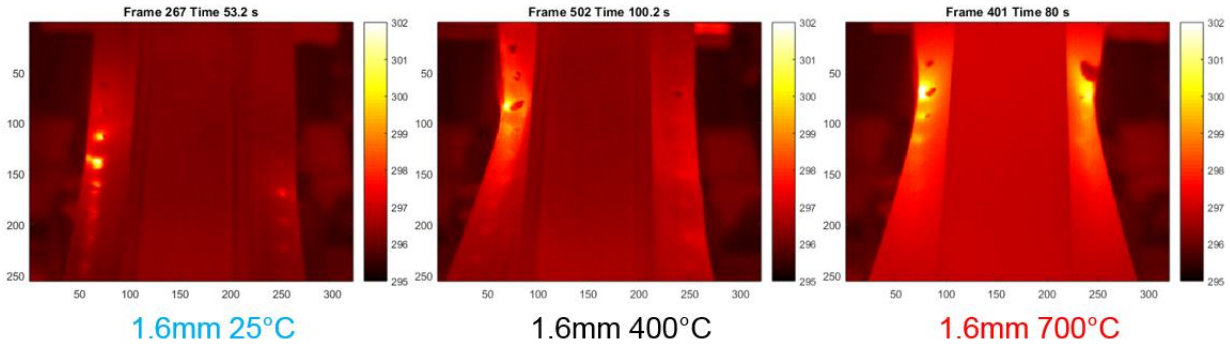

Figure 106: Black body thermal images in Kelvin of three weld release failure modes for fully quenched (left), 400°C tailored flange (center), and 700°C tailored flange (right)

The thermal imaging system was acquired by the research group while this work was in progress so the operating procedure changed as greater familiarity was gained with the system. Initially, specimens were tested without surface preparation. As shown in Figure 107, these specimens showed a thermal spike in the deformed region but the temperature reading was influenced by the flaking off of the Al-Si coating that changes the local emissivity of the material. In an effort to obtain more accurate data, the specimens were sand blasted prior to testing and the results are shown beside the coated image in Figure 107. This surface preparation improved the temperature distributions measured at the weld but as the channel deformed, regions of the surface started to reflect heat from the surrounding environment. As a final measure, the specimens were sand blasted and then painted black, producing the most consistent results, shown at the left of Figure 107. The specimen shows the highest temperatures in the regions dissipating mechanical work and reflects little heat from the surrounding environment.

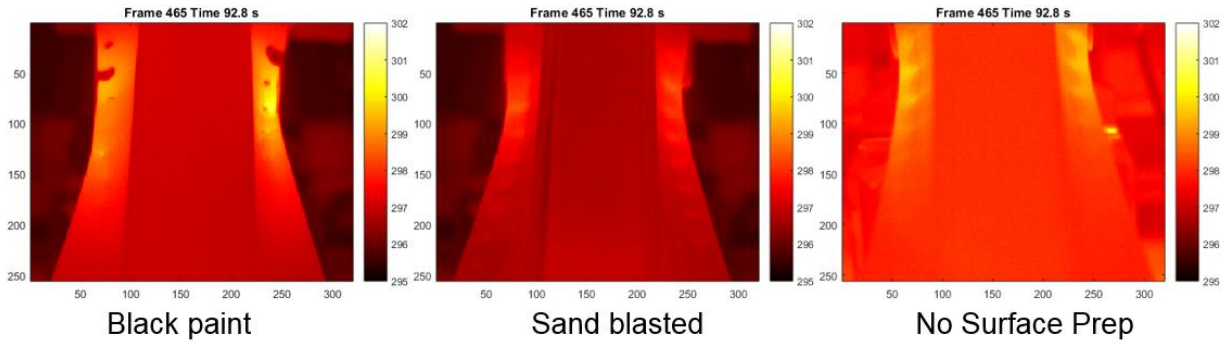

Figure 107: Thermal images taken at 77.3 mm of pin displacement for 700°C tailored flange specimens with black paint (left), sand blasted (center), and as-welded (right) surface preparations

Through observation of the thermal videos, the pin displacement at each weld failure could be determined by matching the recorded pin displacement time history from the MTS DAQ system to the time of the temperature spikes in the thermal images, as shown by Figure 108. The "crack" extension plotted in the figure corresponds to the advance of the crack as each weld fails. The failure process is discrete and the steps seen in the crack extension are equal to the weld pitch of 25 mm. For the fully martensitic material, the crack propagated rapidly, showing a steep slope, whereas the tailored steels had a lower rate of crack growth corresponding to a higher toughness of the specimen. The importance of energy dissipation in the parent metal is shown by the rapid increase in crack length in the strongest material condition (25°C quench condition) which has the lowest energy dissipation, with the rate of crack growth diminishing with increasing parent metal ductility.

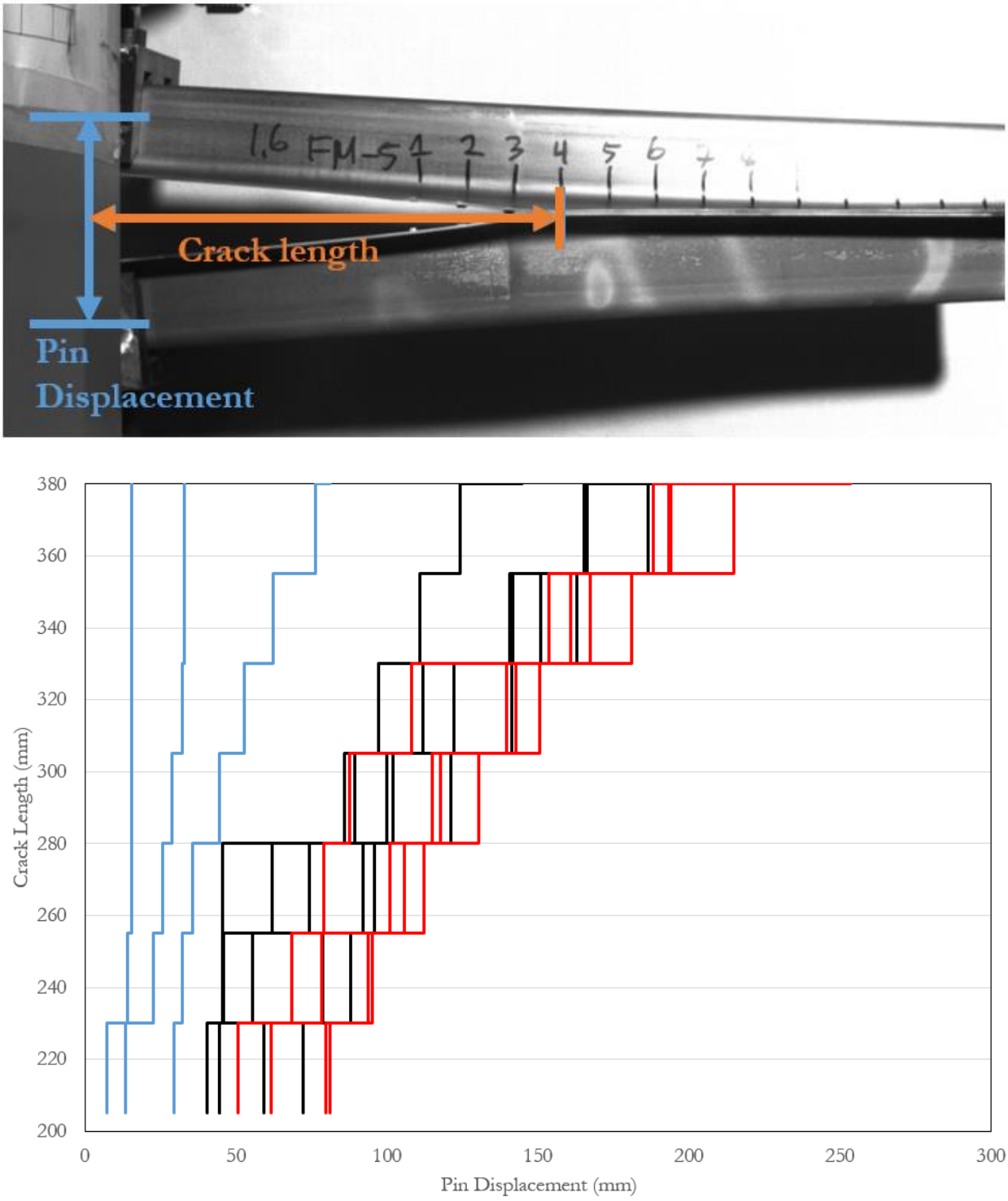

Figure 108: Crack length in quasi-static caiman specimen plotted over pin displacement for all 1.6 mm material tests. Three repeated tests are shown for each condition

6.2 Dynamic Mode I Structural Testing

6.2.1 Dynamic Caiman mechanical response

The dynamic experiments served to validate the trends identified in the quasi-static results and explore how the weld responded to high strain rate loading. To visualize the deformation during the test the side and isometric images are shown in Figure 109 and Figure 110. Similar to the crack length data shown in Section 6.1, the rate at of crack propagation through the weld line was faster in the high strength metal due to less deformation of the parent metal along with a smaller pin displacement at first weld failure compared to the quasi-static data. During testing of the 1.6 mm material, it was observed that welds on different flanges failed on opposing surfaces of the specimen. When the specimens were assembled, a DC welder was used by Promatek and this produced a direction for the thermal load applied to bond the region. Due to this welding orientation, opposing surfaces of the joined region experienced different thermal cycles producing an asymmetric material distribution about the weld center plane. Since specimens were flipped when transitioning flanges during assembly, the weaker side was on opposing sides of the specimen.

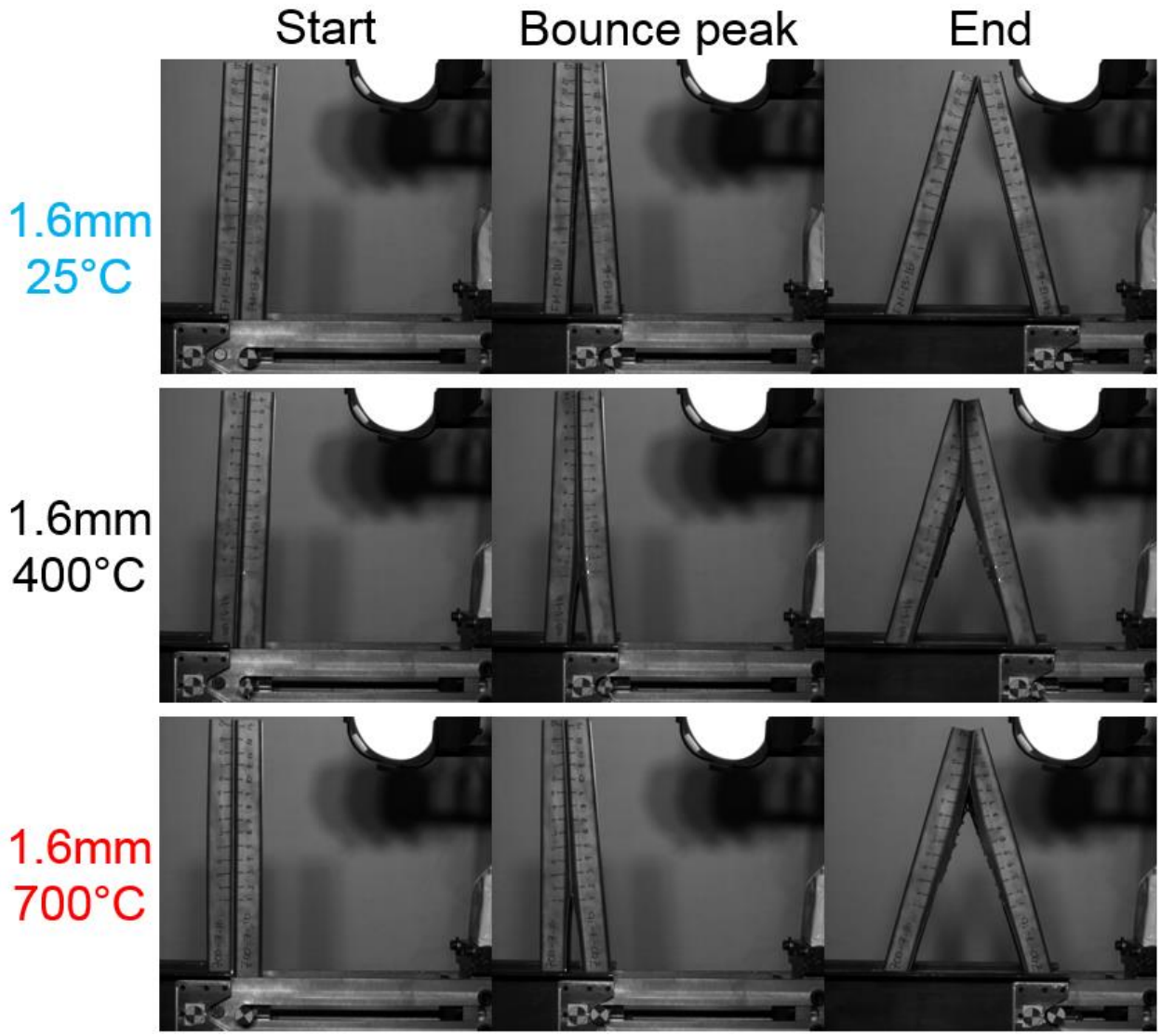

Figure 109: Side images of dynamic Caiman at start (left), peak fork and pin separation (center), and end (right)

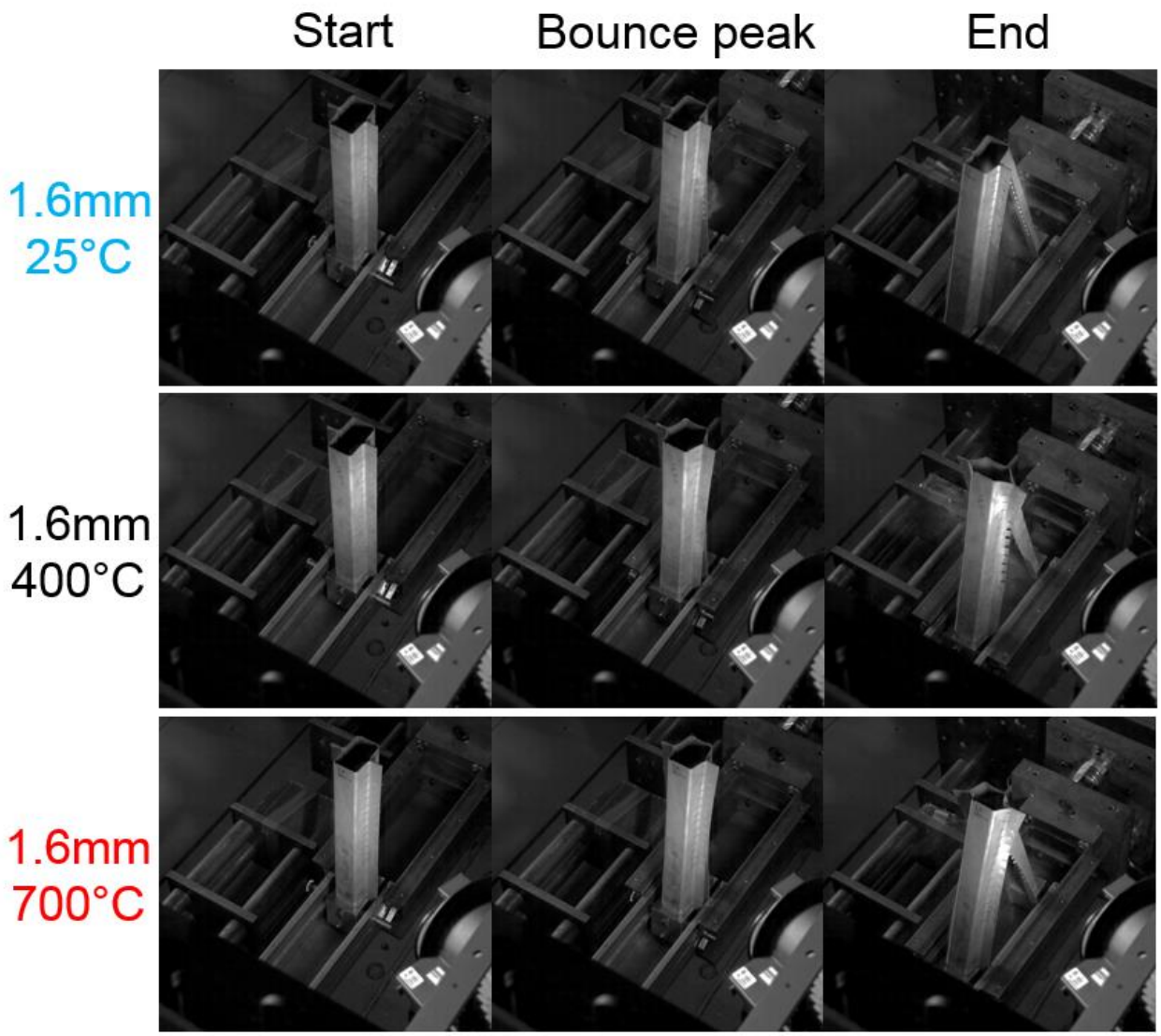

Figure 110: Isometric images of dynamic caiman at start (left), peak fork and pin separation (center), and end (right)

During testing, the impacted pin had a tendency to rebound or launch off the impactor after initial impact because of the large difference in weight between the impactor assembly and the clamp assembly. To quantify this phenomenon, displacement markers were placed on the fork and impacted pin so that the displacement could be tracked in the side video. Post processing was conducted using the software package Tracker in which, the displacement markers were tracked. The results gathered for each tailoring condition are shown in Figure 111. In this data the bouncing phenomena can be identified by looking at the difference between the position of the fork and pin. At initial impact the

pin fully engages the impactor and the minimum difference is achieved, when the difference is larger than this value it highlights that the pin is not in contact with the impactor. Loss of contact occurred both at initial impact with the pin launched off the impactor and at the end of the experiment when the sled loses velocity but the impacted pin continues forward.

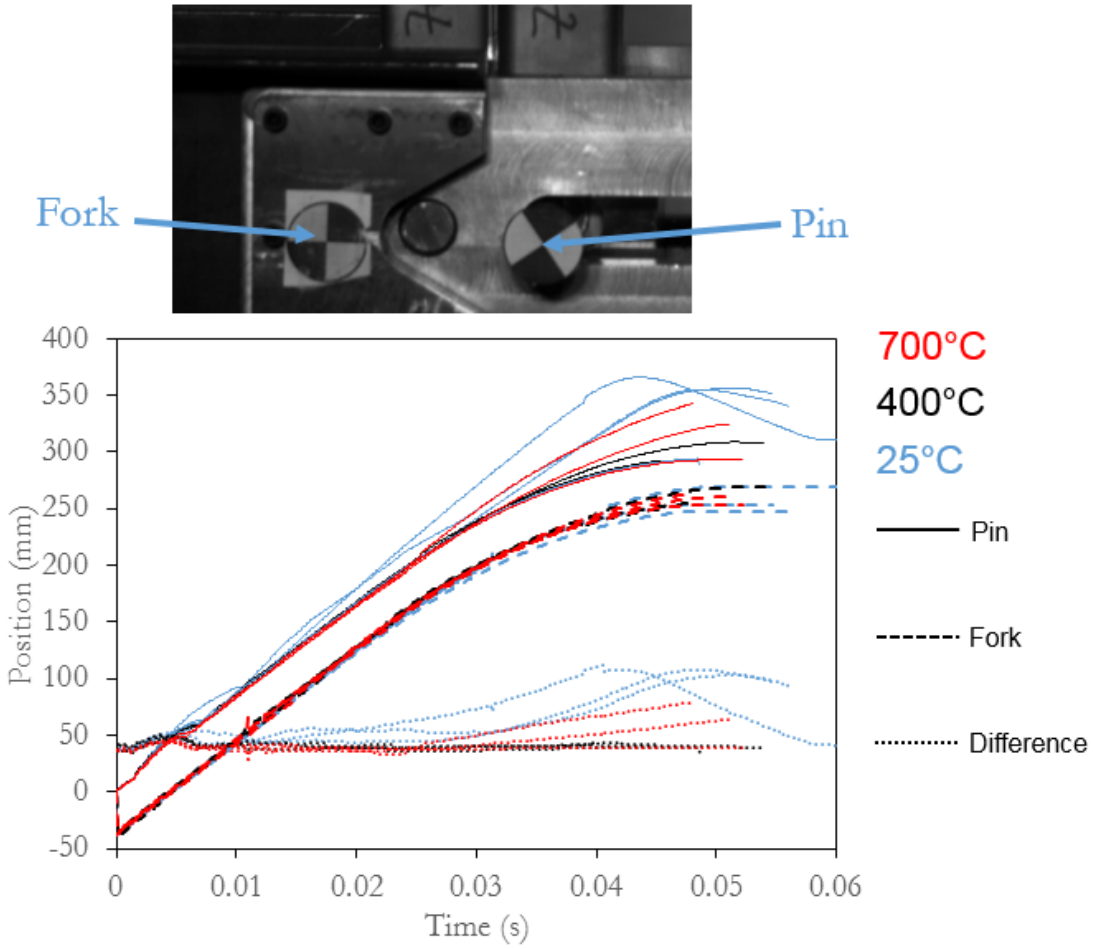

Figure 111: Position of the pin and the fork as well as the difference between the two measured points plotted over time

Comparing the response of the different tailoring conditions, the effect of parent metal strength on joint performance is apparent. For the fully martensitic material there was a large difference between weld strength and parent metal strength. Due to the strength variation, the parent metal experienced little to no plastic deformation causing the failure to propagate rapidly down the

weld line and producing very little energy dissipation, resulting in elastic rebound from the fork and intermittent contact between the impactor and pin. In the specimens with lower strength flanges, plastic deformation was observed in the parent metal, dissipating energy at failure as it propagates down the weld line, resulting in less rebound of the pin.

Force data gathered during this test on the sled and wall was plotted as a function of sled displacement, as shown in Figure 112. To support the assembly, three 120 kN load cells were used to measure the force transmitted from the sled and wall to the apparatus. Since the maximum load of the experiment was approximately 13 kN for the quasi-static testing, even if the load doubled dynamically the measurement was still roughly 10% of the load cell capacity. Since measurements were on the low end of the calibrated range of the load cells, a large amount of noise was observed in the measurement effectively washing out the load drops that were observed in the quasi-static data. For the sled data, since there was intermittent contact between the sled and the impacted pin, some load drops can be observed when the pin loses contact with the pin. For both the wall and fork assemblies, the load cells were located far away from the impact area meaning that fine details were likely washed out in the force measurement as it transmitted through the assembly. After filtering, a load drop similar to that observed in the quasi-static data is shown the force data is too noisy to identify any trend.

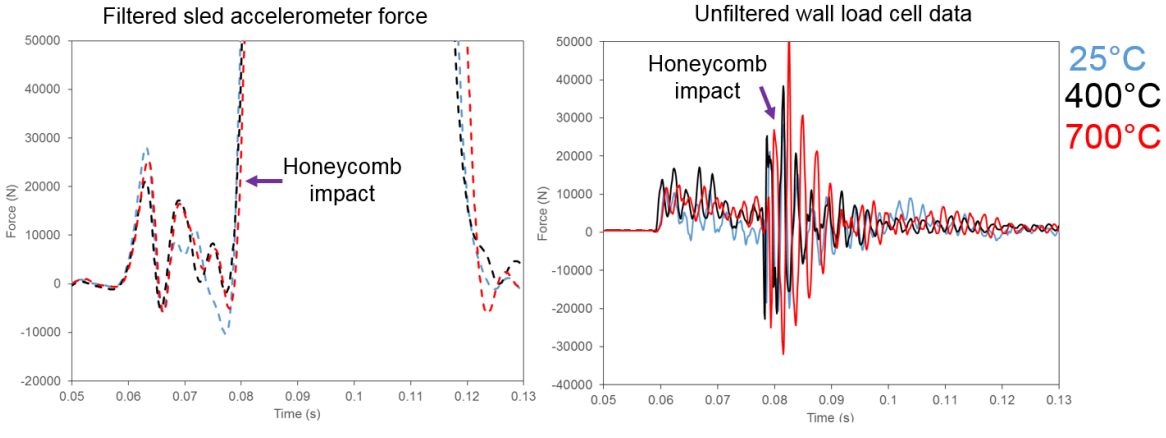

Figure 112: Averaged force data plotted over time for 1.6 mm fully quenched and tailored flange conditions

Using the unfiltered wall force and pin displacement data, the energy was calculated and plotted as seen in Figure 113. Since these results were produced by integrating the force data, some of the noise was filtered out but a small amount remained with an increase observed after honeycomb impact. The acquired absorbed energy data further highlighted the impact of parent metal ductility. For the martensitic material, similar to the quasi-static data, a smaller amount of energy was absorbed over the test. In contrast, the soft flange materials absorbed significantly more energy because plastic deformation occurred in the parent metal.

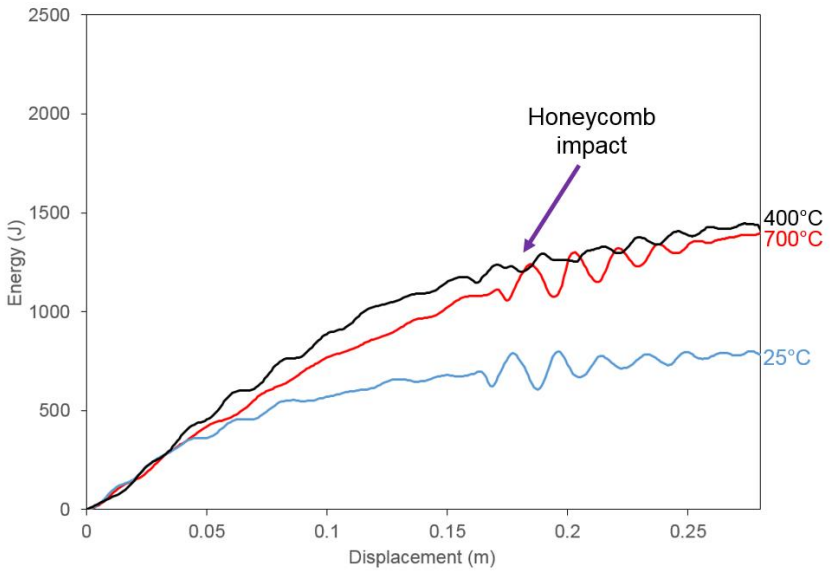

Figure 113: Average energy plotted over sled displacement for 1.6 mm fully quenched and tailored flange conditions

To characterize the influence of deformation rate on the response of the welds to deformation, the average energies absorbed for the quasi-static and dynamic Caiman experiments were overlaid, as shown in Figure 114. There was an increase in absorbed energy under dynamic loading that was observed for all tailoring conditions; however, the most significant increase was for the fully martensitic condition

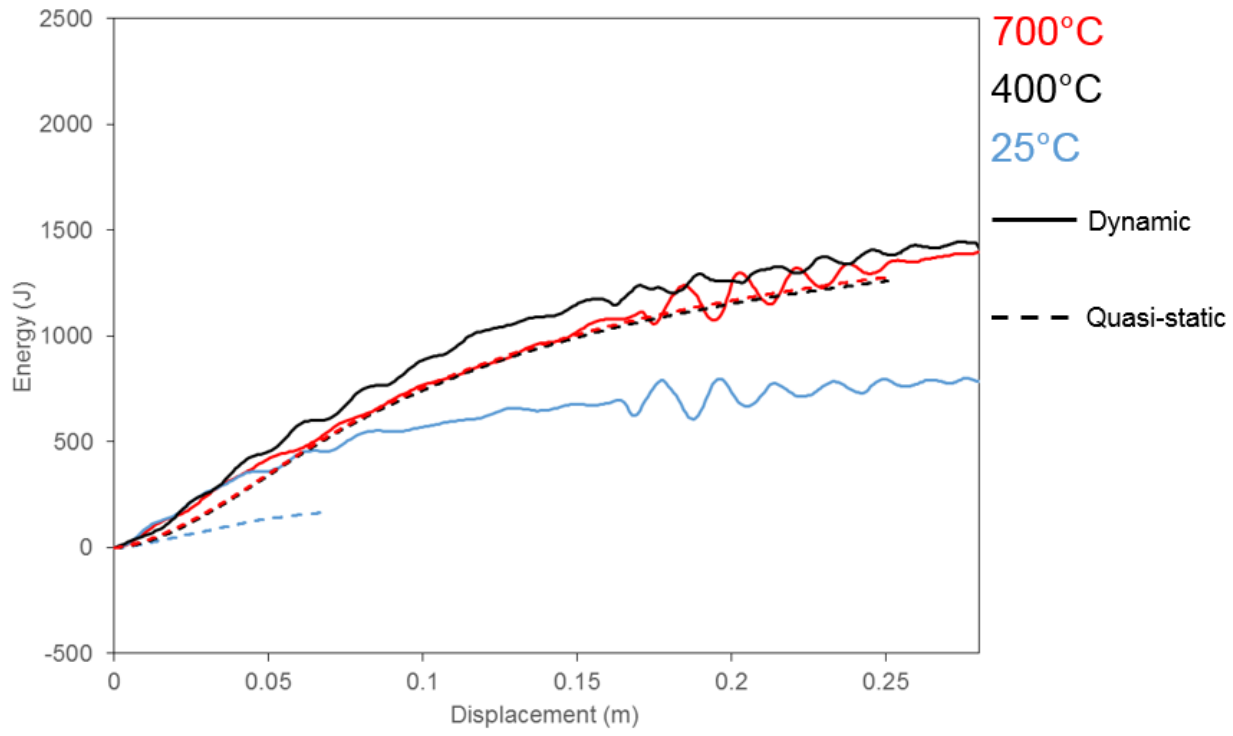

Figure 114: Average dynamic and quasi-static energy plotted over displacement for all 1.6 mm Caiman specimens

6.2.2 Dynamic Caiman thermal measurements

One of the more interesting aspects of the dynamic Caiman test was the measurements taken by the thermal camera. As shown in the images in Figure 115, a larger thermal spike was observed around the weld when fracture initiated compared to that seen in the quasi-static tests (Figure 106). In dynamic testing, the material does not have sufficient time to dissipate the heat produced during weld failure and, as a result, temperature increases of 80°C were measured, compared to only 7°C in the quasi-static experiments. The temperature was likely higher at the notch of the weld (interfacial failure) or in the HAZ (pullout) but thermal diffusion through the surface of the specimen resulted in lower recorded values. Nonetheless, the sharp temperature increase can be used to identify when and where weld failure was occurring in the dynamic experiment.

At higher frame rates, the size of the imaging window of the thermal camera was smaller to achieve a higher frame rate. Since the field of view was small, only the first few welds were visible in the thermal images. For the more ductile materials, a larger region heated whereas in the martensitic material small hot spots formed at the welds. These spots occurred because a smaller volume performed plastic work in the martensitic specimens, reducing the temperature of the material at fracture.

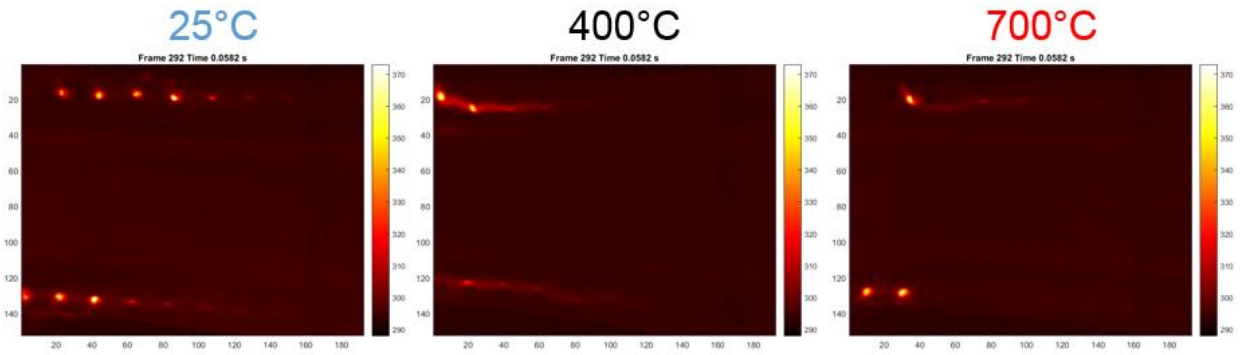

Figure 115: Thermal images from dynamic Caiman testing for all formed conditions

6.2.3 Dynamic Caiman weld failure modes

Although the fracture surfaces shown in Figure 116 and Figure 117 did not vary significantly from the quasi-static data, they served to validate the trends identified at both strain rates. The fully quenched specimen again exhibited both interfacial failure and nugget pull-out with a larger proportion of interfacial failures than seen in the quasi-static specimens. The tailored flange specimens saw interfacial failure and pull-out with more interfacial failures seen in the dynamic experiments.

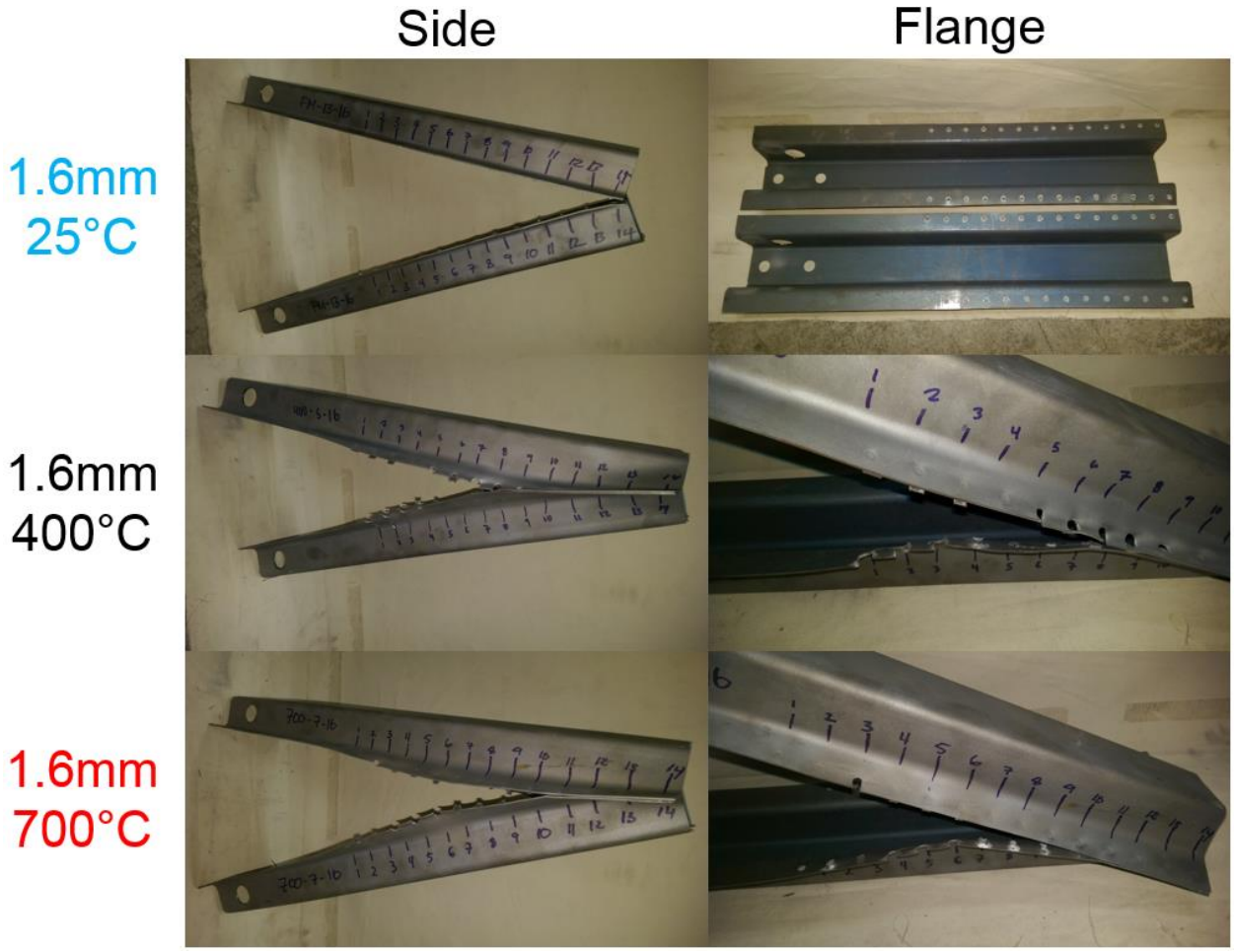

Figure 116: Side (left) and flange (right) images of tested dynamic Caiman 1.6 mm specimens in all die quench conditions

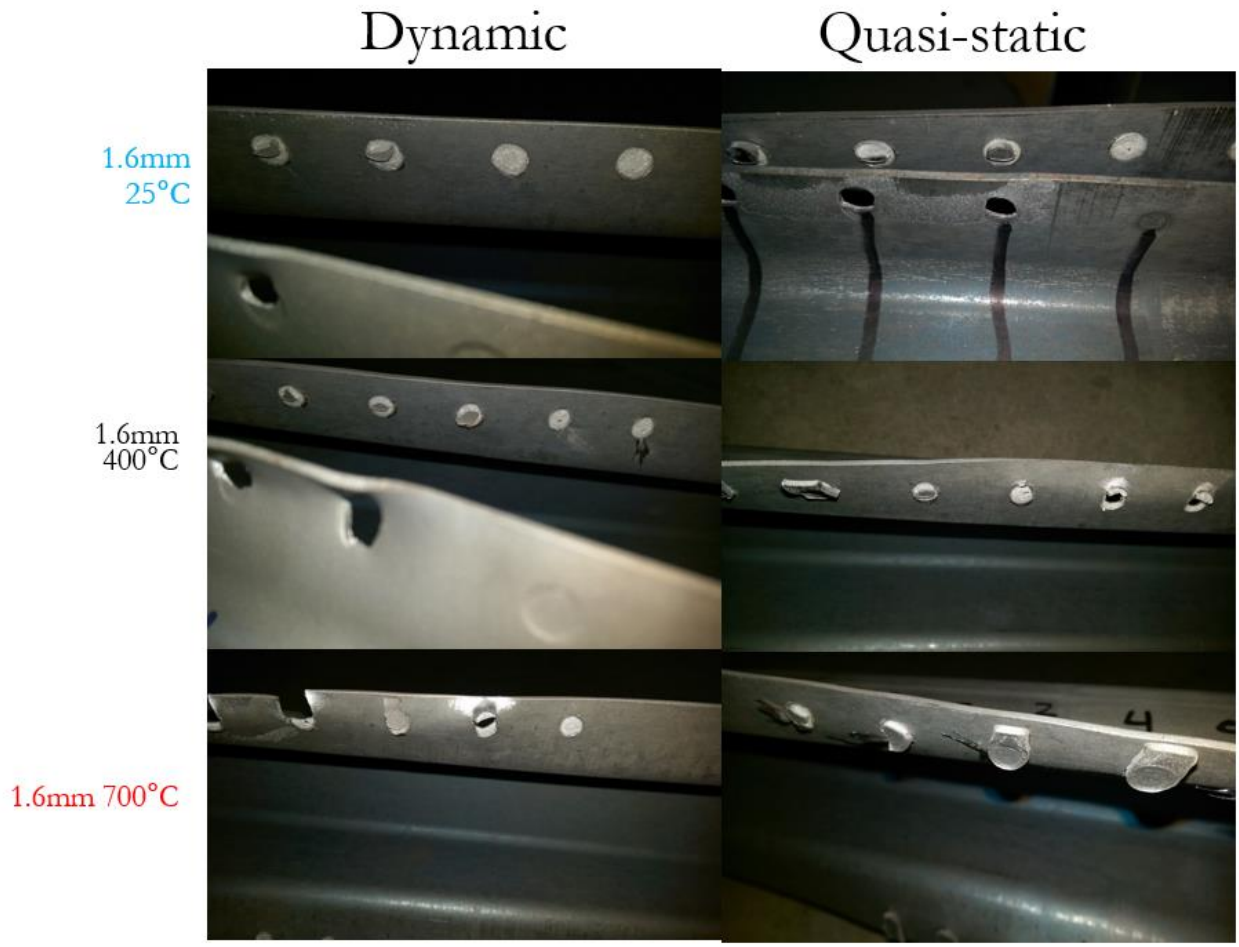

Figure 117: Weld failure modes from 1.6 mm dynamic and quasi-static caiman tests

7.0 Simulation of the Spot Weld Group Experiments

The simulation work presented in Chapter 5 focused on single weld characterization experiments. This chapter presents efforts to simulate the weld group Caiman experiments. Understanding how the welds interact with each other is crucial to properly predict deformation and fracture of a welded structure in crash. The Caiman test presents new opportunities to analyze the load sharing and fade energy behaviour of resistance spot welds at low and high rates. Here, the calibrated weld models from Chapter 5 were implemented directly into the Caiman model (without adjusting the weld model parameters) and the predictive ability of these models to model the weld groups is examined. To limit scope, only 1.6 mm fully quenched and 700°C tailored flange specimens were simulated.

7.1 Caiman numerical model

The constitutive model and fracture loci introduced in Chapter 5 for the single weld simulations were also adopted to describe the base metal response in the Caiman simulations. A remapping technique was used to assign material properties within the hat channel geometry as shown by Figure 118. For the fully quenched specimen, one set of material properties was used because it was assumed that the specimen was fully martensitic. In the 700°C tailored flange mesh assembly, the hat channel was broken into 17 bins with unique material properties assigned based on the hardness in each region using the data shown in Figure 52. Afterwards, the mesh was mirrored about the xz plane and spot weld beam elements were input to join the channels, as shown in Figure 119. These assemblies used the calibrated weld models discussed in Chapter 5 with the weld size measured in the

cross tension samples shown in Table 9. Since the specimen geometry was held constant for all testing, this mesh was used in all Caiman simulations.

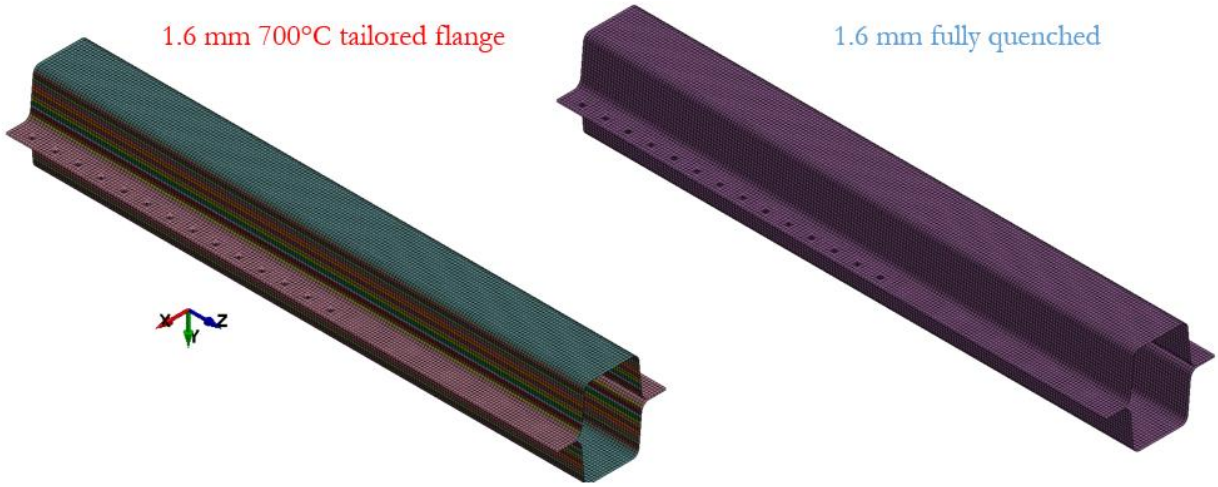

Figure 118: 1.6 mm 700°C tailored flange (left) and fully quenched (right) meshed hat channels

Figure 119: Mesh plot of Caiman specimen

7.2 Quasi-static Mode I Caiman Simulations

In the quasit-static Caiman tests, the measured force-displacement and thermal data allowed for precise determination of when and where welds failed. This section presents the application of the single weld models within simulations of the quasi-static Caiman experiments. In this section, the modeling technique is shown and the predictions made are compared to the experimental data shown in Chapter 6.

7.2.1 Quasi-static Caiman model

To match the experimental boundary conditions, the tooling described in Section 3.2.1 was meshed, as shown in Figure 120, and boundary conditions were prescribed to mimic the experiment. The clamps and pins were defined using fully integrated solid elements (solid element type 3 in LS-DYNA) using a linear elastic material model with properties corresponding to steel. Similar to the loading in the experiment (Figure 64), the bottom node set in red was fixed in all degree of freedom, but free to rotate about the x-direction while the top node set in blue was similarly constrained, but displaced upwards (y-direction) at a speed of 50 mm/min. The pin displacement was continued for 300 seconds producing 250 mm of total displacement. Surface-to-surface contact algorithms were used to enforce contact between the tooling and specimen with a coefficient of friction of 0.4 for tooling surfaces in contact with the specimen and 0.2 for contact between the pin and tooling fixtures.

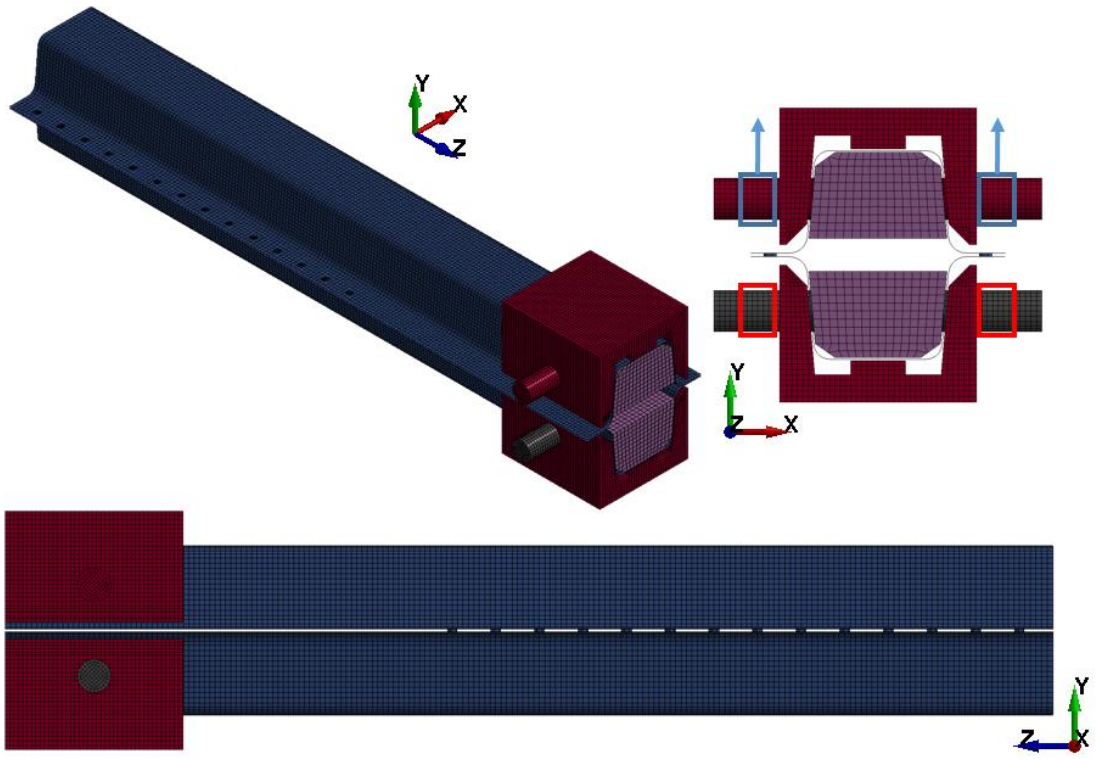

Figure 120: Mesh and boundary conditions used for the quasi-static Caiman model

Since the quasi-static experiment occurred over a relatively long period of time (compared to the dynamic tests), mass scaling (20,600% increase) was applied to the model to increase the time step of the simulation to $5*10^{-5}$ s. Mass scaling was employed so that the overall computational time could be cut down to a reasonable duration. Contrary to the single weld modelling, implicit simulations were avoided due to the sudden unloading associated with spot weld release as exhibited by the martensitic specimens in Chapter 6. Only explicit analysis would be sufficiently stable to enable the solution to advance as each spot weld progressively failed.

7.2.2 Quasi-static Mode I Caiman predictions and comparison with experimental data

The predicted and measured force-displacement responses are shown in Figure 121 for the fully quenched and 700˚C tailored flange quasi-static Caiman. For the fully martensitic specimen, the force response matched the experimental data during elastic deformation but since the softened HAZ was not modelled, the welded assembly was overly stiff causing the peak load to be reached sooner and failure to propagate rapidly down the weld line. For the 700°C specimen, the response was accurately predicted up until weld failure. However, the peak load predicted by the simulation was lower than observed in the test. After the peak load, the simulation sees a more drawn out propagation of weld failure along the weld line, relative to the response of the martensitic specimen due to the ductility of the base metal.

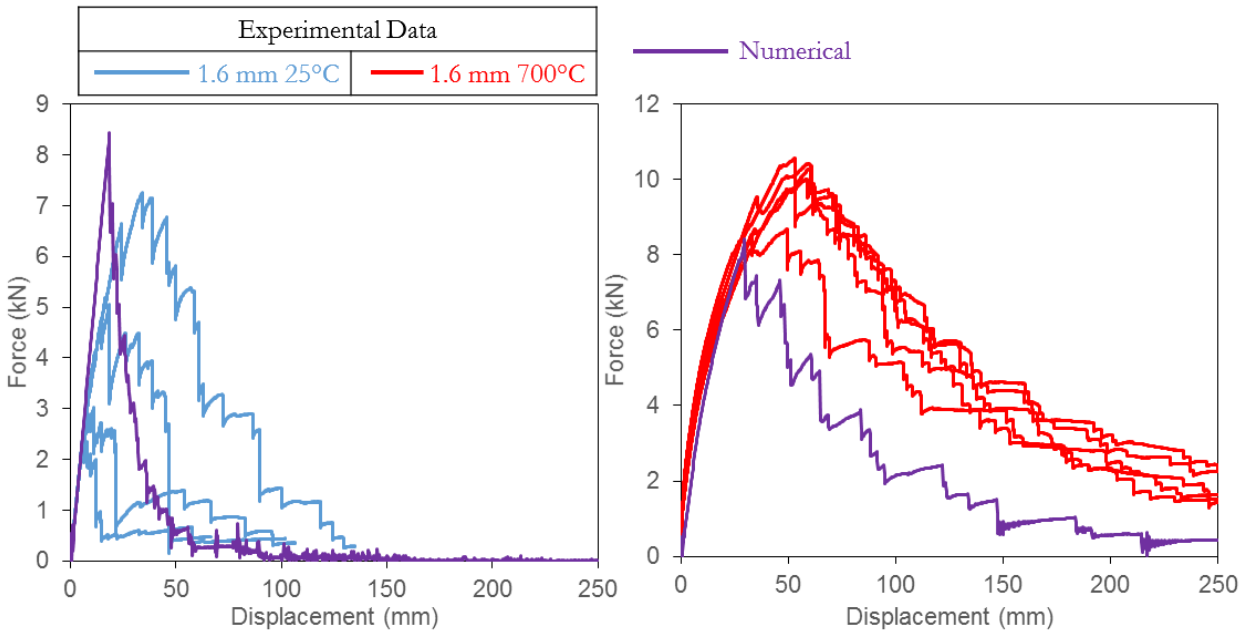

Figure 121: Comparison between numerical and experimental quasi-static caiman force response

By integrating the force *versus* pin displacement response, the toughness (energy absorption) of the specimen can be quantified. A comparison between the numerical predictions and experimental data is shown in Figure 122. Since the fully martensitic simulation peaked before the experimental data, there is a brief period when the energy predicted by the simulation is higher, but remains constant after 78 mm of displacement because the reaction force level was low. For the tailored flange, the energy predictions were low since the simulated peak load was lower than the experimental data. Despite these quantitative differences, the model does capture the increase in energy absorption between the fully martensitic and tailored (soft) flange Caiman specimens.

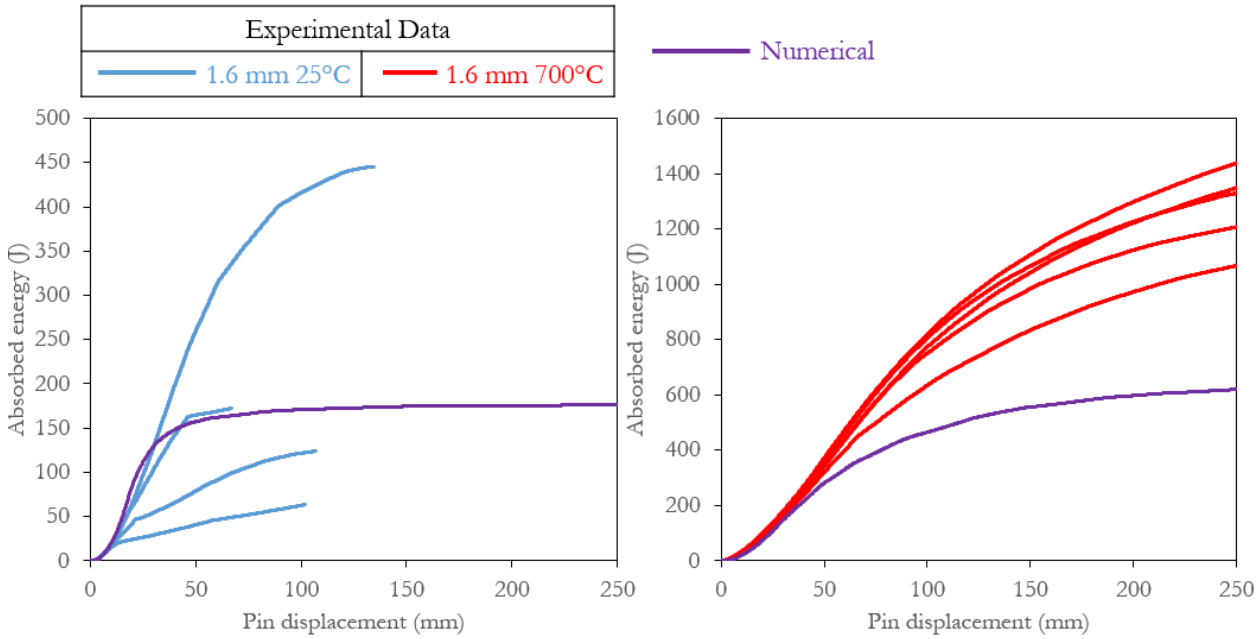

Figure 122: Comparison between simulated and experimental quasi-static caiman energy response

To further examine the differences in energy absorption, the predicted plastic strains in the flange region are plotted for a pin displacement of 37 mm in Figure 123. It can be observed that the fully martensitic specimen experiences little to no yielding in the parent metal due to the high strength of the flange relative to the weld. This suggests that much of the absorbed energy is dissipated by straining within the weld element of the fully quenched sample. In contrast, the lower strength and

higher ductility of the softer tailored flange resulted in more extensive plastic deformation and energy absorption by plastic work in the parent metal.

The predicted rate of crack extension is compared to the measured data (from the thermal measurements in Section 6.1.3 in Figure 124). For the fully quenched samples, the mechanical work was absorbed primarily in the spot weld elements, thus, once failure initiated in the first weld it propagated rapidly as demonstrated by the low pin displacement between progressive weld failures. The failure propagation was slower in the tailored flange specimen because the parent metal experienced yielding in the flange and higher energy absorption prior to each weld failure.

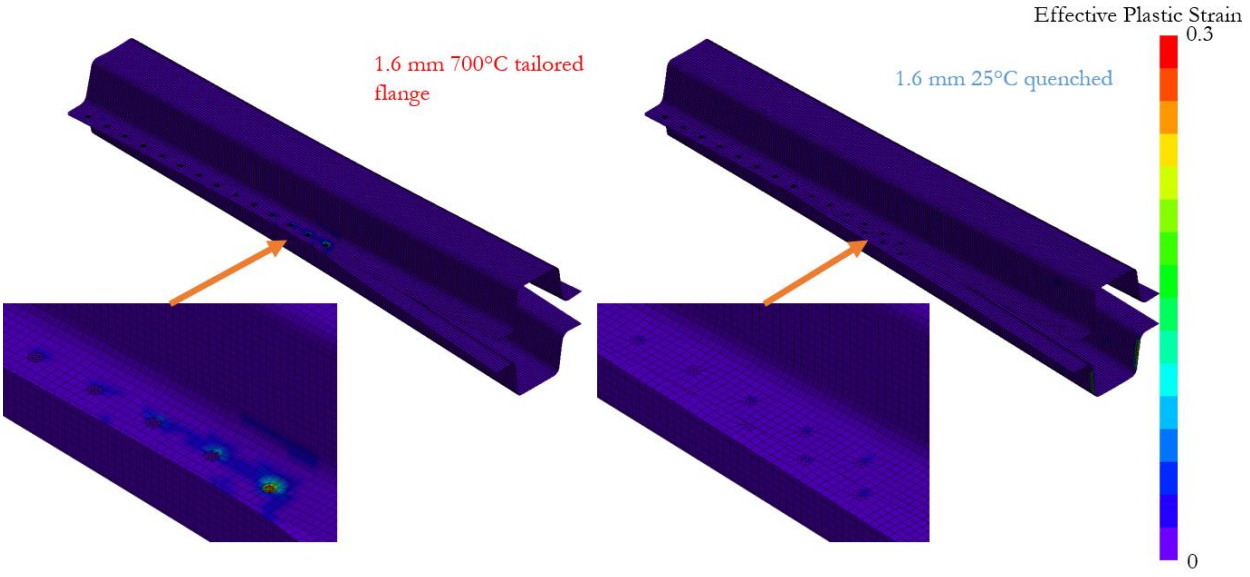

Figure 123: Plastic strain contour plots from 1.6 mm 25°C quenched (Right) and 700°C tailored flange (Left) quasi-static Caiman simulations. Pin displacement = 37 mm.

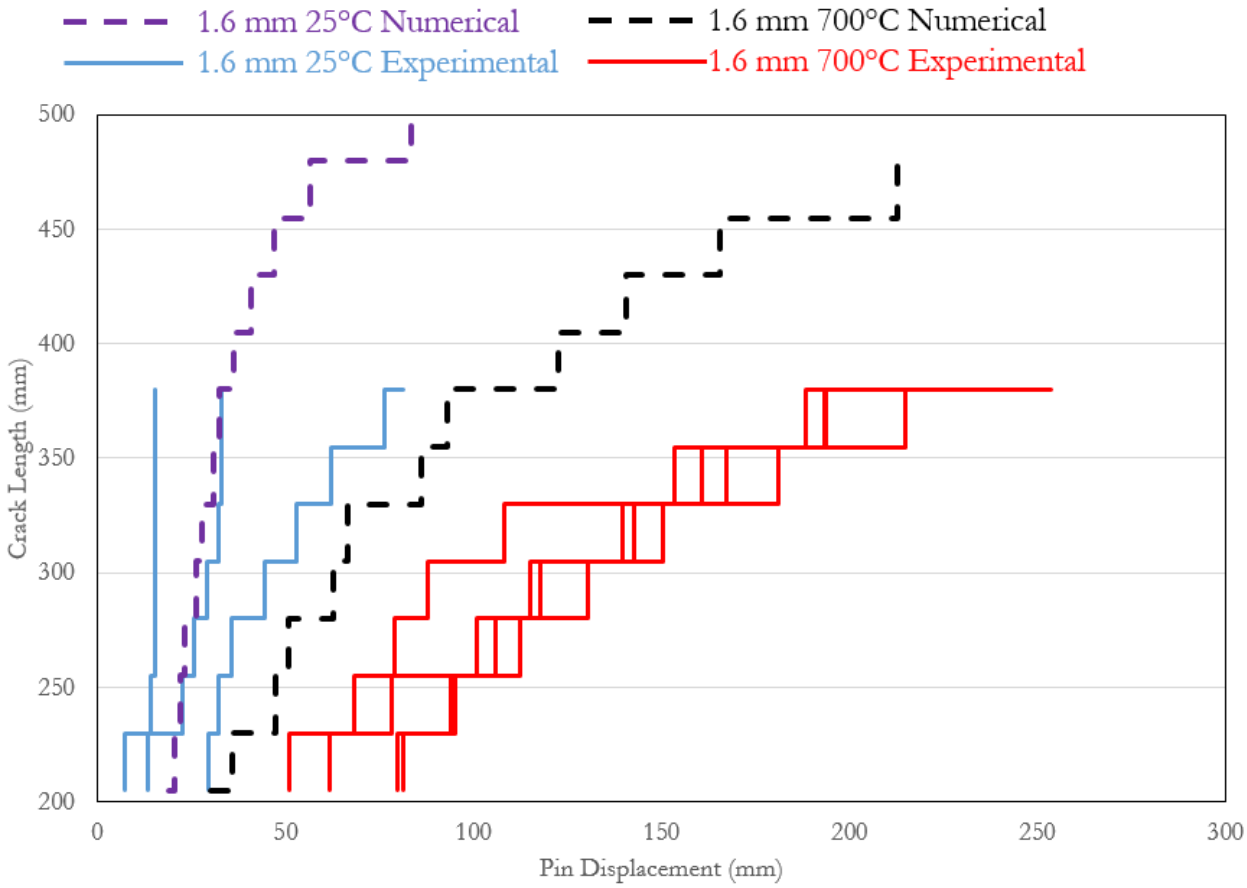

Figure 124: Crack length in numerical and experimental quasi-static Caiman specimen plotted over pin displacement for all 1.6 mm material tests

The thermal images served to indicate how mechanical work was distributed in the system. As shown in Figure 125 the plastic strain distribution in the numerical model, which shows regions of dissipation of plastic work within the flange, corresponds well with the high temperature regions in the thermal images, particularly for the tailored components. For the fully quenched specimen, the deformation was focused in the welds with little deformation in the parent metal. In the tailored flange, the higher temperature within the flange (away from the weld) is consistent with the plastic strain distribution predicted by the model.

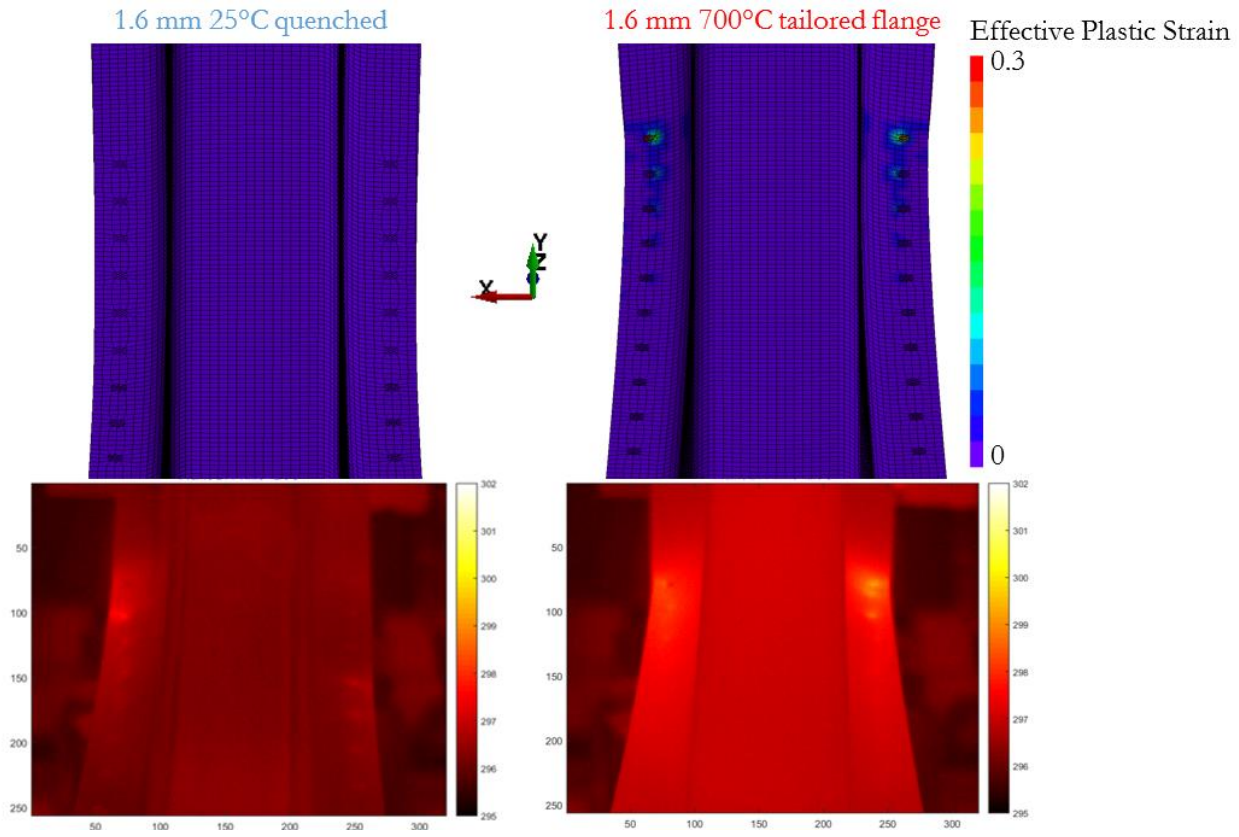

Figure 125: Predicted plastic strain distributions (top) and measured thermal images (bottom) of 1.6 mm fully quenched (left) and 700°C tailored flange (right) specimens from quasi-static caiman. Pin displacement = 37 mm.

7.3 Dynamic Mode I Caiman Simulations

The dynamic Caiman experimental data, shown in Chapter 6, allowed for investigation of the high rate behaviour of welded joints in terms of strength and toughness. In this section, the modelling technique, using the weld models developed in Chapter 5, is applied to the dynamic Caiman model and the predictions are compared to experimental data.

7.3.1 Dynamic Mode I Caiman Models

The structure used to open the jaw of the Caiman specimen was complex, as shown by Figure 68. Unlike the quasi-static experiment, the load was not measured close to the pins, therefore the entire assembly needed to be modelled so that comparison could be made between the data collected and numerical predictions. The mesh used to model the dynamic experiment is shown in Figure 126. To reduce the complexity of the simulation, the bolted connections were simplified to nodal constraints between the major components of the wall and sled structures. All of the fixture components were meshed using fully integrated solid elastic elements.

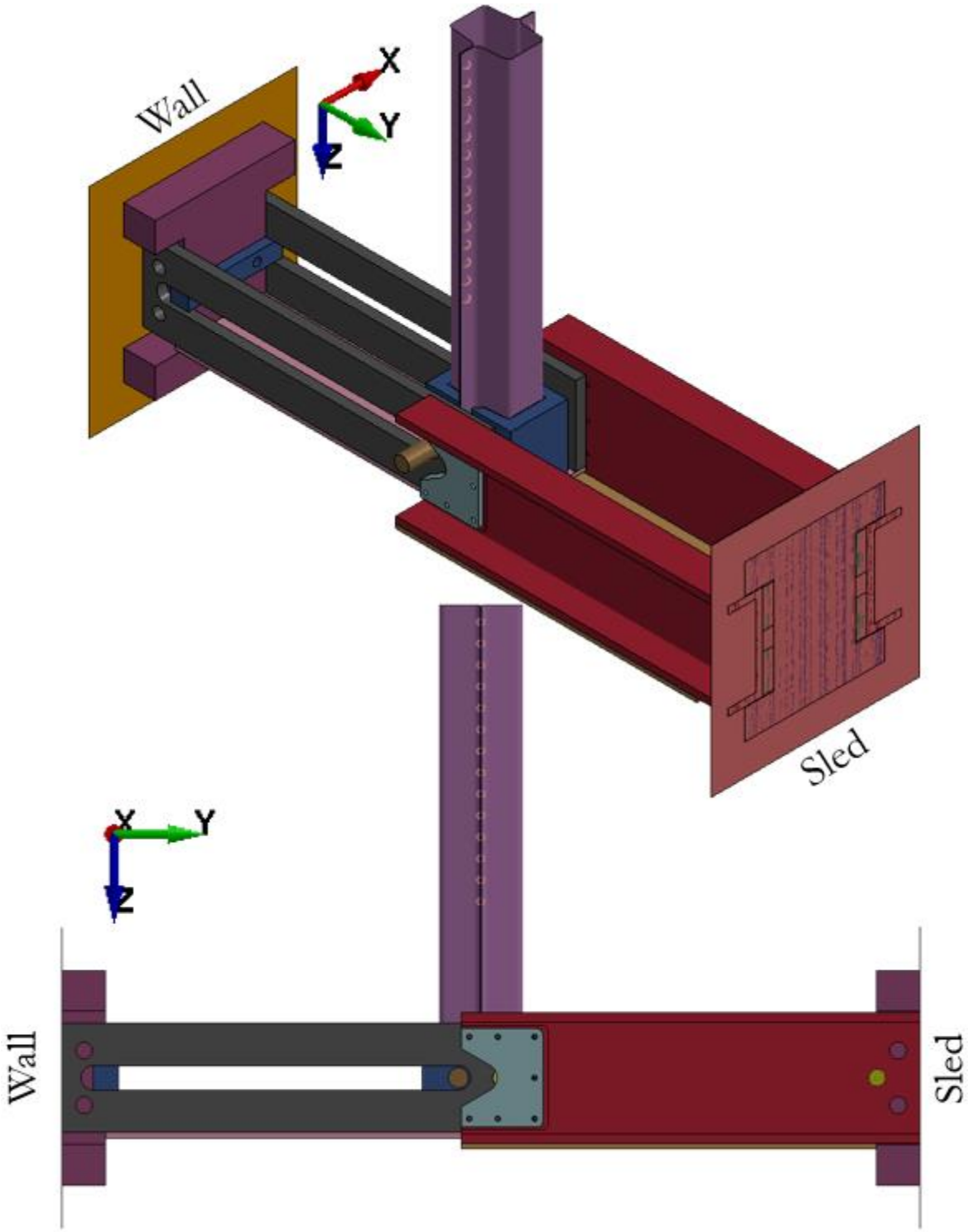

Figure 126: Dynamic caiman mesh assembly

To replicate the motion of the sled, a rigid plate was tied to the I-shaped component and assigned a mass of 1098 kg. An initial velocity of -7.5 m/s was also assigned to all the nodes within the sled assembly. On the impact barrier side of the experiment, a rigid plate was defined that was fixed in spaced and tied to the opposing I-shaped component. The simulation ran until 110 mm of displacement was reached after contact. This value was chosen because the predicted spot weld failure progress through the weld line faster than was observed in the experiments and the reaction load of the specimen had dropped off by the end of the simulated event. Contact was defined between all components using the same contact definitions as adopted in the quasi-static model. Since the time which elapsed over the experimental event was short and there where dynamic impulsive loadings as shown by Chapter 6, the simulation was ran explicitly. Also, the duration of the event was minimal so mass scaling was not applied during simulations.

7.3.2 Dynamic Mode I Caiman predictions and comparison with experiment

The predicted force-displacement response is compared to the dynamic experimental data in Figure 127. For the fully martensitic data, the initial peak is not as large as the experimental data but the numerical force response is within the corridor of the experimental data. The tailored flange specimen had an initial force response similar to that of the experimental data but experiences a second peak and a rapid drop off which the experiment didn't show. In general, the numerical results aligned relatively well with the experimental data. Since the mesh used to represent the components of the experimental fixtures were not finely meshed, contact between the various surfaces likely caused the variation after the initial deformation and the pins couldn't rotate like they could in reality because the

surface was not smooth. In addition, the measured loads are less than 3.3% of the maximum range of the load cell assemblies, hence, the potential for measurement error is high.

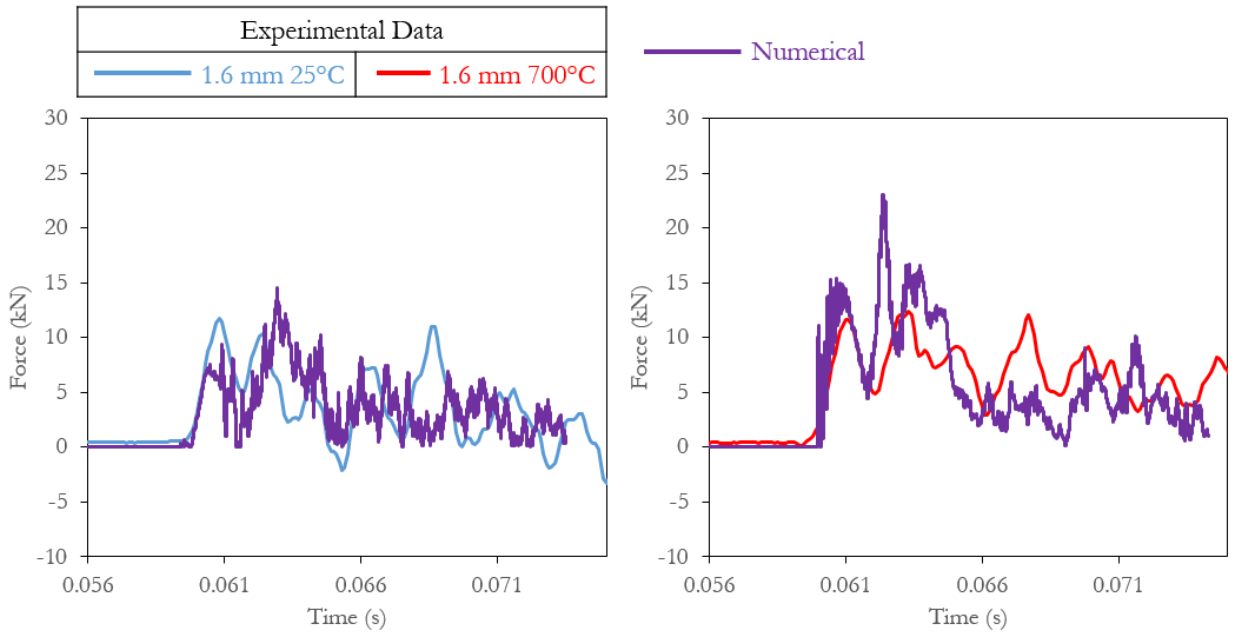

Figure 127: Comparison between predicted and measured force response in the dynamic Caiman tests

By integrating the force-displacement response, the toughness of the specimen can be quantified. A comparison between the numerical predictions and experimental data is shown in Figure 128. Although the force response of the fully hardened specimen of the simulation appeared similar to the experimental data, the energy absorption is considerably lower. Since the softened HAZ region around the welds in the fully martensitic flanges was not accounted for in the models, the mechanical work done by plastic work in the flange was not accounted for. For the tailored flange specimen, the predicted energy absorption aligned with the measured data well. Since the majority of the mechanical work was done by the base material and there was no significant HAZ softening in the 700°C tailored material (Figure 54), the model was able to capture the absorbed energy relatively well.

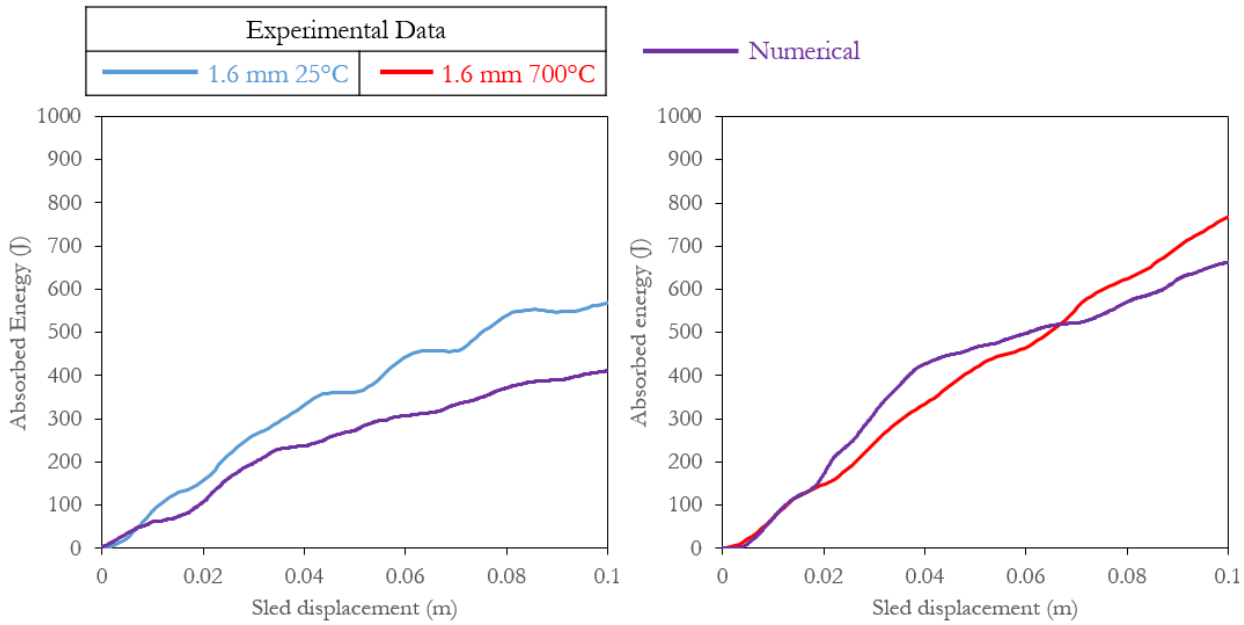

Figure 128: Comparison between predicted and measured energy absorption (toughness) for dynamic Caiman tests

The predicted plastic strain distributions within the two specimen configurations are shown in Figure 129. For the fully martensitic specimen, the plastic strain in the welded regions was approximately 10% strain, which is much higher than was predicted for the quasi-static experiment. The tailored flange specimen also experienced higher predicted plastic strain values in the flange and the deformation was not exclusively in the regions of the parent metal mesh contacting the spot welds. As shown by the plastic strain contour plots in Figure 129, the ability of the softer tailored flanges to dissipate kinetic energy improved the overall performance of the specimen.

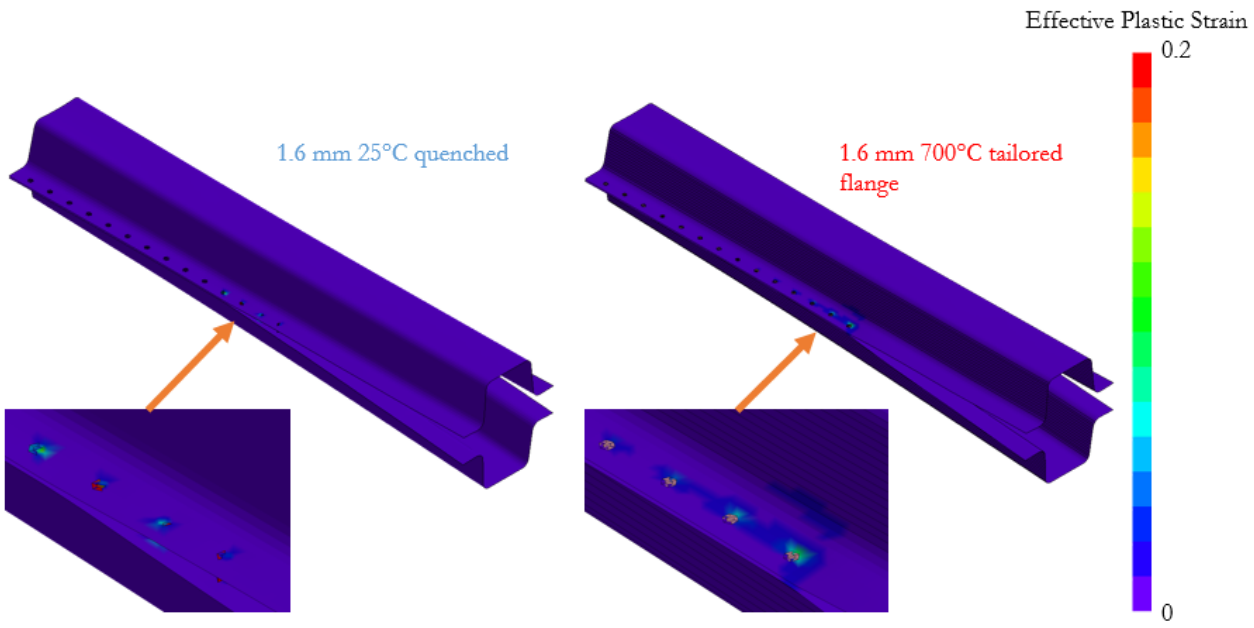

Figure 129: Plastic strain contour plots from 1.6 mm 25°C quenched (Left) and 700°C tailored flange (Right) dynamic caiman simulations. Pin displacement = 52 mm.

Even though the martensitic parent metal was stronger, the lack of deformation in the flange reduced the overall energy absorption since weld fracture initiated sooner and propagated quickly through the weld line as shown in Figure 130. When comparing the quasi-static and dynamic models both specimens exhibited a delay in the onset of the first weld failure relative to the corresponding quasi-static response. After the initiation of weld failure, the propagation was faster for both fully quenched and 700°C tailored material conditions, with the fully dynamic martensitic sample exhibiting a steep slope. Note that measurements of weld failure were not possible in the dynamic experiments since the weld failure events occurred outside of the thermal image due to the smaller image size. This issue will be corrected in future work. The effect of strain rate can also be observed by comparing Figure 123 to Figure 129 in that the quasi-static experiment experiences more plastic strain in the base metal than the dynamic version of the test.

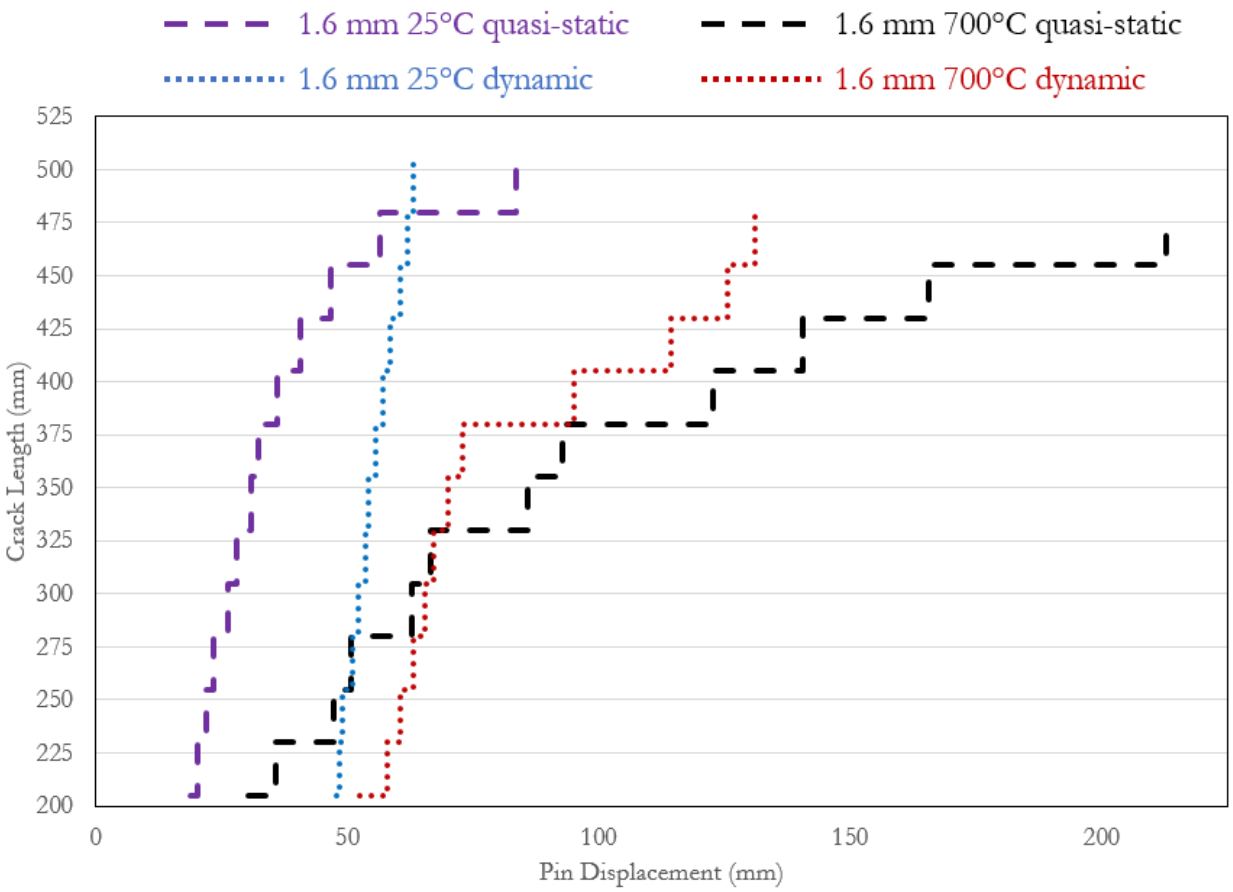

Figure 130: Comparison of crack opening between weld failures for 1.6mm fully quenched and 700°C tailored flange quasi-static and dynamic caiman simulations

For comparison purposes, the predicted plastic strain contours shown adjacent to the corresponding thermal images in Figure 131. Both the thermal images and contour plots demonstrate that deformation is confined to regions near the welds. For the 700°C tailored flange, the extent of strain within the flange is higher and deformation extends between the welds, corresponding to the temperature distribution in the thermal image.

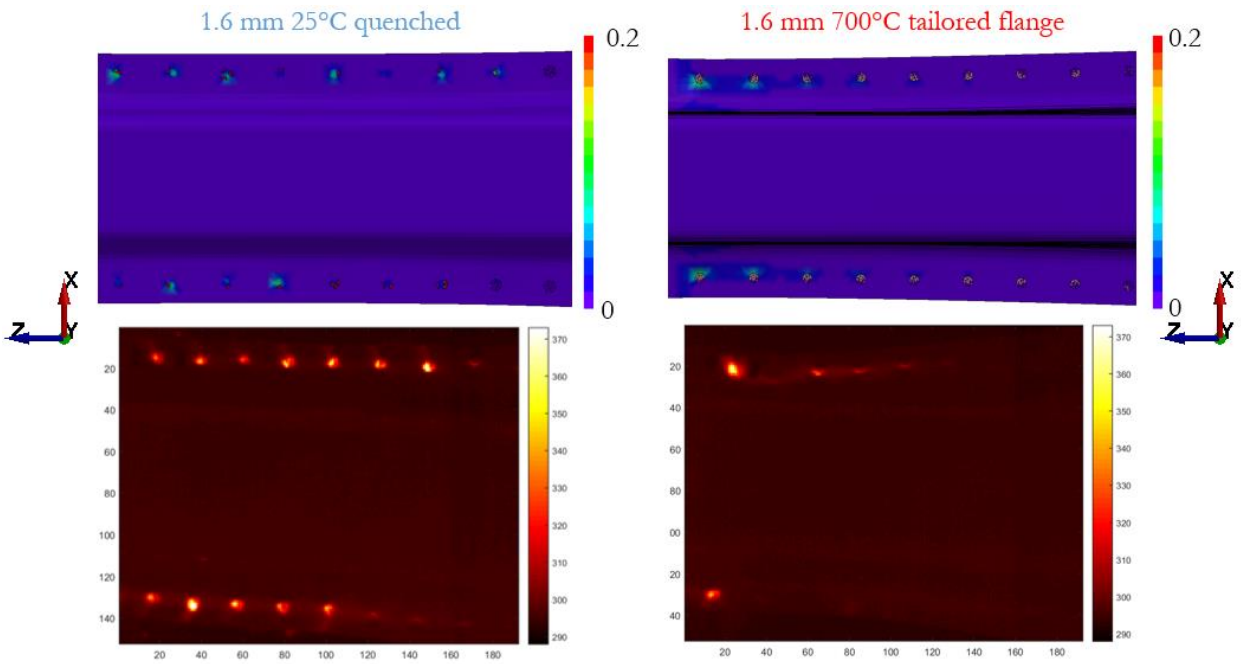

Figure 131: Numerical plastic strain (top) and experimental thermal images (bottom) of 1.6 mm fully quenched (left) and 700°C tailored flange (right) specimens from dynamic caiman testing. Pin displacement = 52 mm.

8.0 Discussion, conclusions, and Recommendations

8.1 Discussion

This thesis presents a new experiment, dubbed the "Caiman", for characterization of failure within spot weld groups under Mode I loading. In addition, the single weld cross tension and lap shear experiments, along with observations of weld microstructure and hardness distribution, served to characterize individual weld properties. Of particular interest was the manner in which tailoring of the hot stamped parent metal to achieve various strength conditions served to highlight the interaction between weld strength and parent metal/HAZ strength in controlling energy absorption.

The hardness measurements on the as-welded samples revealed a significant drop in hardness within the HAZ of welds of fully quenched martensitic parent metal. The hardness drop in the HAZ became less pronounced as the parent metal strength was reduced. The single weld testing served to demonstrate the influence of the parent metal strength in dissipation of plastic work, a key metric describing the performance of a joint. In tension loading, all welds showed similar strengths for a given thickness, with the low strength material conditions seeing somewhat higher displacement before fracture. The resulting fracture surfaces exhibited nugget pull out consistently with less displacement in the thicker grade. Under shear loading, the effect of tailoring was again evident in terms of the softer conditions experiencing more nugget rotation and the fully hardened material exhibiting a more rigid response. The fully hardened material exhibited nugget pullout with fracture contained within the welded region. For the ductile grades, nugget pull out was observed with some seeing fracture transition from the welded region to the base metal.

The V-bend experiments showcased how the distribution of strain in the joint influenced the fracture mode. For the fully hardened and 800 MPa material condition (400 °C die quench), strain

localized in the HAZ which caused rapid fracture initiation and propagation at low equivalent strains. The 600 MPa grade (700 °C die quench) displayed a more uniform strain distribution and higher strain at failure, similar to that measured in the parent metal V-bend experiments. The study of weld behaviour in each parent metal condition was concluded by the testing of spot welded uniaxial tensile samples (JIS geometries) in which strain and fracture localization occurred in the weld for the hardened material, whereas the tailored grades exhibited strain localization and fracture in the base metal.

The quasi-static Caiman experiments demonstrated that joints in which the parent metal participates in the dissipation of plastic work had superior structural performance, at least in terms of energy absorption. For the fully hardened material condition, plastic strain localized in the welded region causing either interfacial fracture or nugget pull out in the HAZ. Since a smaller amount of material was actually performing mechanical work, the load was rapidly transmitted from weld-to-weld causing rapid unzipping of the hat channels. In the tailored grades, weld failure did not propagate as quickly for a given load point displacement because the parent metal performed mechanical work prior to fracture, providing more effective energy dissipation. The dynamic Caiman experiments exhibited the same phenomena, however, the rate of weld failure propagation was accelerated, possibly due to the material constitutive strain rate sensitivity (both parent and weld metal) and the potential effect of strain rate on failure strain, which is relatively unknown. The thermography also revealed significantly higher temperature increase during weld failure in the dynamic experiments due to near adiabatic conditions at higher rates of strain. The associated thermal softening may also trigger onset of earlier failure during the dynamic experiments through adiabatic shear localization as discussed by Rahmaan *et al.* [71].

The use of digital image correlation techniques to measure strains on the surface of welded specimens proved of limited utility since the majority of the deformation leading to failure of the weld occurs within the weld nugget or HAZ as opposed to the surface. However, where digital image correlation strain measure lacks, thermography compensates. The high speed thermal imaging equipment was received towards the end of this thesis and was only used during the Caiman testing. Nonetheless, using thermography the location and time of each weld failure was visible due to a spike in temperature associated with the fracture process. For the quasi-static experiment, the temperature rise was only a few degrees since the material had time to dissipate heat as it deformed. In the dynamic tests, a significant thermal spike of 80°C was observed in the fracture region because of near-adiabatic conditions. For the softer tailored conditions, the contribution of plastic work within the parent metal away from the weld was evident in terms of the significant temperature rise away from the welds. From examination of the thermal images shown in Figure 107 and Figure 115, the fully hardened material only experienced temperature increase in the welded regions whereas the tailored flanges show an increase in the entire flange.

Comparison between the numerical models and experiments has revealed the importance of calibration of the post failure response, using the "fade energy" numerical parameter, to more closely capture the energy released during the fracture event. Of particular note, the Caiman simulations utilized the weld model parameters calibrated based upon the single weld cross tension and lap shear experiments without further adjustment or tuning of the parameters. For the quasi-static Caiman simulations, the predicted load-displacement response and failure propagation predictions were relatively accurate, with higher errors for the fully martensitic case. (It is noted that the welds in the fully martensitic samples exhibited a high degree of scatter, as seen in Figure 103) The dynamic simulations aligned relatively well with the experimental results. The plastic strain contours predicted using the numerical models help to explain why the tailored (softer) material conditions absorbed

higher levels of energy than the fully hardened specimens. Plastic strain in the fully hardened specimens was low and confined to the weld region, whereas larger strained regions were evident in the tailored flanges, promoting increased energy absorption.

The scope of work in this thesis was focused on so-called CAE approaches to weld failure prediction currently used in industrial simulation of vehicle crashworthiness. Such large simulations require efficient shell-based formulations which limit the level of detail and mesh refinement, preventing accurate simulation of the heat affected zone, for example. More detailed simulation of the weld geometry and microstructure is required, using meso-scale models for example, to accurately simulate weld failure. Such approaches are left for future work.

8.2 Conclusions

The following conclusions stem from this research:

- The toughness of the RSW joints in the current research was controlled by the relative strength of the parent metal, weld nugget and HAZ. Although the fully quenched martensitic condition offered the highest parent metal strength, when it was resistance spot welded a softened heat affected zone was produced. Since the HAZ was the weakest link in the structure, the onset of strain localization resulted in failure at relatively low displacement and correspondingly low joint toughness. In the lower strength tailored parent metal conditions, the HAZ and parent metal strengths were similar, promoting more plastic work in the parent metal prior to failure which increased the toughness of the joint.
- The degree to which the parent metal participated in dissipation of plastic work controlled the energy absorption of the RSW joints studied and the rate of propagation of weld failure

within the Caiman experiments. This behaviour is reflected in the lower toughness and high failure propagation rates in the fully martensitic joints *versus* that observed in the tailored joints.

- This work has identified a novel application of infrared thermography to identify the time and location of spot weld failure in a crash structure. While each material condition showed variations in failure mode, they all exhibited a local temperature spike during the failure process.
- The major strain components within the welded region of the Caiman samples are located either within the weld nugget (as in interfacial failure) or oriented along the sheet through-thickness direction during HAZ pullout and do not act in the in-plane direction on the sheet surface. As a result, DIC techniques were not useful in the current Caiman experiments to characterize the local strains at weld failure.
- The spot weld failure treatment in the shell-based numerical models provided reasonably accurate predictions of failure propagation, but were strongly dependent upon the "energy fade" numerical parameter.

8.3 Recommendation

To build on what is presented here, the following recommendations should be considered:

- The fully martensitic samples exhibited a high degree of scatter that may be attributed to a sub-optimal welding process, particularly for the 1.6 mm samples. The welding procedure and experiments for these samples should be revisited.
- To better understand the mechanics of weld deformation, the technique developed by Peer [72] to measure the through-thickness strain distribution should be considered to

characterize the interior strains operative in the spot welded joint. This technique utilizes DIC measurements of strain at the edge of partially-sectioned spot welds and could be extended to the Caiman experiment to further examine failure propagation and load-sharing within weld groups.

- Since martensite has been shown to be strain rate-sensitive by Bardelcik *et al.* [73], high rate testing should be conducted on resistance spot welds to investigate the rate sensitivity (constitutive and failure response) of the spot weld nugget and HAZ.
- The temperature measurements as determined by infrared thermography are largely dependent on the emissivity. To improve the accuracy of these measurements the influence of deformation and fracture on the emissivity of the current materials should be investigated.
- The Caiman test provides a means to compare different joining methods in the same loading condition. More work should be done to characterize different joining methods for comparison to the performance of resistance spot welds.
- To refine the dynamic Caiman experiment, shock absorbent materials should be used to eliminate the bounce after impact so that contact between the fork and pin can be maintained throughout the test.
- Load should be sampled close to the point of impact in the dynamic Caiman test so the force response is not attenuated by the relative large loading fixtures.
- Models should be developed that can capture the material behaviour in the HAZ so that a damage model can be implemented to more accurately predict weld failure in structural models. Such models could range from meso-scale simulations of the weld microstructure to traction-separation-type cohesive zone treatments applied to the HAZ.

- To better characterize the normal strength of RSW joints, the displacement should be measured close to the weld with an extensometer to negate the influence of fixture compliance in the force-displacement response.

9.0 Reference

[1] H. Karbasian and A. Tekkaya, "A review on hot stamping," *Journal of Materials Processing Technology,* pp. 2103-2118, 2010.

[2] H. Liu, X. Jin, H. Dong and J. Shi, "Martensitic microstructural transformations from the hot stamping, quenching and partitioning process," *Materials characterization,* vol. 62, no. 2, pp. 223-227, 2010.

[3] A. Bardelcik, C. P. Salisbury, S. Winkler, M. A. Wells and M. J. Worsiwick, "Effect of cooling rate on the high strain rate properties of boron steel," *International Journal of Impact Engineering,* vol. 37, no. 6, pp. 694-702, 2010.

[4] R. George, "Hot Forming of Boron Steels with Tailored Mechanical Properties Experiments and Numerical Simulations," Waterloo, 2011.

[5] H. Hoffmann, H. So and H. Steinbeiss, "Design of Hot Stamping Tools with Cooling System," *CIRP Annals - Manufacturing Technology,* vol. 56, no. 1, pp. 269-272, 2007.

[6] K. Mori, S. Maki and Y. Tanaka, "Warm and Hot Stamping of Ultra High Tensile Strength Steel Sheets Using Reistance Heating," *CIRP Annals - Manufacturing Technology,* vol. 54, no. 1, pp. 209-212, 2005.

[7] R. George, A. Bardelcik and M. J. Worswick, "Hot forming of boron steels using heated and cooled tooling for tailored properties," *Journal of Materials Processing Technology,* vol. 212, pp. 2386-2399, 2012.

[8] P. Akerstrom, G. Bergman and M. Oldenburg, "Numerical Implementation of a constitutive model for simulation of hot stamping," *Modelling and Simulation in Materials Science and Engineering,* vol. 15, pp. 105-119, 2007.

[9] P. Srithananan, P. Kaewtatip and V. Uthaisangsuk, "Micromechanics-based modeling of stress-strain and fracture behaviour of heat-treated boron steels for hot stamping process," *Materials Science and Engineering,* vol. 667, pp. 61-76, 2016.

[10] S. Golling, R. Östlund and M. Oldenburg, "A study on homogenization methods for steels with varying content of ferrite, bainite, and martensite," *Journal of Materials Processing Technology,* vol. 228, pp. 88-97, 2016.

[11] A. Bardelcik, M. J. Worswick, S. Winkler and M. J. Wells, "A strain rate sensititve constitutive model for quenched boron steel with tailored properties," *International Journal of Impact Engineering,* vol. 50, pp. 49-62, 2012.

[12] A. Haufe, F. Neukamm, M. Feucht, P. DuBois and T. Borvall, "A comparison of recent damage and failure models for steel materials in crashworthiness application in LS-DYNA," in *11th International LS-DYNA Users Conference*, Detroit, 2010.

[13] L. ten Kortenaar, "Failure Characterization of Hot Formed Boron Steels with Tailored Mechanical Properties," Waterloo, 2016.

[14] K. Omer, L. ten Kortenaar, C. Butcher, M. J. Worswick, S. Malcolm and D. Detwiler, "Testing of Hot Stamped Axial Crush Member with Tailored Properties - Experiments and Models," *International Journal of Impact Engineering,* vol. 103, pp. 12-28, 2017.

[15] T. Eller, L. Greve, M. Andres, M. Medricky, A. Hatscher, V. Meinders and A. v. d. Boogaard, "Plasticity and fracture modeling of quench-hardenable boron steel with tailored properties," *Journal of Materials Processing Technology,* vol. 214, pp. 1211-1227, 2014.

[16] Y. Prajogo, "Hot Stamping of a Boron Steel Side Impact Beam with Tailored Flange Properties," Waterloo, 2015.

[17] K. Omer, "Development and Testing of a Hot Stamped Axial Crush Member with Tailored Properties," Waterloo, 2014.

[18] S. Hamidinejad, F. Kolahan and A. Kokabi, "The modeling and process analysis of resistance spot welding on galvanized steel sheets used in car body manufacturing," *Materials and Design,* vol. 34, pp. 759-767, 2012.

[19] Y.-S. Jong, Y.-K. Lee, D.-C. Kin, M.-J. Kang, I.-S. Hwang and W.-B. Lee, "Microstructural Evolution and Mechanical Properties of Resistance Spot Welded Ultra High Strength Steel Containing Boron," *Materials Transactions,* vol. 52, no. 6, pp. 1330-1333, 2011.

[20] M. T. Horst Lanzerath, "Lightweight Potential of Ultra High Strength Steel Tubular Body Structures," *SAE International Journal of Materials and Manufacturing,* vol. 8, no. 3, pp. 813-822, 2015.

[21] P. Kumar, "Lectures 11 & 12," NPTEL, 31 December 2009. [Online]. Available: http://nptel.ac.in/courses/112107144/35. [Accessed 02 09 2016].

[22] Shinkokiki Co., "Basis and Point of Resistance Welding," Shinkokiki Co., 2014. [Online]. Available: http://www.shinkokiki.co.jp/en/knowledge/miracle. [Accessed 02 09 2016].

[23] ISO, "ISO 10447:2015(en), Resistance welding - Testing of welds - Peel and chisel testing of resistance spot and projection welds," 2015. [Online]. Available: https://www.iso.org/obp/ui/#iso:std:iso:10447:ed-3:v1:en. [Accessed 15 09 2016].

[24] American Welding Society, *AWS D8.9M:2012, Test Methods for Evaluating the Resistance Spot Welding Behaviour of Automotive Sheet Steel Materials,* American Welding Society, 2012.

[25] S. Donders, M. Brughmans and L. Hermans, "The Effect of Spot Weld Failure on Dynamic Vehicle Performance," in *the 23rd International Modal Analysis Conference*, Orlando, FL, 2005.

[26] E. E. Medeiros, A. M. d. S. Dias and A. L. Christoforo, "Numerical Simulation of Mechanical Fracture Testings," *International Journal of Materials Engineering,* vol. 2, no. 5, pp. 61-66, 2012.

[27] D. W. Dickinson, Welding in the Automotive Industry: State of the Art: a report, Republic Steel Research Center, 1981.

[28] M. Pouranvari, H. Asgari, S. Mosavizadch and M. G. P.H. Marshi, "Effect of weld nugget size on overload failure mode of resistance spot welds," *Science and Technology of Welding and Joining,* vol. 12, no. 3, pp. 217-225, 2007.

[29] D. W. Dickinson, "Welcome to WE602," Ohio State University, 31 03 2003. [Online]. Available: http://www.gatewaycoalition.org/files/Instructional_Technology/weld602/files/2a4%20Spot%20Weld%20Mech%20Prop.ppt. [Accessed 06 09 2016].

[30] P. Wung, "A force-based failure criterion for spot weld design," *Experimental Mechanics,* vol. 41, no. 1, pp. 107-113, 2001.

[31] S. Malcolm and E. Nutwell, "Spotweld Failure Prediction using Solid Element Assemblies," in *6th European LS-DYNA Users Conference*, 2007.

[32] J. Wang, Y. Xia, Q. Zhou and J. Zhang, "Simulation of Spot Weld Pullout By Modeling Failure Around Nugget," in *SAE 2006 World Congress & Exhibition*, 2006.

[33] K. L. Nielsen and V. Tvergaard, "Ductile shear failure or plug failure of spot welds modelled by modified Gurson model," *Engineering Fracture Mechanics,* vol. 77, pp. 1031-1047, 2010.

[34] A. Gurson, "Continuum theory of ductile rupture by void nucleation and growth: Part I--Yield criteria and flow rules of porous ductile media," *Journal of engineering materials and technology,* vol. 99, no. 1, pp. 2-15, 1977.

[35] L. Zeng, Y. Xia, H. Zhao and Q. Zhou, "On utilization of material failure criterion in modeling pull-out failure of spot-welded joints," in *ASME 2013 International Mechanical Engineering Congress and Exposition*, San Diego, 2013.

[36] N. Nguyen, D. Kim, J. Song, K. Kim, I. Lee and H. Kim, "Numerical prediction of various failure modes in spotwelded metals," *International Journal of Automotive Technology,* vol. 13, no. 3, pp. 459-467, 2012.

[37] A. Kamoulakos, "The ESI-Wilkins-Kamoulakos (EWK) rupture model," in *Continuum Scale Simulation of Engineering Materials*, Verlag, Berlin, GmbH, 2004.

[38] M. Pouranvari and S. Marashi, "Critical review of automotive steels spot welding: process, structure and properties," *Science and Technology of Welding and Joining,* vol. 18, no. 5, pp. 361-403, 2013.

[39] V. B. Hernandez, S. Nayak and Y. Zhou, "Tempering of Martensite in Dual-Phase Steels and Its Effects on Softening Behaviour," *Metallurgical and Materials Transactions A,* vol. 42, no. 3115, 2011.

[40] V. B. Hernandez, S. Panda, M. Kuntz and Y. Zhou, "Nanoindentation and microstructure analysis of resistance spot welded dual phase steel," *Materials Letters,* vol. 64, pp. 207-210, 2010.

[41] M. Pouranvari, S. Marashi and D. Safanama, "Failure mode transition in AHSS resistance spot welds. Part II: Experimental investigation and model validation," *Materials Science and Engineering A,* vol. 528, pp. 8344-8352, 2011.

[42] S. Nayak, V. B. Hernandez and Y. Zhou, "Effect of Chemistry on Nonisothermal Tempering and Softening of Dual-Phase Steels," *Metallurgical Materials and TransactionsA,* vol. 42, no. 3242, 2011.

[43] S. Dancette, V. Massardier-Jourdan, D. Fabregue, J. Merlin, T. Dupuy and M. Bouzekri, "HAZ Microstructures and Local Mechanical Properties of High Strength Steels Resistance Spot Welds," *ISIJ International,* vol. 51, pp. 99-107, 2011.

[44] T. Eller, L. Greve, M. Andres, M. Medricky, H. Geijselaers, V. Meinders and A. v. d. Boogard, "Plasticity and fracture modeling of the heat-affected zone in resistance spot welded tailor hardened boron steel," *Journal of Materials Processing Technology,* vol. 234, pp. 309-322, 2016.

[45] T. K. Eller, "Modeling of tailor hardened boron steel for crash simulation," Twente, 2016.

[46] S. Burget and S. Sommer, "Characterization and modeling of fracture behaviour of spot welded joints in hot-stamped ultra-high strength steels," in *LS-DYNA Forum*, Ulm, 2012.

[47] M. Marya, K. Wang, J. Louis G. Hector and X. Gayden, "Tensile-Shear Forces and Fracture Modes in Single and Multiple Weld Specimens in Dual-Phase Steels," *Journal of Manufacturing Science and Engineering,* vol. 128, pp. 287-298, 2006.

[48] F. Schneider and N. Jones, "Influence of spot-weld failure on crushing of thin-walled structural sections," *International Journal of Mechanical Sciences,* vol. 45, pp. 2061-2081, 2003.

[49] Y. P. Yang, J. Gould, W. Peterson, F. Orth, P. Zelenak and W. Al-Fakir, "Development of spot weld failure parameters for full vehicle crash modelling," *Science and Technology of Welding and Joining,* vol. 18, no. 3, pp. 222-231, 2013.

[50] L. Wittevrongel, P. Lava and D. Debruyne, "A Self Adaptive Global Digital Image Correlation Algorithm," *Experimental Mechanics,* vol. 55, pp. 361-378, 2015.

[51] P. Lava, "Practical considerations in DIC measurements," in *10th International conference on Advances in Experimental Mecahanics*, Edinburgh, 2015.

[52] National Instruments, "Calculating Camera Sensor Resolution and Lens Focal Length," National Instruments, 2014. [Online]. Available: http://digital.ni.com/public.nsf/allkb/1BD65CB07933DE0186258087006FEBEA. [Accessed 23 11 2017].

[53] T. L. Bergman, A. S. Lavine, F. P. Incropera and D. P. Dewitt, Fundamentals of Heat and Mass Transfer, John Wiley & Sons, Inc., 2011.

[54] Telops, "Fast-IR 2K Camera," 2016. [Online]. Available: http://telops.com/18-cameras-infrarouges/40-fast-ir-2k-rapid-ir-camera. [Accessed 26 11 2017].

[55] Telops, *Training Meeting,* Waterloo: Telops, 2017.

[56] ArcelorMittal, "Automotive Product Catalogue," ArcelorMittal, [Online]. Available: http://automotive.arcelormittal.com/saturnus/sheets/ArcelorMittal%20Automotive%20product%20offer%20EN.pdf. [Accessed 08 09 2016].

[57] Japanese Industrial Standards, *JIS Z 2241:2011 Metallic materials - Tensile testing - Method of test at room temperature,* Japanese Industrial Standards, 2011.

[58] Correlated Solutions, "The VIC-3D System," Correlated Solutions, 2017. [Online]. Available: http://correlatedsolutions.com/vic-3d/. [Accessed 11 4 2017].

[59] K. Cheong, K. Omer, C. Butcher, R. George and J. Dykeman, "Evaluation of the VDA 238-100 Tight Radius Bending Test using Digital Image Correlation Strain Measurement," in *36th IDDRG Conference - Materials Modelling and Testing for Sheet Metal Forming*, Munich, 2017.

[60] M. R. Tharrett and T. B. Stoughton, "Stretch-Bend Forming Limits of 1008 AK Steel," in *SAE World Congress*, Detroit, 2003.

[61] VDA, *VDA 238-100, Plate bending test for metallic materials,* 2010.

[62] ZRCI Refactory Composites, "REFRACTORY BOARD TYPES ZIRCAL-18, ZIRCAL-45 AND ZIRCAL-95," July 2015. [Online]. Available: http://www.zrci.com/zrci301.pdf. [Accessed 26 October 2016].

[63] T. Iuchi, T. Furukawa and S. Wada, "Emissivity modeling of metals during the growth of oxide film and comparison of the model with experimental results," *Applied Optics,* vol. 42, no. 13, pp. 2317-2326, 2003.

[64] J. Dykeman, Interviewee, *Personal Communication.* [Interview]. 2017.

[65] H. Ghassemi-Armaki, E. Biro and S. Sadagopan, "Transformations in the HAZ of Martensitic AHSS - Part 2: Advanced Characterization of HAZ Softening of AHSS for Crash Modeling," in *Sheet Metal Welding Conference*, Livonia, 2014.

[66] Plascore, "Plascore CrushLite," 2012. [Online]. Available: http://www.plascore.com/pdf/Plascore_CrushLite.pdf. [Accessed 13 04 2017].

[67] F. Seeger, M. Feucht, G. Dumitru and T. Graf, "Enhancement of Spot Weld Modeling using MAT_100_DAI," in *LS-DYNA Anwenderforum*, Bamberg, 2008.

[68] GmbH; LSTC Inc and DYNAmore, "Download LS-DYNA for UNIX/Linux/Solaris | Livermore Software Technology Corp.," 2011. [Online]. Available: http://www.lstc.com/download/ls-dyna#mpp70. [Accessed 26 11 2017].

[69] F. Neukamm, M. Feucht and A. Haufe, "Considering damage history in crashworthiness simulations," in *7th European LS-DYNA Conference*, Stuttgart, 2009.

[70] M. Jou, "Real time monitoring weld quality of resistance spot welding for the fabrication of sheet metal assemblies," *Materials Processing Technology,* vol. 132, pp. 102-113, 2003.

[71] A. A. C. B. N. P. M. J. W. Taamjeed Rahmaan, "Investigation into the shear stress, localization and fracture behaviour of DP600 and AA5182-O sheet metal alloys under elevated strain rates," *International Journal of Impact Engineering,* vol. 108, pp. 303-321, 2017.

[72] A. J. Peer, *Performance Testing and Modeling of Ultra-High Strength Steel and Complex Stack-Up Resistance Spot Welds,* Columbus: Ohio State University, 2017.

[73] M. J. W. S. W. M. J. W. A. Bardelcik, "A strain rate sensititve constitutive model for quenched boron steel with tailored properties," *International Journal of Impact Engineering,* vol. 50, pp. 49-62, 2012.

[74] W. Tong, H. Tao, X. Jiang, N. Zhang, M. P. Marya, J. Louis G. Hector and X. Q. Gayden, "Deformation and Fracture of Miniature Tensile Bars with Resistance-Spot-Weld Microstructures," *Metallurgical and Materials Transactions A,* vol. 36, no. 10, pp. 2651-2669, 2005.

[75] T. Rahmaan, A. Abedini, C. Butcher, N. Pathak and M. J. Worswick, "Investigation into the shear stress, localization and fracture behaviour of DP600 and AA5182-O sheet metal alloys under elevated strain rates," *International Journal of Impact Engineering,* vol. 108, pp. 303-321, 2017.

[76] M. I. Khan, M. L. Kuntz, E. Biro and Y. Zhou, "Microstructure and Mechanical Properties of Resistance Spot Welded Advanced High Strength Steels," *Materials Transactions,* vol. 49, no. 7, pp. 1629-1637, 2008.